THE DYNAMICS OF FISSURE-FED ERUPTIONS

Insights from the Svartsengi Volcanic System, Iceland

Rebekah Rhodes

University of Oxford

St Anne's College

Cover image: Screenshot from the Langihryggur camera at the start of the February 2024 eruption

Recent eruptions of the Svartsengi Volcanic System have repeatedly impacted infrastructure on the Reykjanes Peninsula, including damaging homes, affecting hot water supply, and displacing the entire town of Grindavík. As eruptions on the Reykjanes Peninsula are expected to continue for centuries, understanding their dynamics is crucial. This study analyses webcam footage from the first six eruptions of the Svartsengi Volcanic System to map fissure propagation and measure fire fountain heights over time. Later eruptions have been excluded due to the discontinuation of the webcam network. Results show that pulses of accelerated fissure propagation are driven by magma pressurisation, while variations in propagation speed along individual segments are influenced by crustal heterogeneities. Fissure locations are heavily affected by topography, including features formed during previous eruptions. Fire fountain heights are primarily influenced by fissure segment length and conduit erosion, with larger conduits increasing mass eruption rates and fountain heights. Predictive models successfully estimated fissure length and total erupted volume for the seventh eruption of the Svartsengi volcanic system based on pre-eruptive inflation duration, demonstrating the potential for forecasting eruption characteristics. Understanding the key controls on fissure propagation improves the ability to predict future fissure locations. Reinstating the disbanded webcam network is crucial for improving forecast accuracy, enabling further refinement of predictive models.

Word count: 7962

Contents

1 Introduction

1.1 Tectonic and Volcanic Setting of the Reykjanes Peninsula (RP)

Fissure eruptions on the Reykjanes Peninsula (fig.1.1) are driven by tectonic rifting due to Iceland's position on a divergent plate boundary. Active rifting has occurred on the RP for the last 6 – 7 Ma (Pałgan et al., 2017, Jóhannesson, 1980). Additional magmatism from Iceland's mantle plume has led to the development of a widened plate boundary through Iceland that is separated into several volcanic and tectonic zones (Einarsson, 2008). Through the RP, the plate boundary is highly oblique (DeMets et al., 1994) to the direction of plate motion (Sæmundsson et al., 2020) meaning tectonic motion must be accommodated through a combination of strike slip and normal faulting (Einarsson, 1991) within a 5 – 10km volcanic and seismic zone (Sigmundsson et al., 2022). Within the six volcanic systems on the RP, extension occurs through normal faults and fissures (Ducrocq et al., 2024).

Volcanic events on the Reykjanes Peninsula occur roughly every 800 – 1000 years. During previous volcanic events, activity has been concentrated in a single volcanic system at a time, jumping between systems from east to west every 100 – 200 years (Sæmundsson et al., 2020). Volcanism on the RP is typically marked by linear fissures that form crater rows, with the last volcanic event occurring between 800 – 1200 AD (Caracciolo et al., 2023). In March 2021, volcanism on the Reykjanes Peninsula reactivated with eruptions at Fagradalsfjall and after three years activity jumped to the Svartsengi Volcanic System in December 2023.

For clarity throughout, a volcanic event refers to the reactivation of the whole of the Reykjanes Peninsula, and a volcanic eruption refers to a single fissure eruption from one volcanic system. Maps shown have been generated on QGIS.

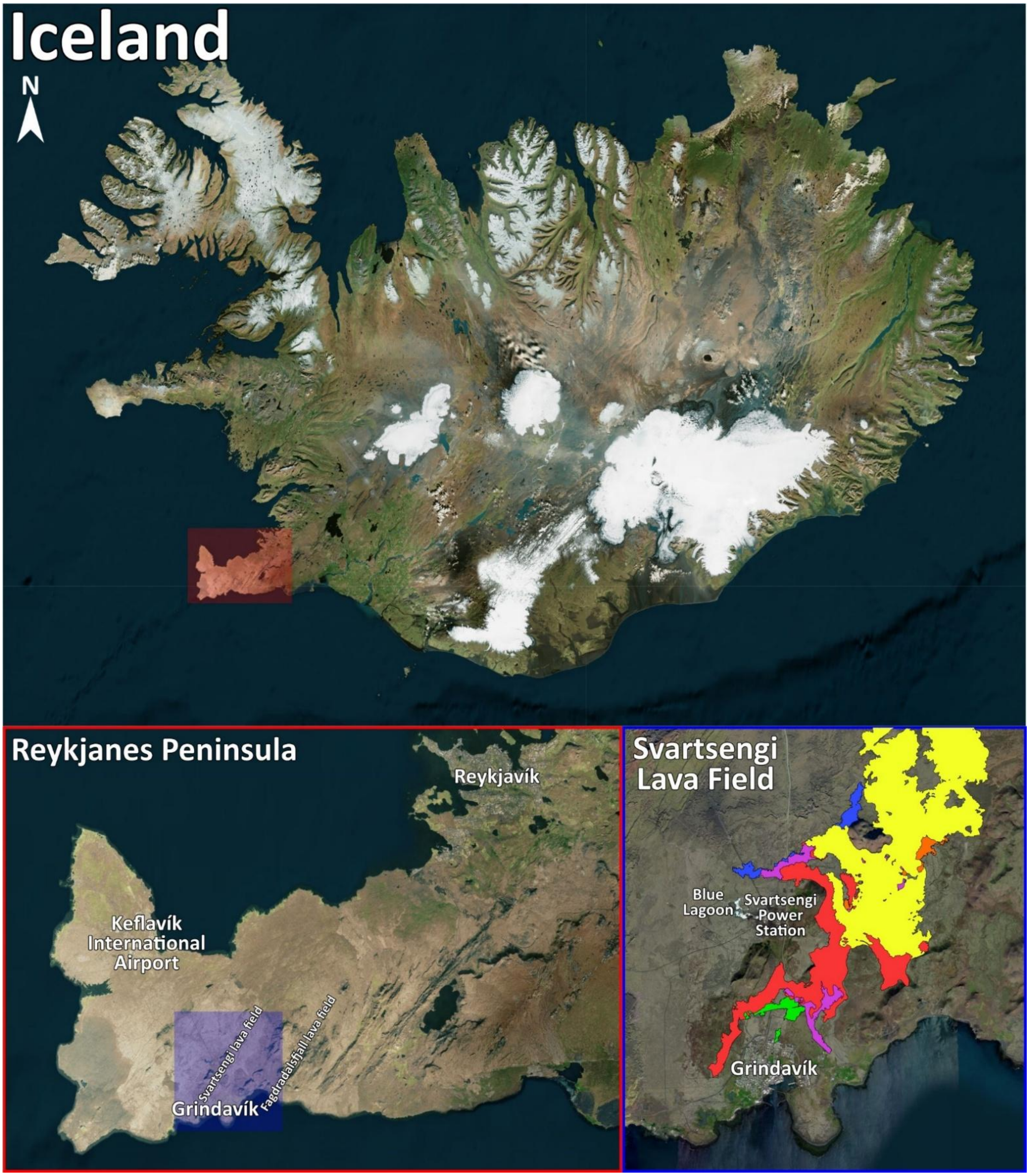

Fig.1.1: *Geographical context to the study area, showing the location of the Reykjanes Peninsula and the Svartsengi Lava Field, along with other key locations. Base maps from: Bing, 2025*

1.2 The Svartsengi Fires

The last eruption of the Sundhnúkur crater row, where the current eruptions are taking place, occurred 2350 years ago (Jónsson, 1983). Before continuous inflation of the Svartsengi magma reservoir began on 25th October 2023 (Sigmundsson et al., 2024), there were four inflation events of the Svartsengi magma reservoir in the three years prior (Giersson et al., 2021; Cubuk-Sabuncu et al., 2021; Flóvenz et al., 2022; Parks et al., 2023; Sigmundsson et al., 2024). This ultimately resulted in a dike intrusion on 10th November 2023, followed by the first eruption of the Svartsengi Volcanic System (SVS) on 18th December 2023. This marked the start of the Svartsengi fires, which has now included seven[a] subsequent eruptions (fig.1.2, fig.1.3).

[a] Eruptions after and including the seventh eruption (November 2024) have not been analysed in this project due to a lack of footage due to the discontinuation of webcams around the RP.

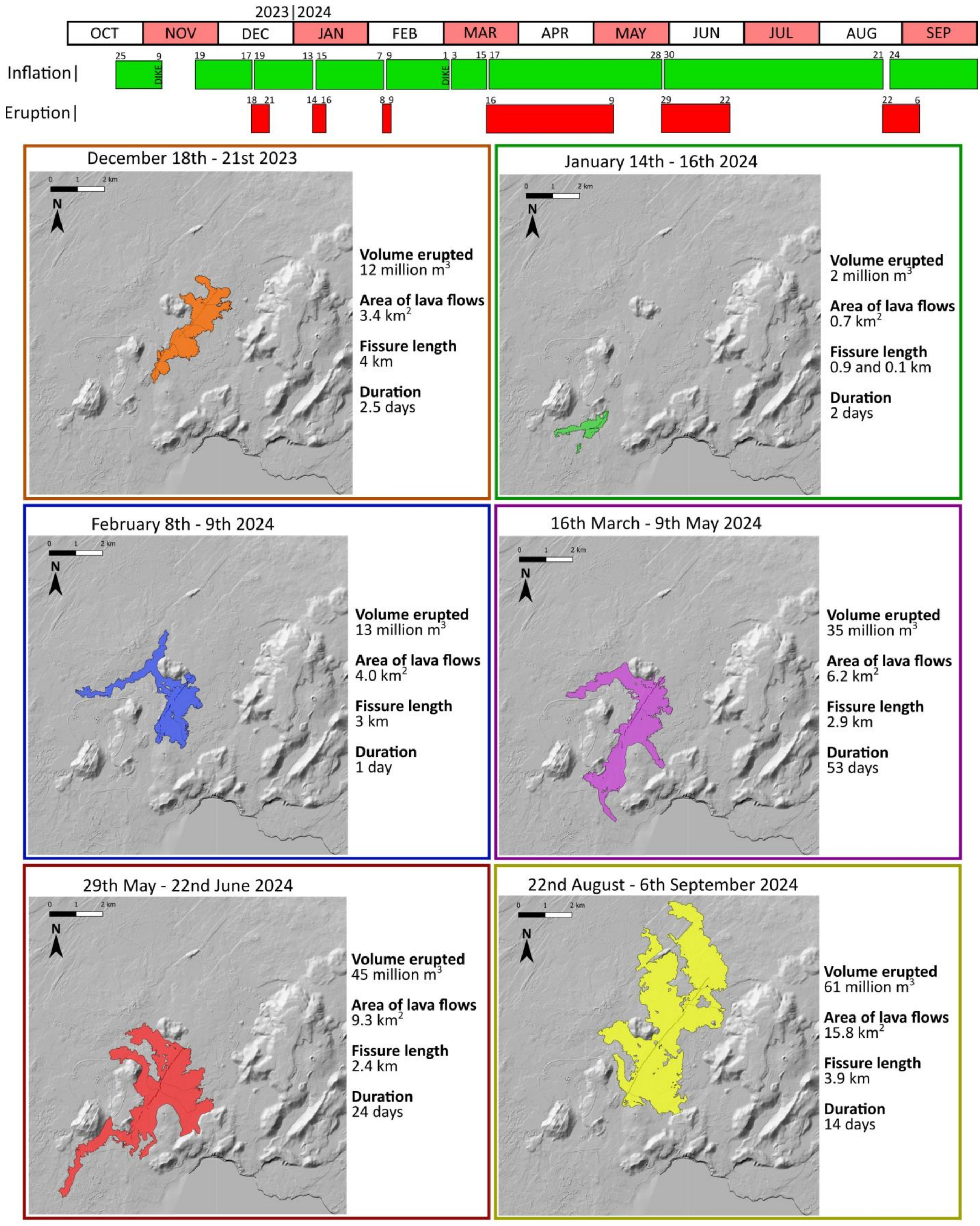

Fig.1.2: *Timeline of inflation, dike injection and eruptions along with the outlines of lava flows from each eruption and their associated fissures on the same scale maps for size comparison. Base map DEMs from: ÍslandsDEM, 2025*

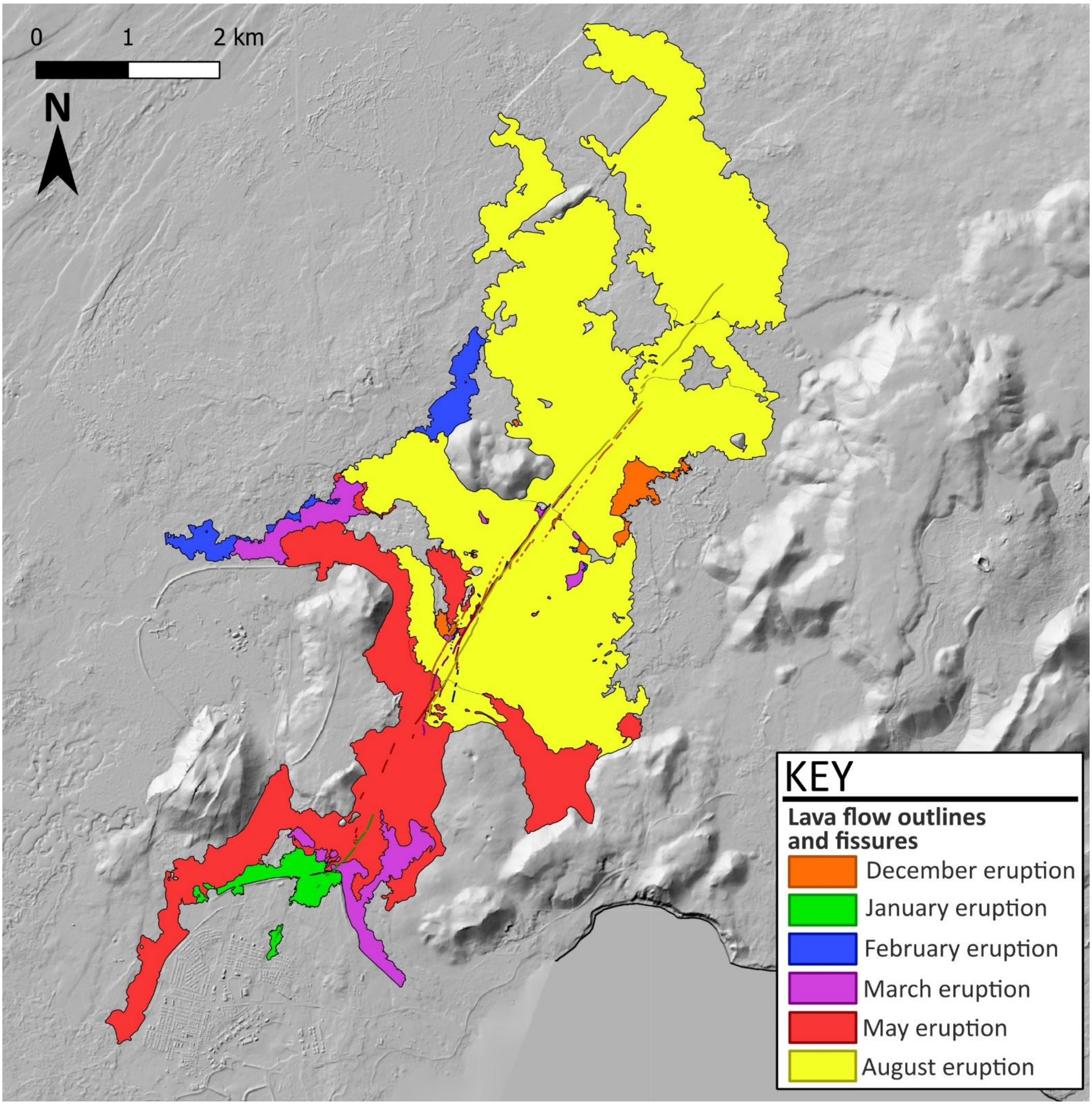

Fig.1.3: *All of the lava flows superimposed on one another to show which lava flows are outcropping at the surface. All of the fissures are also shown to compare their locations between events. Base map DEM from: ÍslandsDEM, 2025*

1.3 Motivations and Importance

The study of fissure fed eruptions is important because their often extended duration can lead to significant impacts on local communities and ecosystems. The Laki Fires in Iceland involved 10 eruptions between 1783 – 1784 with an estimated maximum extrusion rate of 8.5×10^3 and 8.7×10^3 m^3/s from fissures totalling 2.2 and 2.8 km in length respectively. Fire fountains were estimated to reach 800 – 1450 m, based on magma volatile contents and mass eruption rate (Thordarson and Self, 1993).

The environmental impacts of the eruptions were significant, leading to famine, disease, harsh winters, and ultimately death of 22% of Iceland's population (Óskarsson et al. 1984; Finnsson, 1796; Thorarinsson, 1979; Hálfdánarsson, 1984). The Laki Fires gives an indication of the potential impacts of the SVS eruptions if they increased in magnitude. Acknowledgement of these impacts allows for the development of mitigation measures, such as ensuring there is food security if growing or transport is disrupted.

Understanding these eruptions is important given that the RP is home to 70% of Iceland's population (Bideman et al., 2022) and critical infrastructure. Furthermore, there is evidence that historic lava flows reached areas that are currently inhabited and that eruptions are likely to persist for the next few centuries (Caracciolo et al., 2023; Sæmundsson et al., 2020).

The eruptions of the SVS have produced a uniquely valuable dataset, enabling the study of repeated fissure-fed eruptions from the same volcanic system. Continuous webcam footage throughout each eruption allows for direct observations and quantification of the factors controlling eruption features as the system evolves over time. Few long-duration videos of fissure eruptions exist, with most consisting of handheld footage (Spampinato et al., 2008: 2002–3 Mt. Etna eruption), or brief clips lasting only minutes (Witt & Walter, 2017: March 2011 Pu'u 'ō'ō eruption, Kilauea Volcano). This research, therefore, significantly expands upon previous fissure eruption studies using video analysis (e.g. Witt et al., 2018; Scott et al., 2023).

Witt et al., (2018) analysed fire fountains at Holurhaun (2014) after fissures had concentrated into cones, using software to continually measure the pulsating fountains. Similarly, Scott et al., (2023) examined fire fountain pulsations at Fagradalsfjall. In contrast, this study focuses on fire fountains before cone concentration, disregarding pulsations to examine the overall decay behaviour. To date, no other study has used full-duration eruption recordings to produce high-resolution maps of fissure propagation and measure early fire fountain decay before cone concentration, let alone across six[b] separate eruptions.

1.4 Research Questions and Hypotheses

This project investigates fissure propagation and fire fountaining dynamics during the first six eruptions of the Svartsengi Volcanic System (SVS) from December 2023 to September 2024. Eruptions from November 2024 onwards were excluded due to the discontinuation of the webcam network. The research addresses the following key questions:

- Does fissure propagation follow a consistent pattern across eruptions?
- Does fissure opening align with known faults and previous fissures?
- Can these insights improve prediction of fissure-prone locations?
- What is the rate of fissure propagation?
- Do fire fountain heights follow a uniform decay pattern?
- What are the primary controls on fire fountain heights?
- Can correlations between measured parameters be integrated into predictive models?
- What eruption characteristics can be predicted for future eruptions?

[b] Six eruptions have had fissure propagation analysed, four eruptions have had fire fountain measurements

2 Methodology

2.1 Data: Webcam Footage

Continuous webcam video footage (table.2.1) has been provided by the Icelandic Met Office (IMO) for the first six eruptions of the SVS, named throughout as such: December (18/12/23 – 21/12/23), January (14/01/24 – 16/01/24), February (08/02/24 – 08/02/24), March (16/03/24 – 09/05/24), May (29/05/24 – 22/06/24), and August (22/08/24 – 06/09/24). Multiple webcams capture different viewpoints during each eruption, allowing topographic obstructions to be avoided. Cameras often zoom and pan around eruptions which can make maintaining consistent observations challenging. The most useful cameras during each eruption have been selected and their locations recorded. The footage was reviewed in two stages: first to map the fissure propagation, and second to measure the fire fountain heights. This ensured that the fire fountains measured could be correlated to the correct fissures.

Eruption	Webcam	Start date	Start time	End date	End time	Used?
December *18/12/23 – 21/12/23*	LFI langihryggur	18/12/2023	23:00	21/12/2023	00:00	**Yes**
	MBL webcam 1	18/12/2023	22:00	21/12/2023	00:00	**Yes**
	MBL webcam2x	18/12/2023	22:00	21/12/2023	00:00	Not as good as others
January *14/01/24 – 16/01/24*	LFI reyjanes2	14/01/2024	10:00	16/01/2024	06:00	**Yes**
	LFI visir 2	14/01/2024	08:00	16/01/2024	01:00	Poor quality
	MBL webcam1	14/01/2024	07:00	16/01/2024	11:00	**Yes**
	MBL webcam2x	14/01/2024	07:00	16/01/2024	11:00	**Yes**
	RUV4	14/01/2024	06:00	14/01/2024	19:00	**Yes**
February *08/02/24 – 08/02/24*	LFI langihryggur	08/02/2024	06:00	09/02/2024	09:00	**Yes**
	MBL webcam1	08/02/2024	06:00	09/02/2024	09:00	**Yes**
	MBL webcam2x	08/02/2024	06:00	09/02/2024	09:00	**Yes**
	RUV4	08/02/2024	06:00	09/02/2024	02:00	**Yes**
	RUV5	08/02/2024	06:00	09/02/2024	02:00	Not needed
March *16/03/24 – 09/05/24*	LFI grindavik	16/03/2024	20:00	16/03/2024	23:00	Facing wrong direction
	LFI langihryggur	16/03/2024	20:00	07/04/2024	00:00	**Yes**
	LFI reykjanes2	16/03/2024	19:00	17/03/2024	13:00	Too zoomed in
	LFI reykjanes3	16/03/2024	19:00	16/03/2024	22:00	Same LOS as Langihryggur
	LFI svartsengi	16/03/2024	20:00	16/03/2024	02:00	Facing wrong direction
	LFI thorbjorn2	16/03/2024	20:00	24/04/2024	00:00	**Yes**
	LFI visir	16/03/2024	20:00	16/03/2024	22:00	Facing wrong direction
	LFI visir2	16/03/2024	20:00	16/03/2024	22:00	Facing wrong direction
	MBL webcam1	16/03/2024	20:00	16/03/2024	09:00	Same as Thorbjorn
	MBL webcam2	16/03/2024	19:00	19/03/2024	22:00	Cannot see propagation
	MBL webcam2x	16/03/2024	19:00	16/03/2024	10:00	Too zoomed out
	MBL webcam3	16/03/2024	19:00	16/03/2024	23:00	Facing wrong direction
	MBL webcam11	16/03/2024	19:00	16/03/2024	22:00	Poor quality
May *29/05/24 – 22/06/24*	LFI reykjanes2	29/05/2024	12:00	31/05/2024	10:00	**Yes**
	LFI thorbjorn2	29/05/2024	12:00	31/05/2024	13:00	**Yes**
	MBL webcam2	29/05/2024	12:00	05/06/2024	00:00	**Yes**
	MBL webcam2x	29/05/2024	17:00	05/06/2024	00:00	Facing wrong way
	MBL webcamA	29/05/2024	12:00	04/06/2024	04:00	Yes
August *22/08/24 – 06/09/24*	LFI langihryggur	22/08/2024	20:00	23/08/2024	00:00	**Yes**
	LFI thorbjorn2	22/08/2024	20:00	23/08/2024	23:00	**Yes**
	LFI vogar	22/08/2024	20:00	04/09/2024	00:00	Facing wrong way
	MBL webcam1	22/08/2024	21:00	29/08/2024	23:00	**Yes**
	MBL webcam11	22/08/2024	21:00	25/08/2024	23:00	**Yes**
	MBL webcam13	22/08/2024	20:00	22/08/2024	23:00	Facing wrong way
Total hours of footage: 2286						

Table 2.1: *The webcam footage available for each of the eruptions and the duration of the eruption they covered. Cameras that were used for analysis have been identified and reasons other cameras were not used stated. Most cameras were disregarded for facing the wrong way, not being correctly zoomed or having poor camera quality. LFI Langihruggur is situated on a ridge to the east of the lava flows; all other used webcams are on Þorbjörn facing different directions during eruptions. Webcam footage has been provided by the Icelandic Met Office (thanks to M. Parks and G. Pedersen).*

2.2 Fissure Propagation Mapping

Throughout the eruptions, the times that a new fissure segment propagated was noted, and its location marked on the IMO-mapped fissures based on matching distinctive topographic features (fig.2.1). Where possible, the times that propagation reached the full northern and southern extent of each fissure segment were also recorded. Smaller segments (<10m) propagated too quickly relative to their length to be mapped due to the resolution limits of the footage. Weather conditions and camera states were logged throughout to account for their impact on the quality of observations.

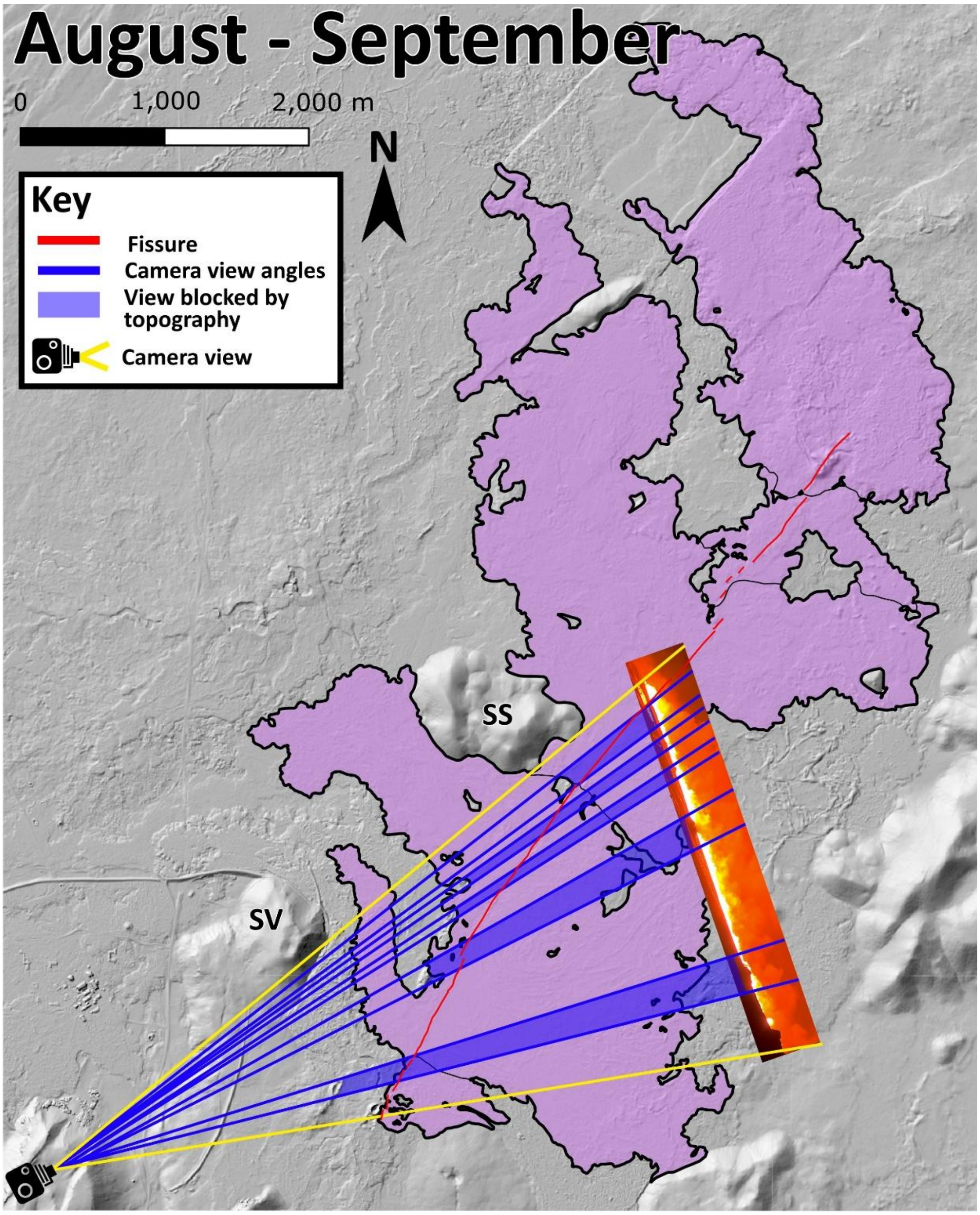

Fig.2.1: *Matching of the topographic highs on the webcam footage with those visible on the DEM to allow for accurate matching of the fissure segments from the footage onto the map, taking into account the apparent length of fissures due to the camera viewing angle. This webcam screenshot was taken from the August – September eruption, on the 22nd August at 22:34:54. Base map DEM from: ÍslandsDEM, 2025*

2.3 Fire Fountain Height Analysis

Fire fountain heights for each fissure segment were measured for approximately three hours from the onset of each eruption. This timeframe captures the initial rapid height increase and subsequent gradual decrease before fissures began concentrating into cones, which complicates further measurements. Adverse weather conditions, such as fog and rain, occasionally shortened this observation window. Measurements were taken using a standard ruler and scaled to real dimensions. The scaling factor was determined by comparing the on-screen fissure segment length to its actual length from the IMO map, adjusting for distortions caused by webcam angles and fissure orientations. This scaling factor was then applied to fire fountain heights to obtain their true value (fig.2.2).

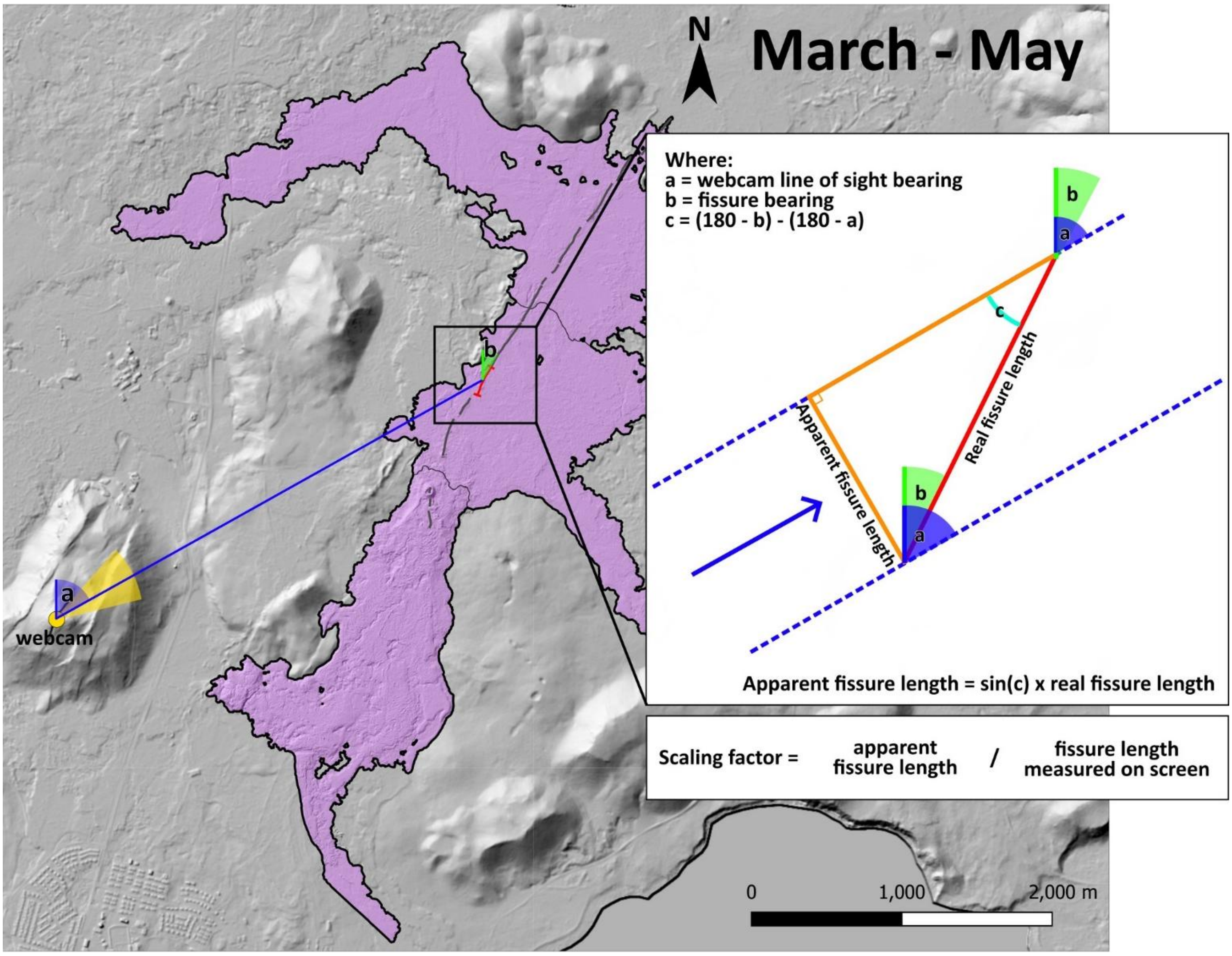

Fig. 2.2: *Example of calculating the apparent fissure length of a fissure from the March – May eruption. This calculation is repeated for every fissure segment, changing the fissure bearing and webcam line of sight bearing appropriately for each calculation. The scaling factor is then calculated for each different fissure segment. Base map DEM from: ÍslandsDEM, 2025*

To capture the rapid height increase when each fissure segment starts to propagate, fire fountain heights were initially measured every ~10 seconds. As the height changes slowed, the interval increased to 30 seconds, 1 minute and finally 5 minutes. To account for the highly pulsatory nature of fire fountains, measurements were consistently taken from the highest fountain within a ten-second window at each interval to minimise stochastic variability. Additional measurements were recorded during notable activity changes.

This study's methods differ from those used by Witt et al. (2018) in their Holuhraun eruption study for several reasons. Firstly, their cameras were positioned nearly perpendicular to the fissure, minimising perspective distortion and allowing them to assume a uniform scaling factor across all vents. In contrast, this study had no control over camera placement, often resulting in highly oblique viewing angles and introducing perspective distortion which required separate scaling factors for each fissure segment to resolve.

Secondly, Witt et al. (2018) enhanced contrast on the footage by isolating the red channel (Witt and Walter, 2017), allowing them to use a Sobel edge detection algorithm (Jin-Yu et al., 2009) to automatically measure fire fountains. This method was impractical here because of the low quality of webcam footage, so manual processing was more accurate.

Finally, Witt et al. (2018) measured fire fountain heights continuously, capturing every part of a pulse, resulting in a large overall standard deviation, but demonstrating that fountain heights were stable over time. However, this study focuses on the decay of fountain heights, making it crucial to capture only the highest point of each pulse.

Due to the nature of the raw data, there are several uncertainties which affect the results:

1) Fissure lengths rely on accurate mapping by the IMO.

2) Exact webcam locations are unknown, so locations have been approximated based on topographic features. However, any angular discrepancies resulting from this have been deemed negligible.
3) +/- 1mm ruler uncertainty that affects measured fire fountain height and fissure length. Fissure length affects scaling factor so larger scaling factors result in larger overall uncertainties.
4) Identification of the top of the fire fountain relies on viewer discretion. This is particularly significant when the cameras are zoomed far out because the lava spray at the top of the fountains, which can be seen easily when zoomed in, often appears as a diffuse glowing cloud.

The ruler uncertainty is the only uncertainty that can be accurately quantified and is the uncertainty reflected in the error bars on plots. These other factors are largely negligible in comparison to the ruler uncertainty and so are less important to be quantified.

2.4 Recommendations

During future eruptions camera operators should ensure that cameras are not zoomed out further than necessary as this leads to large uncertainties. Some cameras should stay stationary throughout the eruption to make fissure mapping and fire fountain measuring throughout the eruption easier, and others should follow the fissure propagation and zoom to see more details. More cameras should be instated further north so view angles are perpendicular to fissures, as apparent fissure lengths are currently up to seven times shorter than the real fissure lengths.

Fissure eruptions are surface expressions of subsurface dikes. They are usually located immediately above their feeder dike and erupt to the surface through long, but often disjointed, cracks that develop at the start of an eruption (Tyrell, 1937). Fissure locations are controlled by a range of factors including: direction of least compressive stress (Anderson, 1951), preexisting structural weaknesses in the crust (Delaney et al., 1986; Ziv and Rubin, 2000), crustal loading (Klügel et al., 2005; Walter and Amelung, 2006; Jenness and Clifton, 2009), and topography (Gaffney and Damjanac, 2006). However, as expected, fissures don’t open everywhere at the same time, but rather propagate from some starting location outwards.

Throughout this section, a fissure refers to the full extent of the fissure which is broken up into sections. A fissure segment refers to an individual section of the total fissure.

3.1 Propagation Start Locations

The most frequent initial fissure opening location is between Svartsengisfell and Stóra Skógafell (fig.3.1), aligning with the place where most lava is thought to have extruded during the Sundhnúkur Fires (2350B.P.; Jenness and Clifton, 2009). Surface deformation, due to magma reservoir inflation, is always centred over Mt Þorbjorn (fig.3.1), making the start location in the January eruption closest to the magma reservoir. The other eruptions start further north suggesting some crustal weakness may make this longer path preferable for most eruptions.

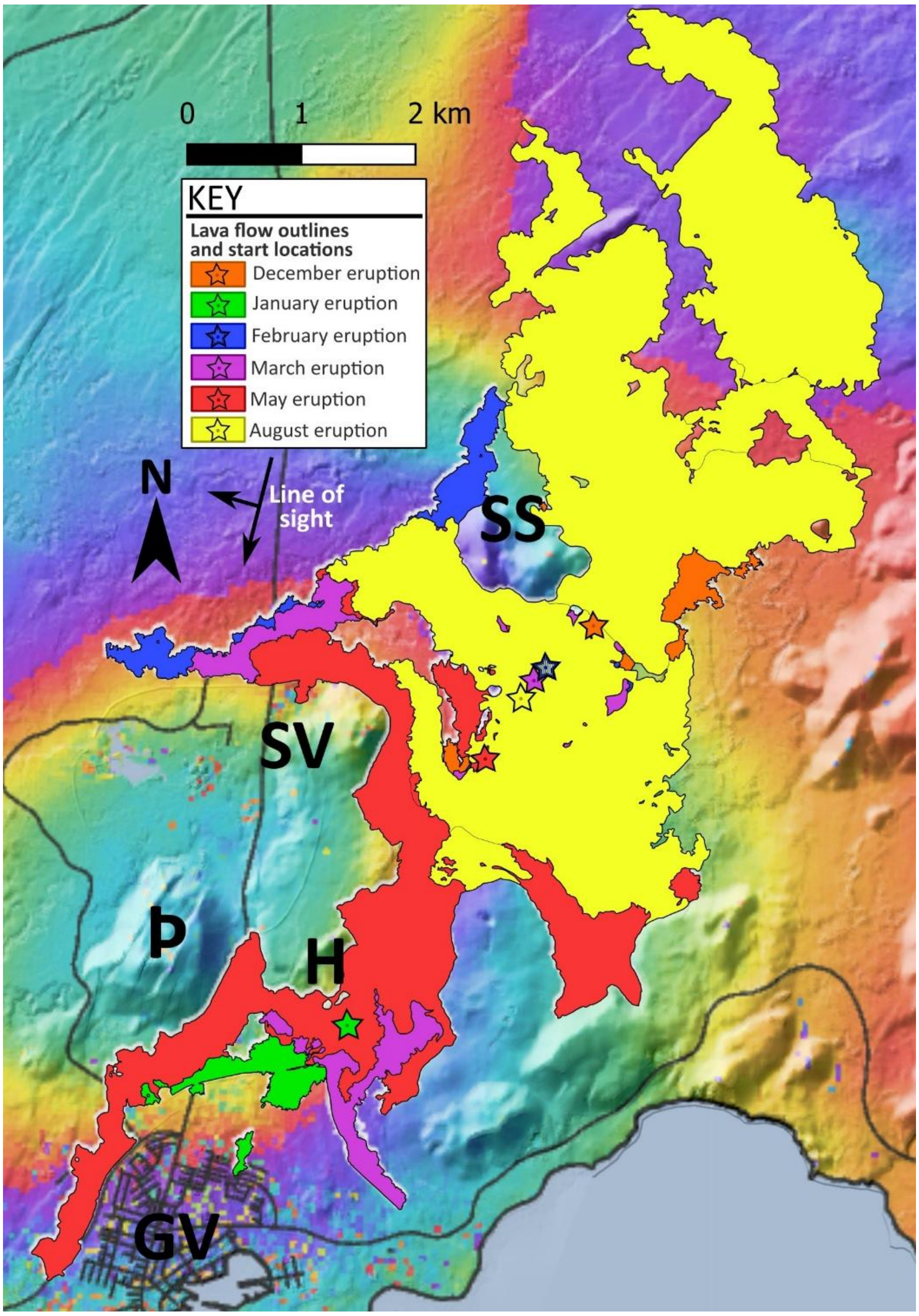

Fig.3.1: *Start locations of the eruptions of the SVS along with their lava flow outlines. Background is an interferogram from 13 – 25 June 2024 (IMO, 2024) to show the pre-eruption ground inflation proximity to eruption start locations. Inflation in this period was roughly 3 – 4 cm. The start location of the February eruption is shown with a hashed star because the starting location is uncertain due to unfocused webcam footage. Þ = Þorbjörn, SV = Svartsengisfell, SS = Stóra Skógafell, H = Hagafell, GV = Grindavík.*

3.2 Fissure Propagation Speeds

Fissure propagation is controlled by factors including: magma pressure, tectonic movement, crustal stress fields, normal faults (Pedicini et al., 2023), and crustal geology (Tentler and Temperley, 2006).

High resolution fissure propagation measurements have been taken every few seconds during the start of the December 2023, January 2024, March 2024, and August 2024 eruptions. Propagation, both on each segment and as a whole fissure, advances in discrete bursts, separated by short periods of repose (fig.3.2, fig.3.3). Although apparent in each of these eruptions, the pulses of enhanced fissure propagation are most obvious during the December eruption (fig.3.3a), where fissure propagation occurs in four discrete periods. Tentler and Temperley (2007) suggest that the absence of fissure activity at the surface occurs when the vertical body force stress in the ascending magma cannot overcome the horizontal compressive stress in the crust. Because the propagation pulses occur on fissure segments that are significant distances apart (Dec1a, and Dec6a and Dec6b, advancing at the same time from opposite ends of the fissure), it is unlikely that crustal obstructions are responsible for the periods of repose, and that a magma system origin is more likely.

Generally, fissure propagation is fastest close to the start of fissure opening and slows through time during the eruption (fig.3.3). This finding supports work by Einarsson (1991), that suggests propagation slows as a dike lengthens and the magma chamber pressure drops. The fastest fissure propagation speed measured was at the very start of the August eruption at >8000m/min (fig.3.3d). However, it is often hard to accurately capture the propagation speed of the first fissure because the cameras typically take quite a few seconds to focus, but this leads to underestimates rather than overestimates.

Within fissure segments, variations in propagation speed show no commonality with other segments at the same time. If these variations were being driven by the magma system, the same increases or decreases in propagation speed should be visible on different fissure segments at the same time. Variation of this type is absent here, suggesting variations are most likely controlled by small crustal heterogeneities that introduce resistance into the proceeding fissure, like small cross-cutting faults and variations in lithology.

Therefore, long term variations in the propagation of the whole fissure seem to be controlled by changes in the magma stress, whereas, variations on individual fissure segments are most likely controlled by crustal heterogeneities.

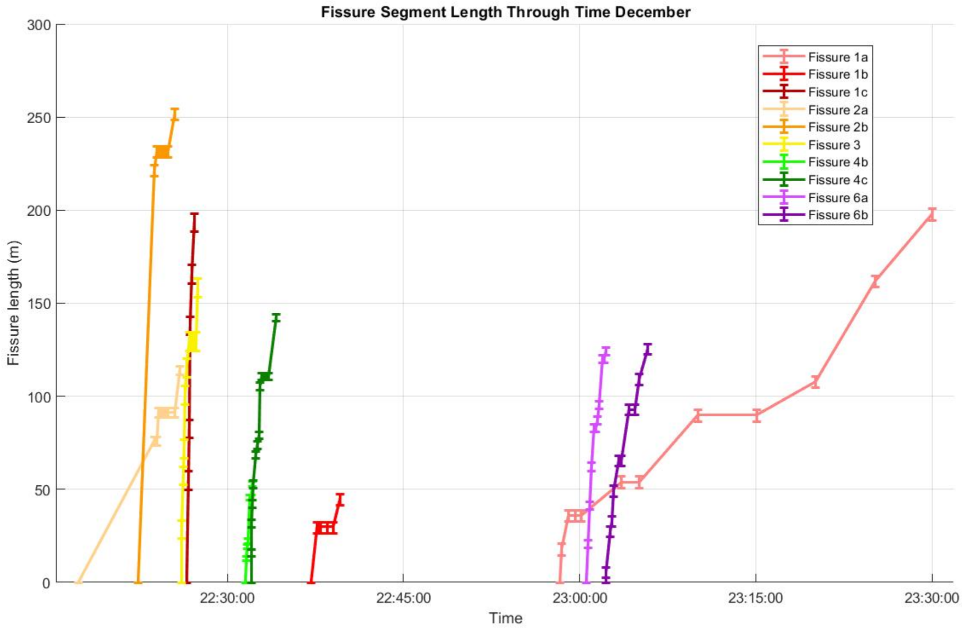

Fig.3.2a: *Fissure segment length through time during fissure propagation in the December 2023 eruption*

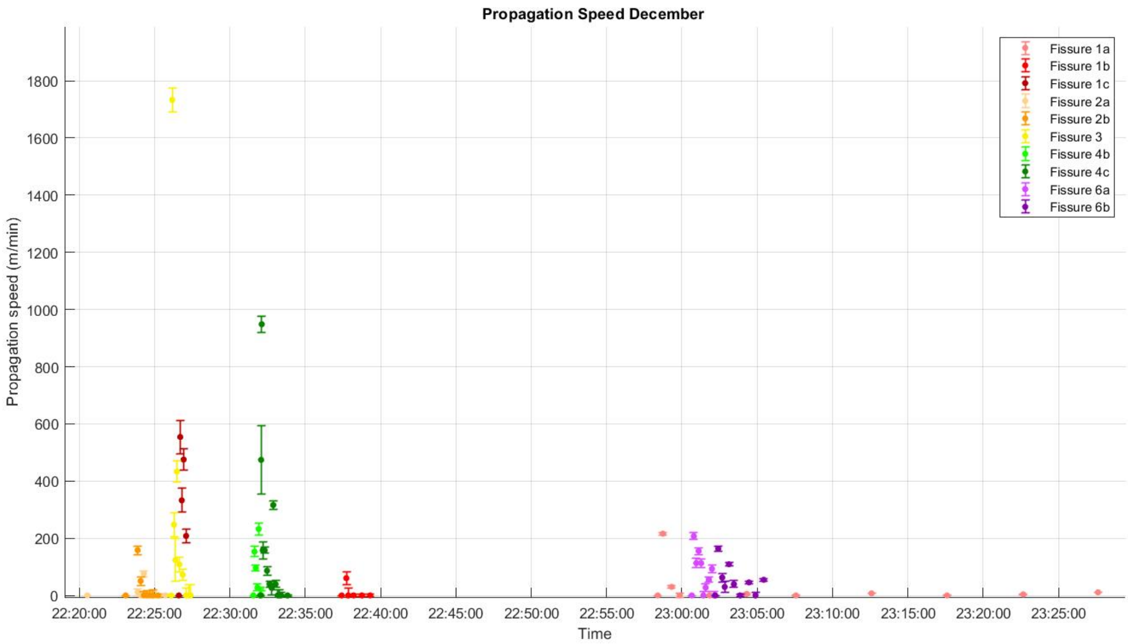

Fig.3.3a: *Fissure propagation speed through time during the December 2023 eruption, for each fissure segment*

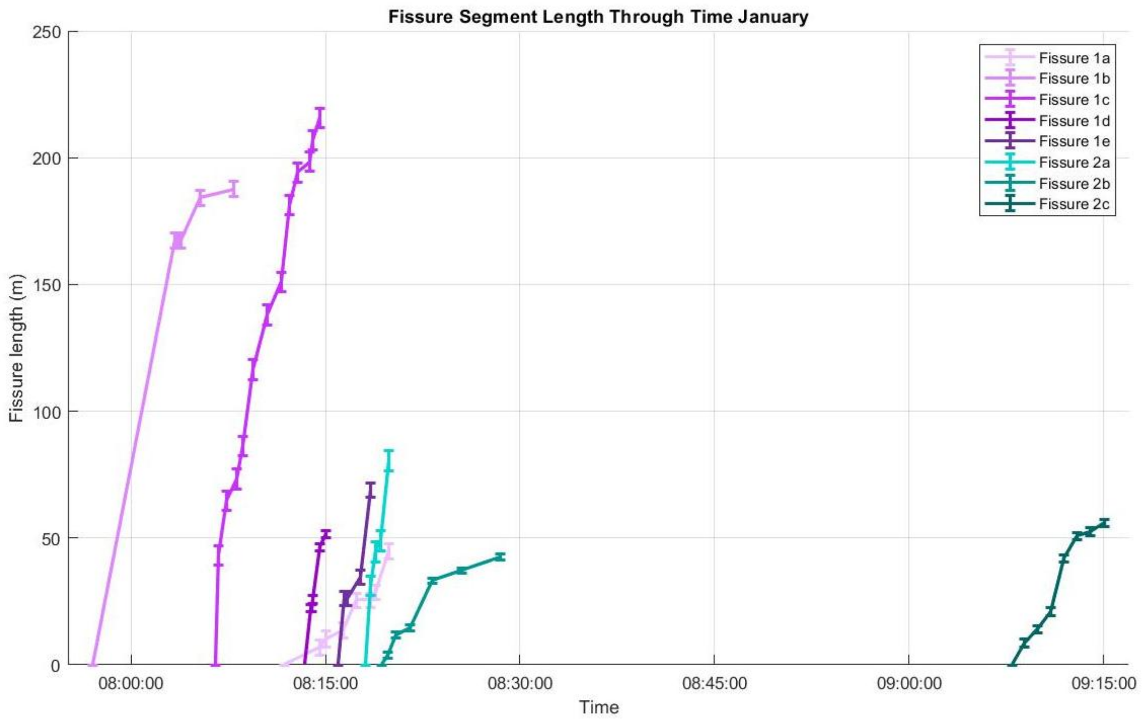

Fig.3.2b: *Fissure segment length through time during fissure propagation in the January 2024 eruption*

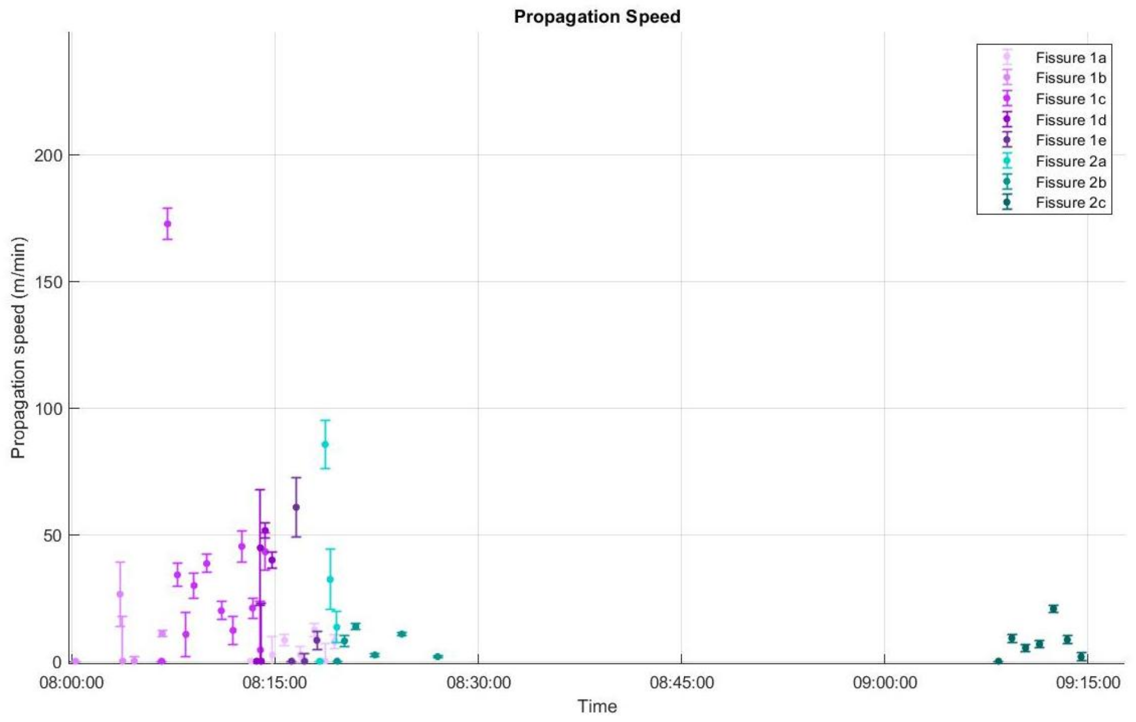

Fig.3.3b: *Fissure propagation speed through time during the January 2024 eruption, for each fissure segment*

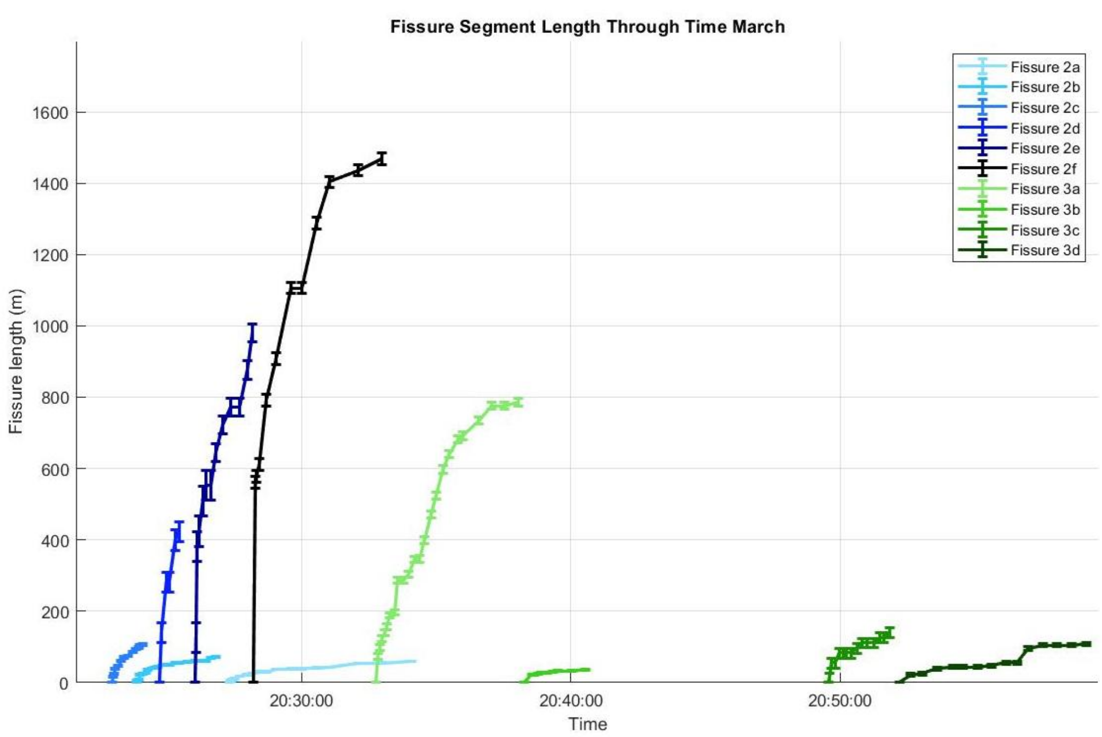

Fig.3.2c: *Fissure segment length through time during fissure propagation in the March 2024 eruption*

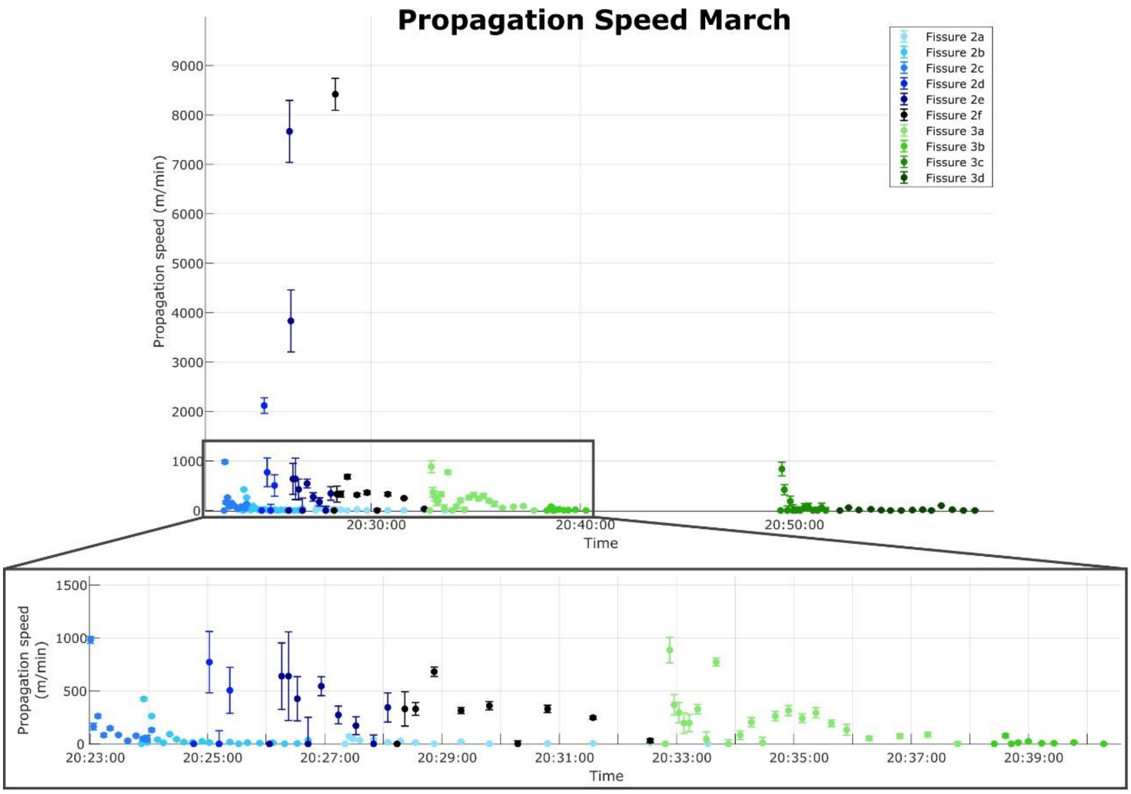

Fig.3.3c: *Fissure propagation speed through time during the March 2024 eruption, for each fissure segment. Zoom in box provided for clarity.*

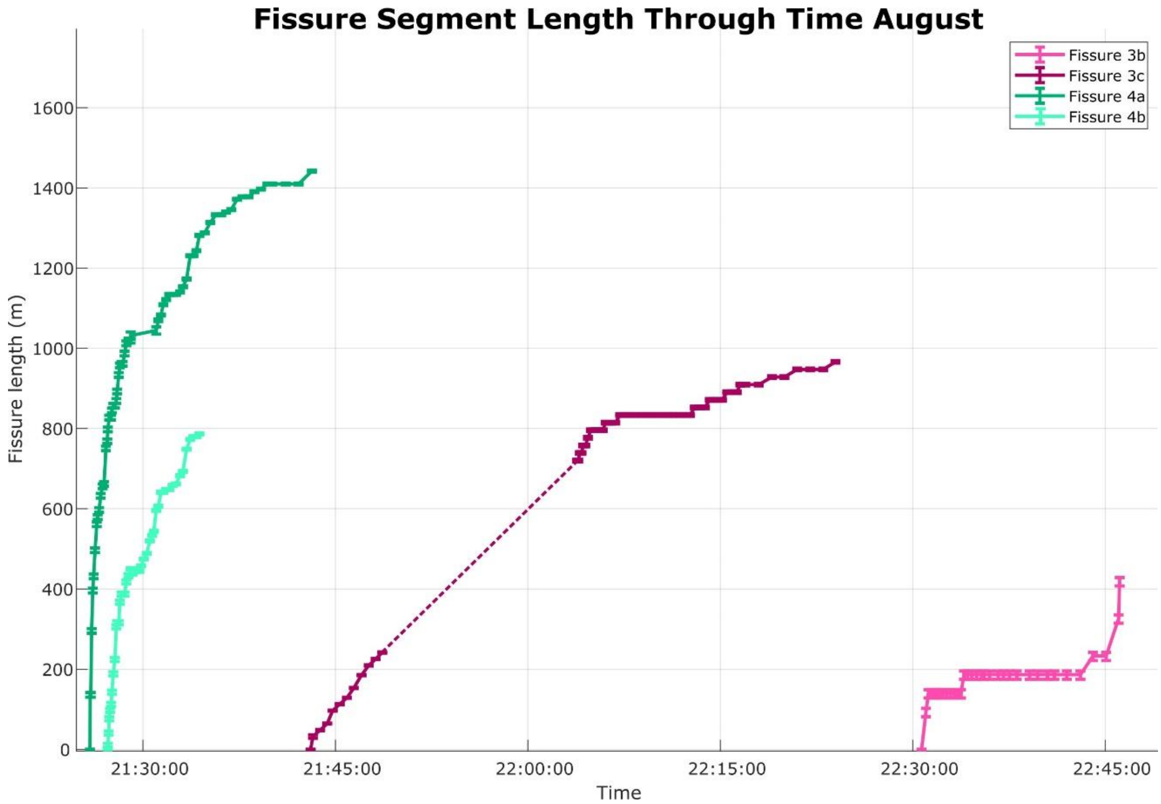

Fig.3.2d: *Fissure segment length through time during fissure propagation in the August 2024 eruptiont. The dashed line shows extrapolated propagation during a time when the fissure could not be seem because of the camera angle*

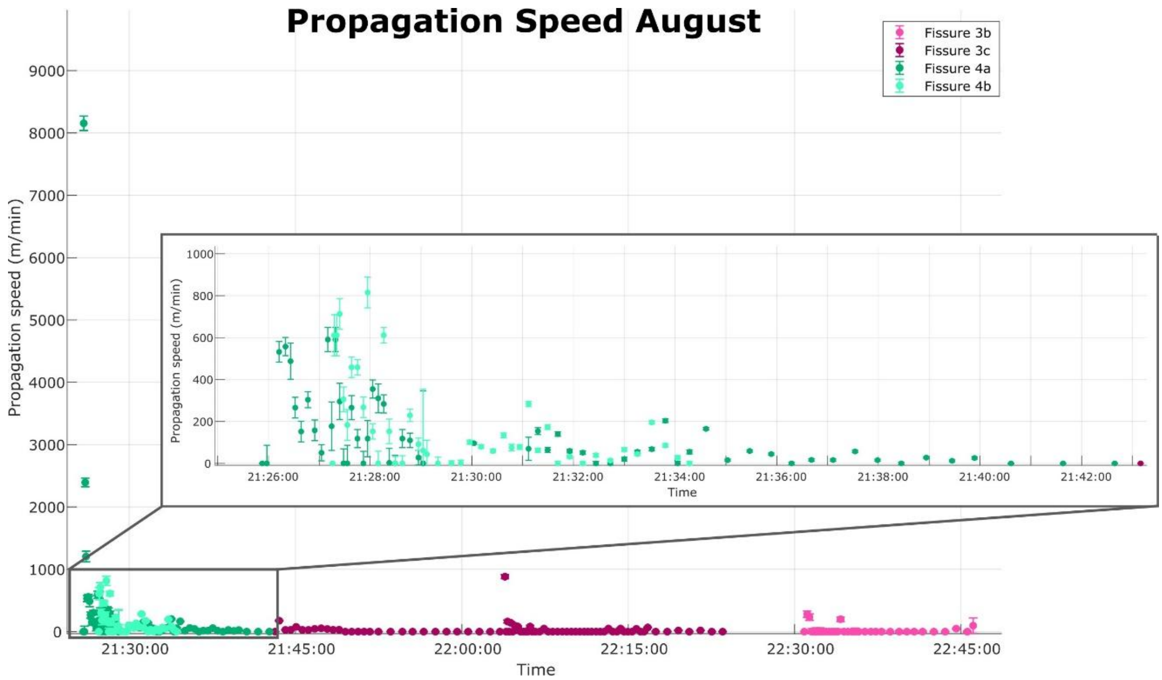

Fig.3.3d: *Fissure propagation speed through time during the August 2024 eruption, for each fissure segment. Zoom in box provided for clarity.*

3.3 Fissure Propagation Directions

Fissure segments typically open in one of two ways: either from one end, propagating toward the other, or from the centre, unzipping outwards (fig.3.3). In all eruptions except the August eruption (fig.3.3f), fissure opening consistently began roughly two-thirds of the way up (north) the fissure. Propagation then predominantly advanced southward, with more limited propagation to the north.

Despite this dominant southward trend, in the December, January (excluding the later Grindavík segment), and February eruptions (fig.3.3a-c), propagation ceased at both ends at around the same time. This suggests that crustal resistance may have inhibited northward progression. However, this pattern was not observed in the March and May eruptions (fig.3.3d,e), implying that repeated fissure activity near Stóra Skógafell has weakened the crust. The August eruption (fig.3.3f) deviated from this trend; the initial fissure was only one-third of the way from the southern end and propagation predominantly advanced northwards. This led to the exploitation of previously unused crust.

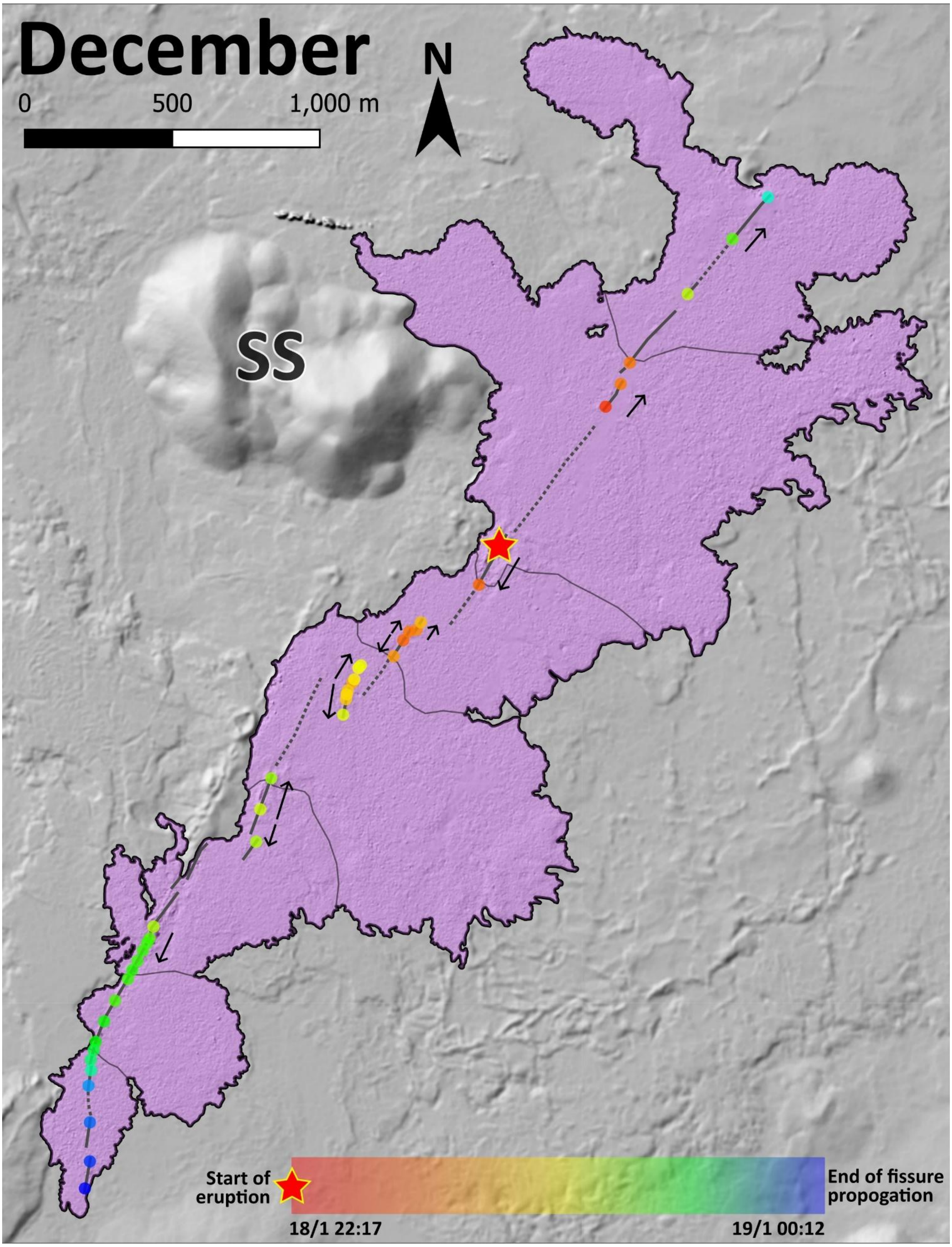

Fig.3.3a: *Fissure propagation during the December 18th – 21st 2023 eruption of the SVS. The start location of the eruption is shown with a star, and the fissure propagation is shown with the coloured dots, coloured according to a coloured time scale. Dots appear in locations where it was possible to identify the location of fissure propagation at any time, usually at the ends of the fissure segment or approximate locations where individual segments opened. Fissured are outlined in grey, with uncertain fissures shown with a dashed line. Arrows are shown for easy interpretation of propagation directions. The outline of the final lava extent is shown in purple. SS = Stóra Skógafell. Base map DEM from: ÍslandsDEM, 2025*

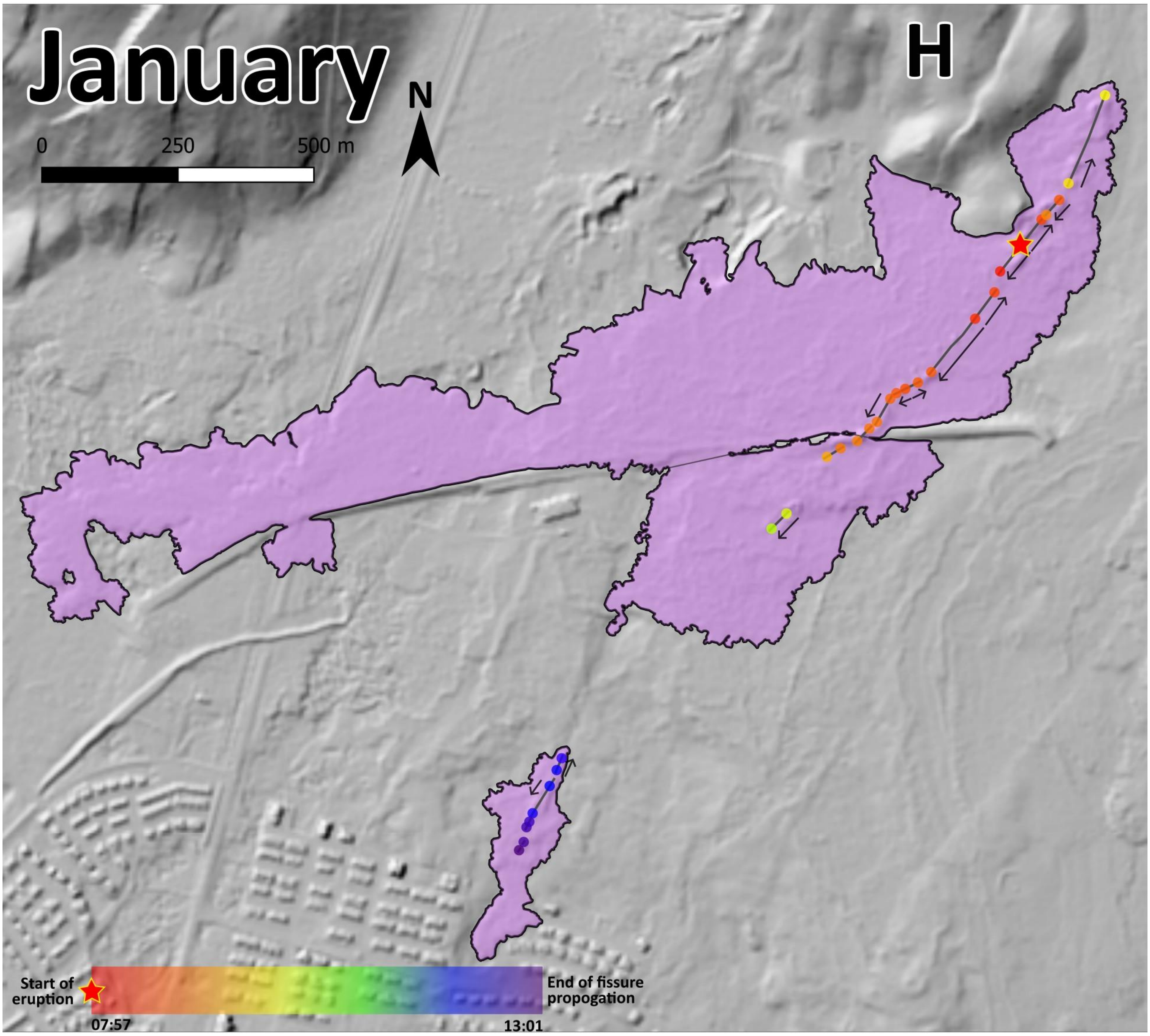

Fig.3.3b: *Fissure propagation during the January 14th – 16th 2024 eruption of the SVS. The start location of the eruption is shown with a star, and the fissure propagation is shown with the coloured dots, coloured according to a coloured time scale. Dots appear in locations where it was possible to identify the location of fissure propagation at any time, usually at the ends of the fissure segment or approximate locations where individual segments opened. Fissured are outlined in grey. Arrows are shown for easy interpretation of propagation directions. The outline of the final lava extent is shown in purple. H = Hagafell. Base map DEM from: ÍslandsDEM, 2025*

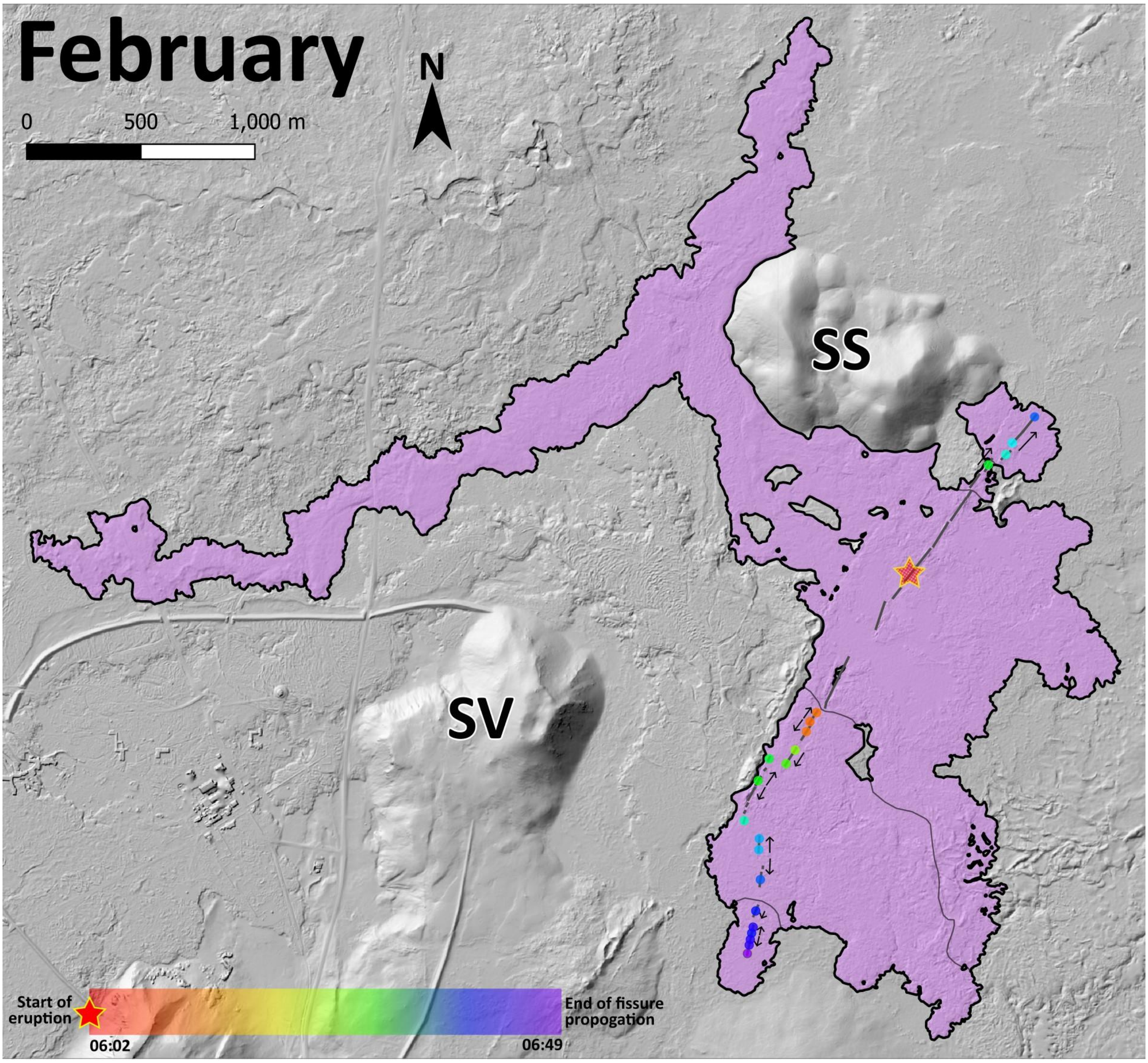

Fig.3.3c: *Fissure propagation during the February 8th – 9th 2024 eruption of the SVS. The start location of the eruption is shown with a star, and the fissure propagation is shown with the coloured dots, coloured according to a coloured time scale. Dots appear in locations where it was possible to identify the location of fissure propagation at any time, usually at the ends of the fissure segment or approximate locations where individual segments opened. Fissured are outlined in grey. Arrows are shown for easy interpretation of propagation directions. The outline of the final lava extent is shown in purple. SV = Svartsengisfell; SS = Stóra Skógafell. Base map DEM from: ÍslandsDEM, 2025*

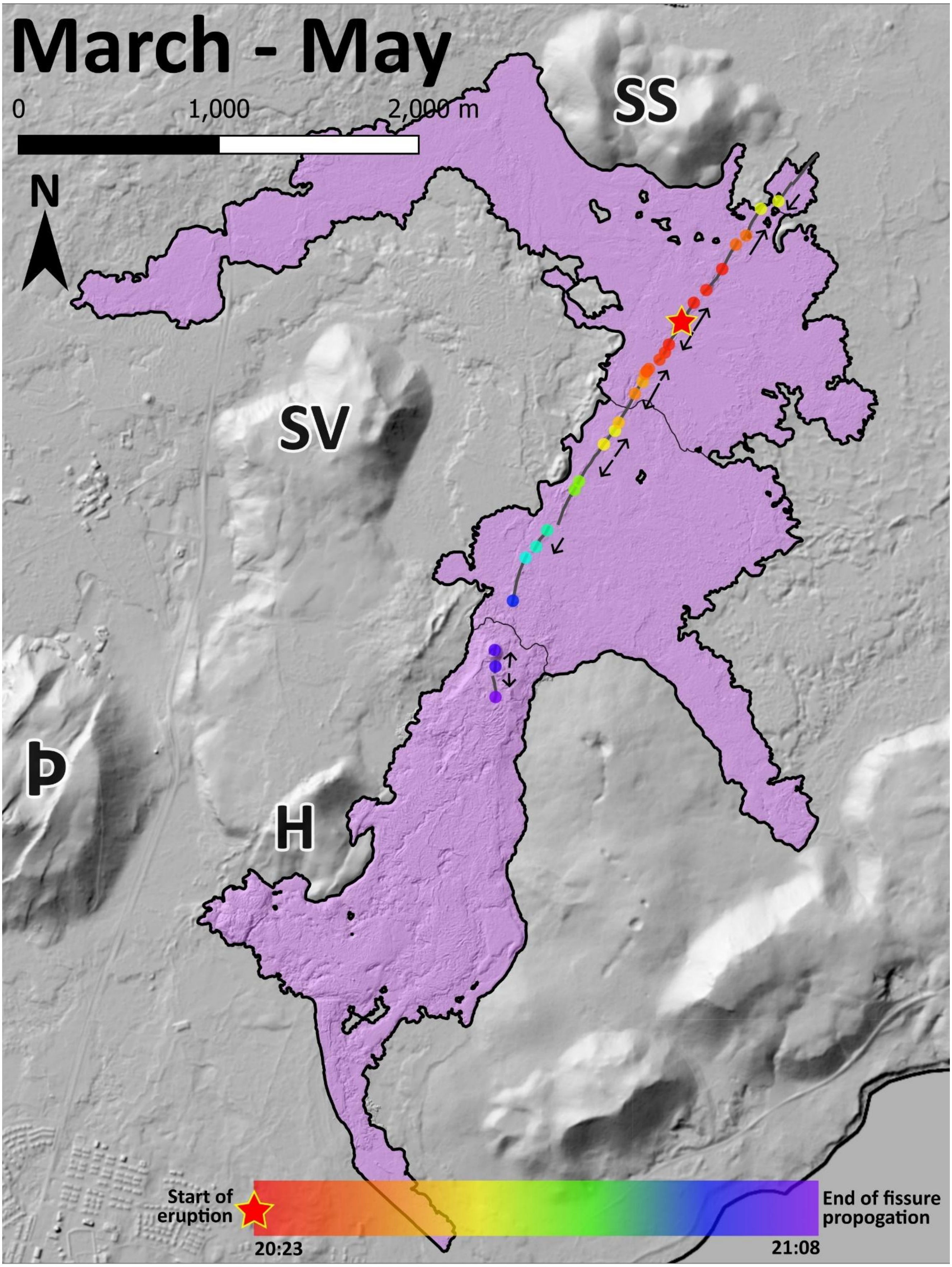

Fig.3.3d: *Fissure propagation during the March 16th – May 9th 2024 eruption of the SVS. The start location of the eruption is shown with a star, and the fissure propagation is shown with the coloured dots, coloured according to a coloured time scale. Dots appear in locations where it was possible to identify the location of fissure propagation at any time, usually at the ends of the fissure segment or approximate locations where individual segments opened. Fissured are outlined in grey. Arrows are shown for easy interpretation of propagation directions. The outline of the final lava extent is shown in purple. Þ = Þorbjörn; H = Hagafell; SV = Svartsengisfell; SS = Stóra Skógafell. Base map DEM from: ÍslandsDEM, 2025*

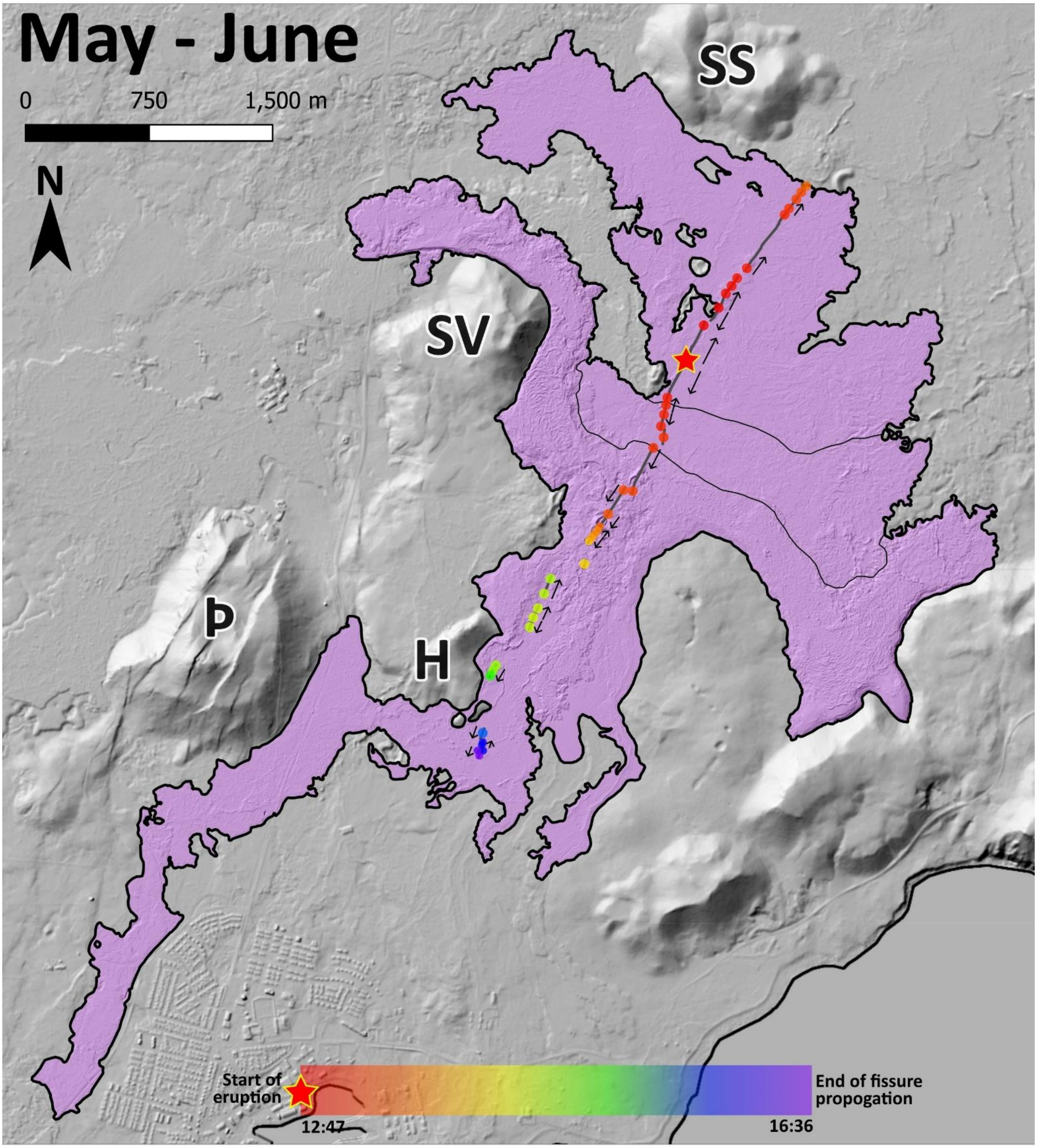

Fig.3.3e: *Fissure propagation during the May 29th – June 22nd 2024 eruption of the SVS. The start location of the eruption is shown with a star, and the fissure propagation is shown with the coloured dots, coloured according to a coloured time scale. Dots appear in locations where it was possible to identify the location of fissure propagation at any time, usually at the ends of the fissure segment or approximate locations where individual segments opened. Fissured are outlined in grey. Arrows are shown for easy interpretation of propagation directions. The outline of the final lava extent is shown in purple. Þ = Þorbjörn; H = Hagafell; SV = Svartsengisfell; SS = Stóra Skógafell. Base map DEM from: ÍslandsDEM, 2025*

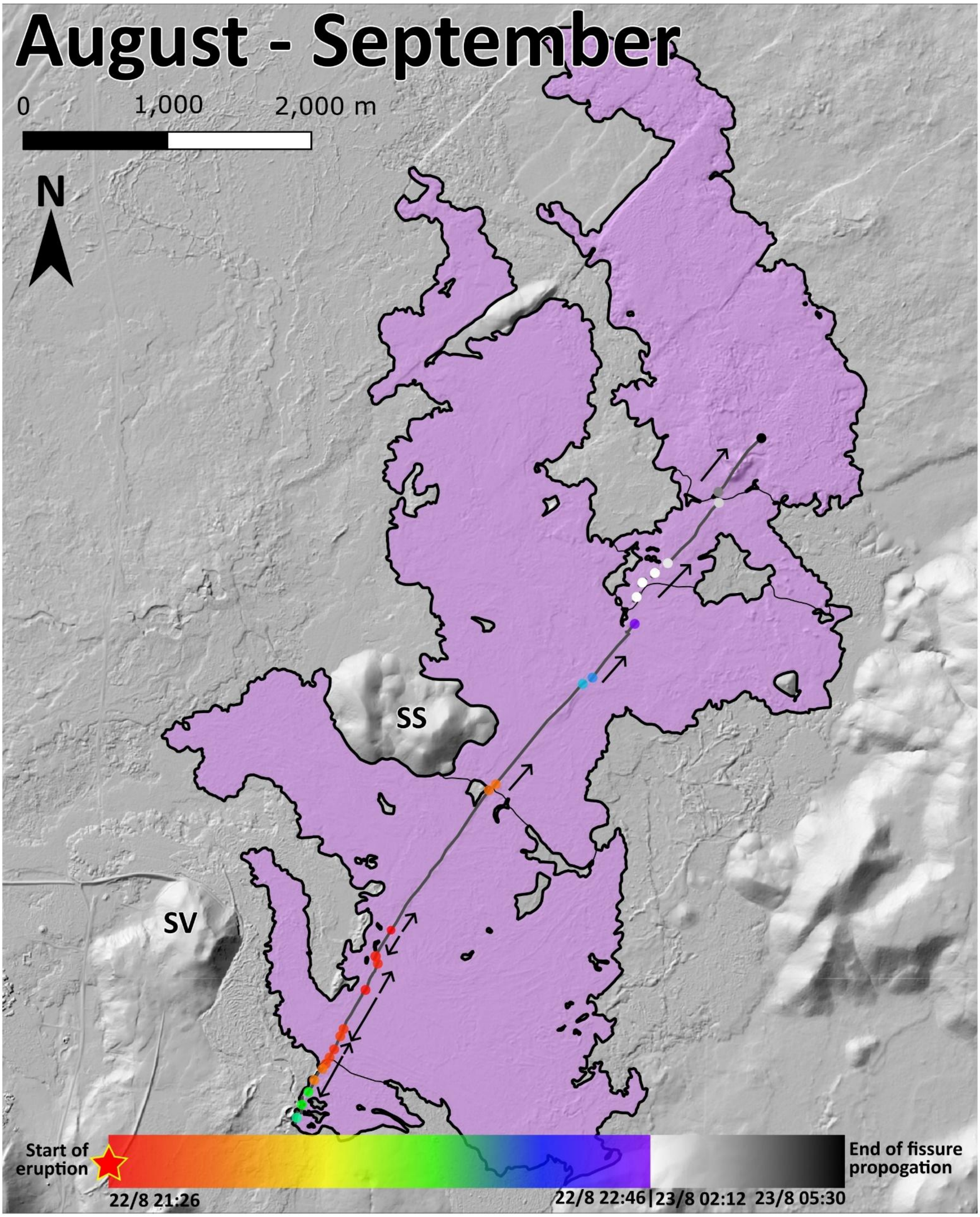

Fig.3.3f: *Fissure propagation during the August 22nd – September 6th 2024 eruption of the SVS. The start location of the eruption is shown with a star, and the fissure propagation is shown with the coloured dots, coloured according to a coloured time scale. Dots appear in locations where it was possible to identify the location of fissure propagation at any time, usually at the ends of the fissure segment or approximate locations where individual segments opened. Fissured are outlined in grey. Arrows are shown for easy interpretation of propagation directions. The outline of the final lava extent is shown in purple. SV = Svartsengisfell; SS = Stóra Skógafell. Base map DEM from: ÍslandsDEM, 2025*

3.4 Fissure Propagation in Relation to Dike Propagation

The propagation of a dike changes the stress field in the surrounding rock, triggering swarms of migrating earthquakes (Belachew et al., 2012; Roman and Cashman, 2006). The propagation of the dike prior to eruption onset can be tracked using migrating seismicity recorded by the IMO South Iceland Lowlands Earthquake Catalogue (IMO, 2024b). However, the error in these automatically detected earthquake locations must be taken into consideration when looking at earthquake data, especially given the mismatch between the earthquakes and the dike traces generated based on geodetic modelling (Parks et al., 2025; see section 3.5.6). On the Reykjanes Peninsula, the lateral location uncertainty is on the order of +/- ~300m (Pers. Comm. M. Parks).

Seismicity before the December eruption was high magnitude, and concentrated (fig.3.4a). Dike propagation began east of Stóra Skógafell, near where the first fissure segment opened, then propagated quickly south and more slowly north, mirroring fissure propagation. The dike continued to propagate southwards through Hagafell after the fissure had stopped propagating.

The January eruption's feeder dike was much longer than its fissure (fig.3.4b). Over ~5 hours, the dike propagated south from east of Svartsengisfell, reaching near its full extent before fissure opening began.

Before the February eruption, seismicity was primarily north of the dike, with limited seismicity on the dike itself (fig.3.4c). Early, concentrated seismicity NE of Stóra Skógafell suggested the eruption might start there, but instead it began south of Stóra Skógafell.

Seismicity before the March eruption was minimal due to a previous dike intrusion 14 days earlier that did not erupt. Geodetic modelling suggests the March 16 dike reused this pathway, reducing induced seismicity. Seismicity tracked the dike's propagation from north to south, which was copied during fissure propagation (fig.3.4d).

The May eruption was preceded by intense seismicity concentrated over Hagafell, potentially explaining why a fissure segment exploited the normal fault there. The dike propagated mainly south from near where the first fissure segment opened. This pattern was repeated in fissure propagation (fig.3.4e).

Before the August eruption, seismicity was intense in the north but limited in the south because the dike propagated further northeast than in previous events (Parks et al., 2025), while the southern crust has been repeatedly weakened by previous activity. The dike propagated from close to where the eruption started, predominantly northwards, similar to the fissure propagation (fig.3.4f).

Generally, fissure propagation follows the same path as dike propagation and early seismicity can be used to predict where the first fissure segment will open. However, exceptions like January and February highlight the need to also consider deformation when identifying a dike. Over time, precursor seismicity has weakened, reducing its predictive reliability.

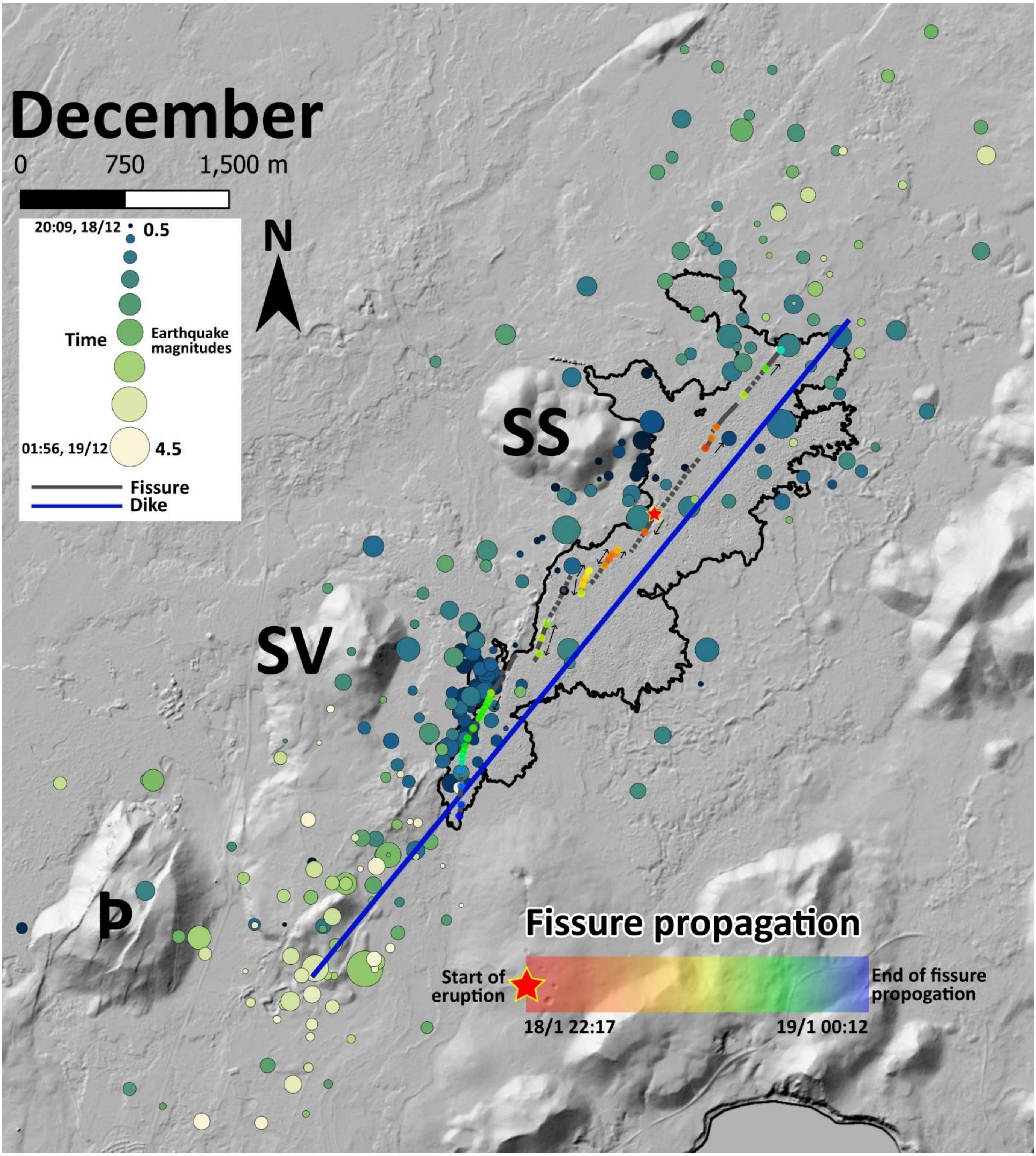

Fig.3.4a: *Seismicity from the injection of the December 18th 2023 dike overlain by fissure propagation. Dot sizes are relative to earthquake size as per the key. Dike location: Parks et al., 2025; Seismicity: IMO, 2024b. Base map DEM from: ÍslandsDEM, 2025*

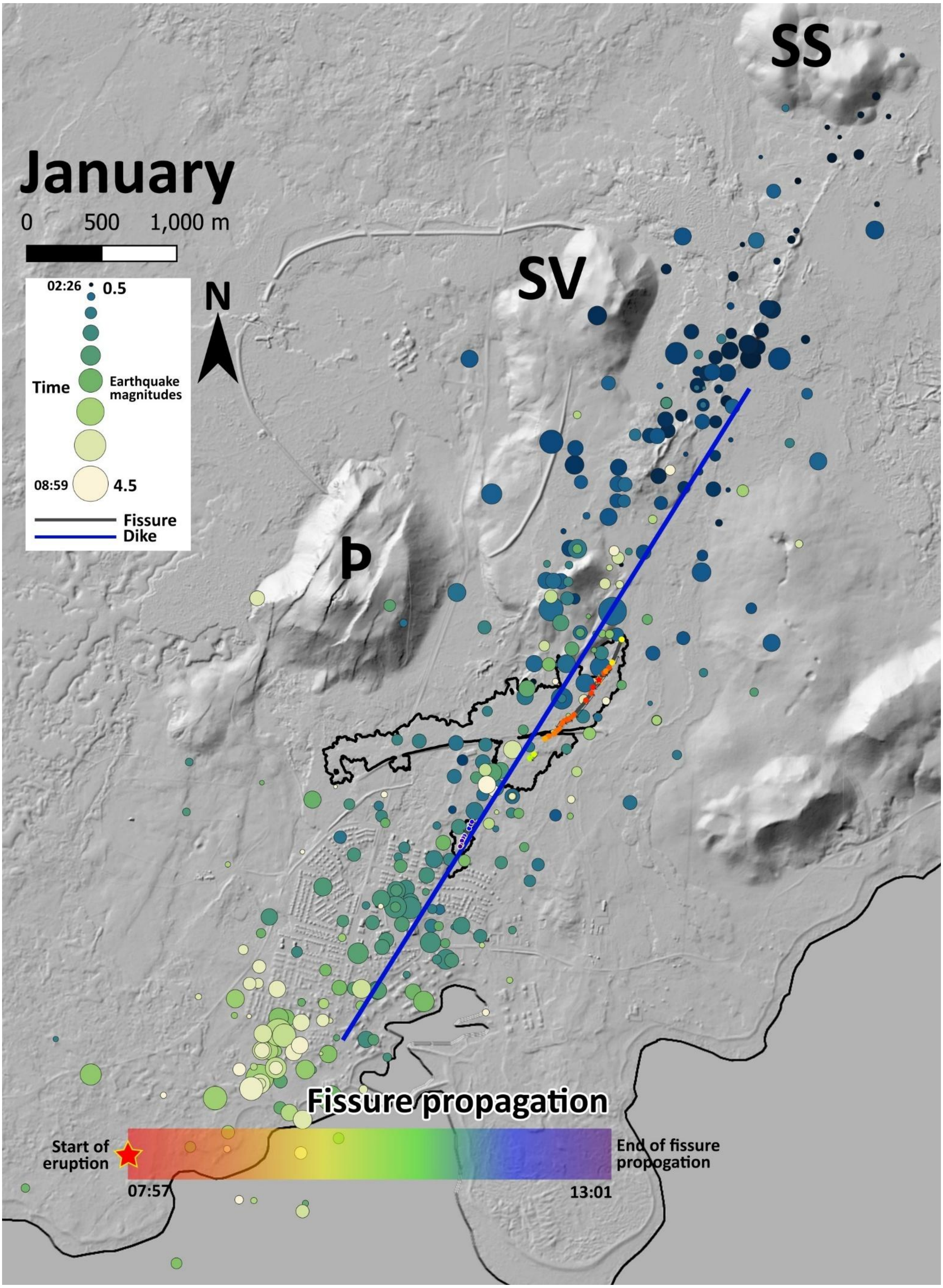

Fig.3.4b: *Seismicity from the injection of the January 14th 2024 dike overlain by fissure propagation. Dot sizes are relative to earthquake size as per the key. Dike location: Parks et al., 2025; Seismicity: IMO, 2024b. Base map DEM from: ÍslandsDEM, 2025*

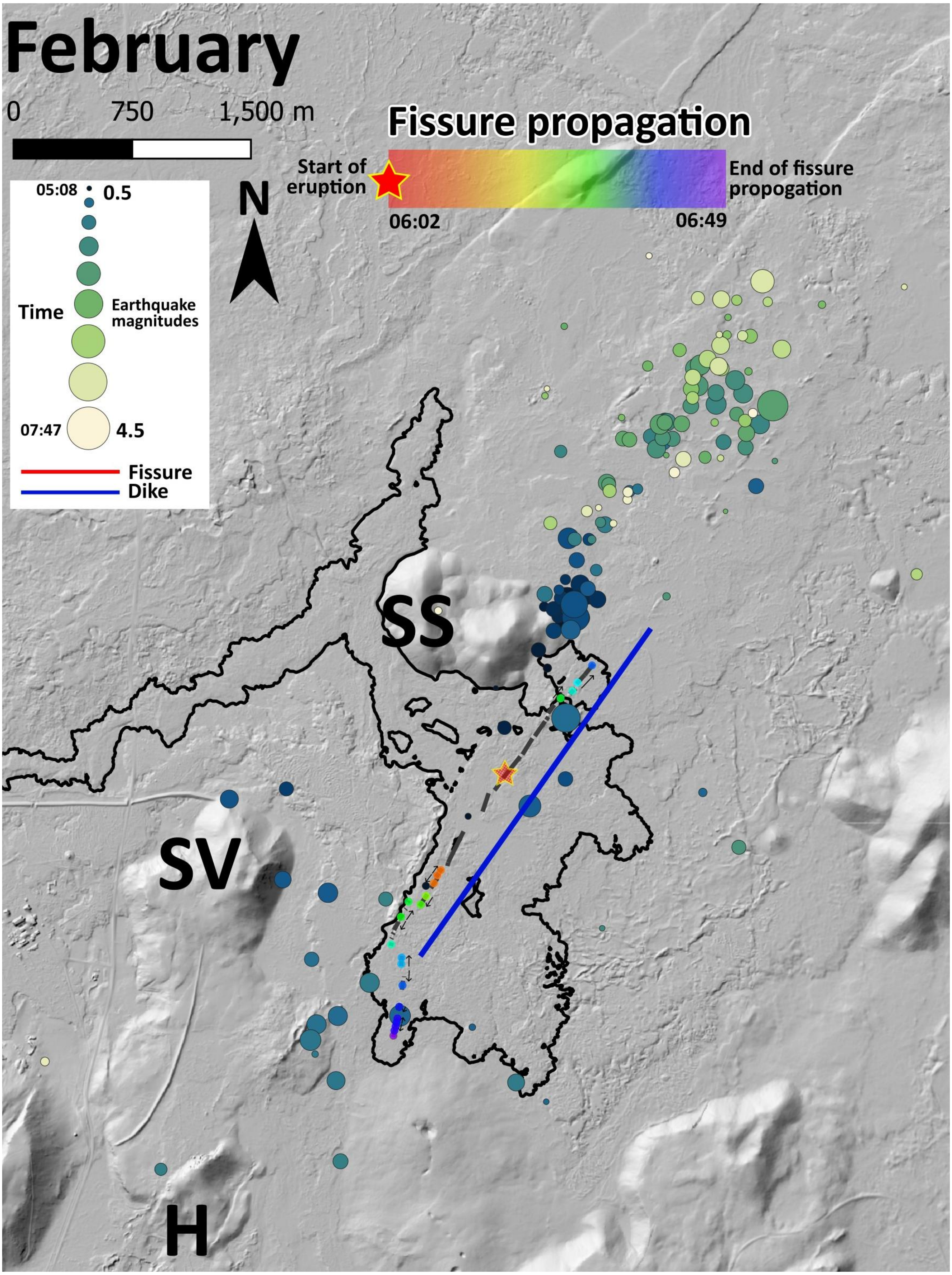

Fig.3.4c: *Seismicity from the injection of the February 8th 2024 dike overlain by fissure propagation. Dot sizes are relative to earthquake size as per the key. Dike location: Parks et al., 2025; Seismicity: IMO, 2024b. Base map DEM from: ÍslandsDEM, 2025*

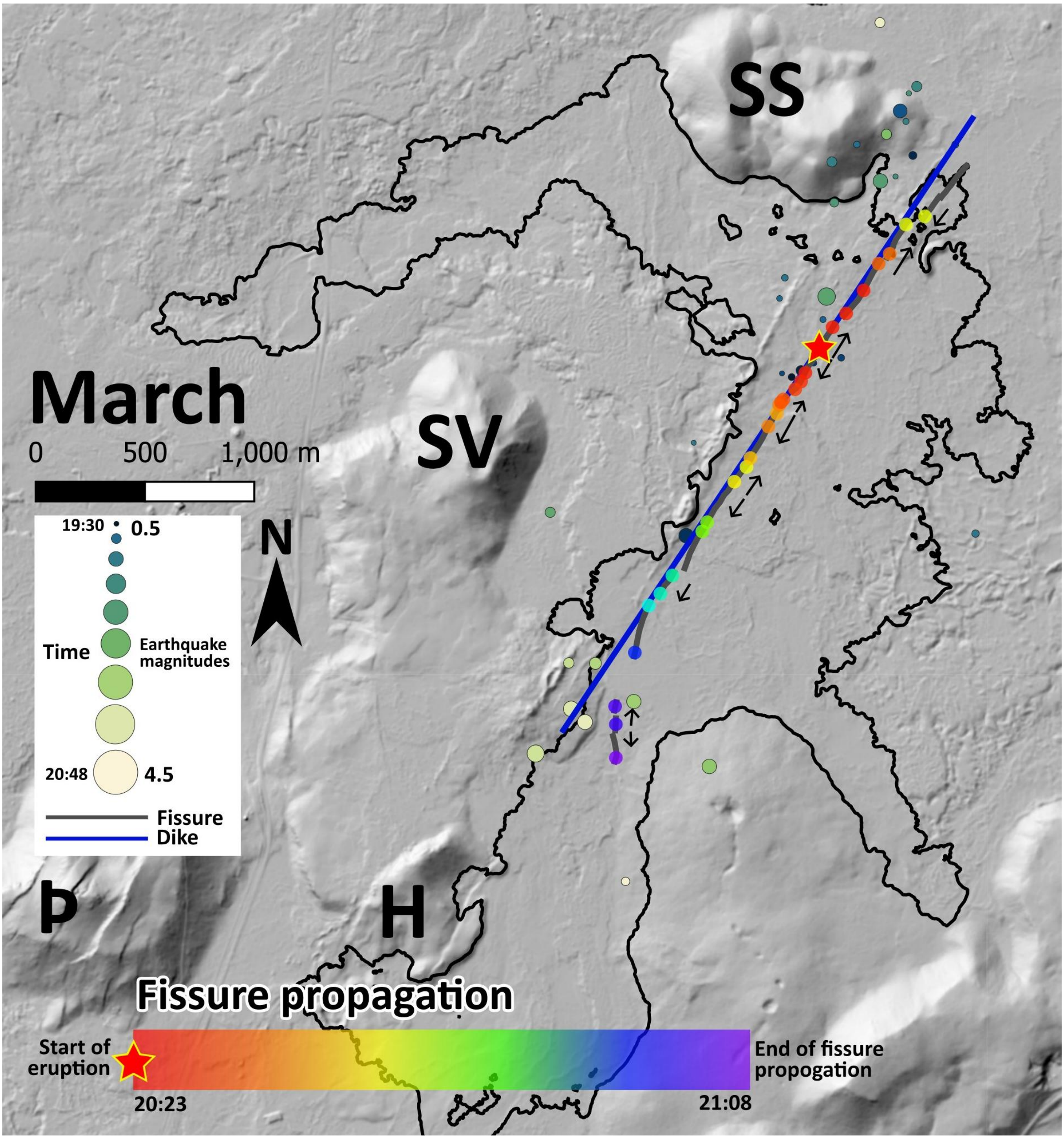

Fig.3.4d: *Seismicity from the injection of the March 16th 2024 dike overlain by fissure propagation. Dot sizes are relative to earthquake size as per the key. Dike location: Parks et al., 2025; Seismicity: IMO, 2024b. Base map DEM from: ÍslandsDEM, 2025*

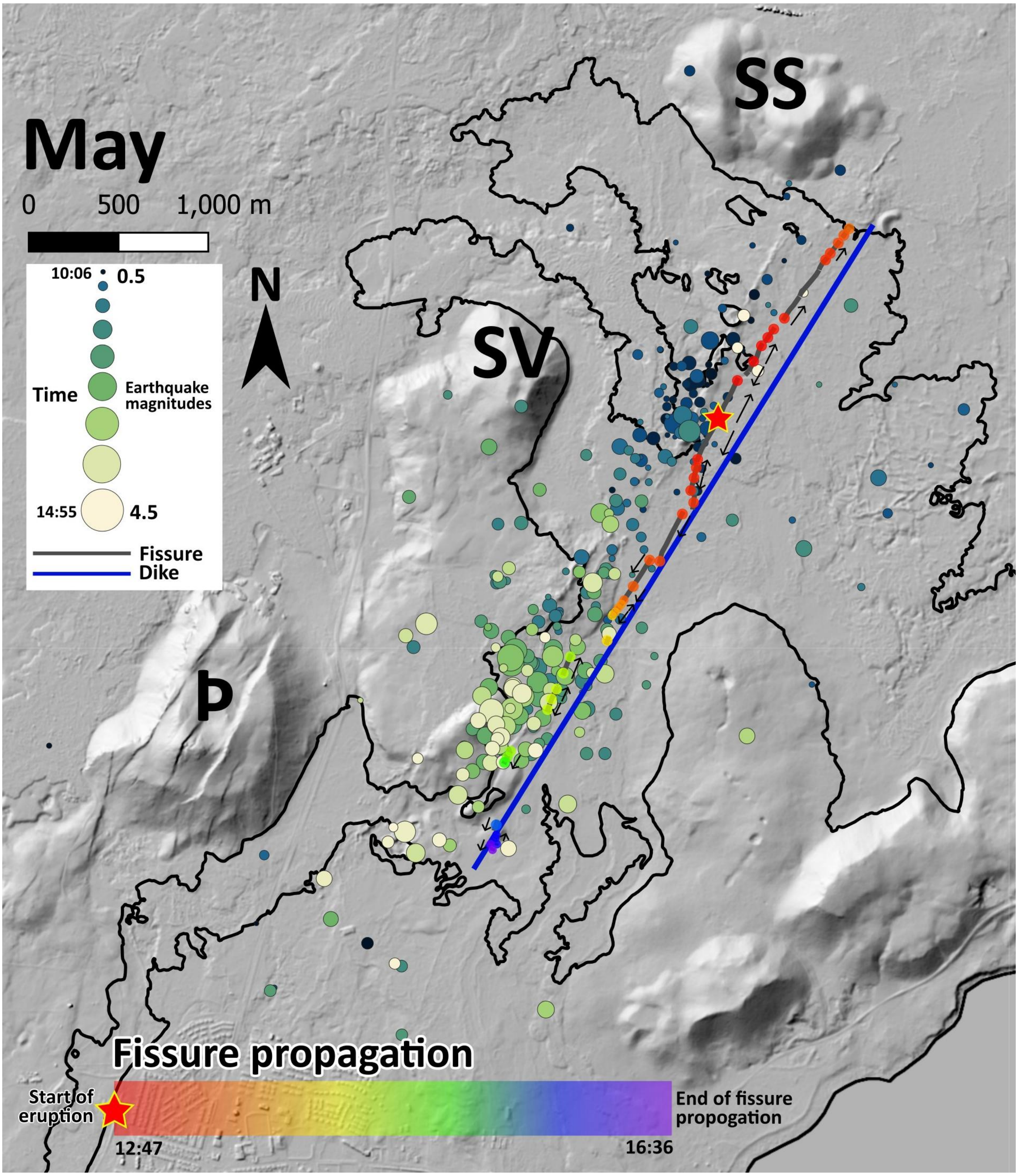

Fig.3.4e: *Seismicity from the injection of the May 29th 2024 dike overlain by fissure propagation. Dot sizes are relative to earthquake size as per the key. Dike location: Parks et al., 2025; Seismicity: IMO, 2024b. Base map DEM from: ÍslandsDEM, 2025*

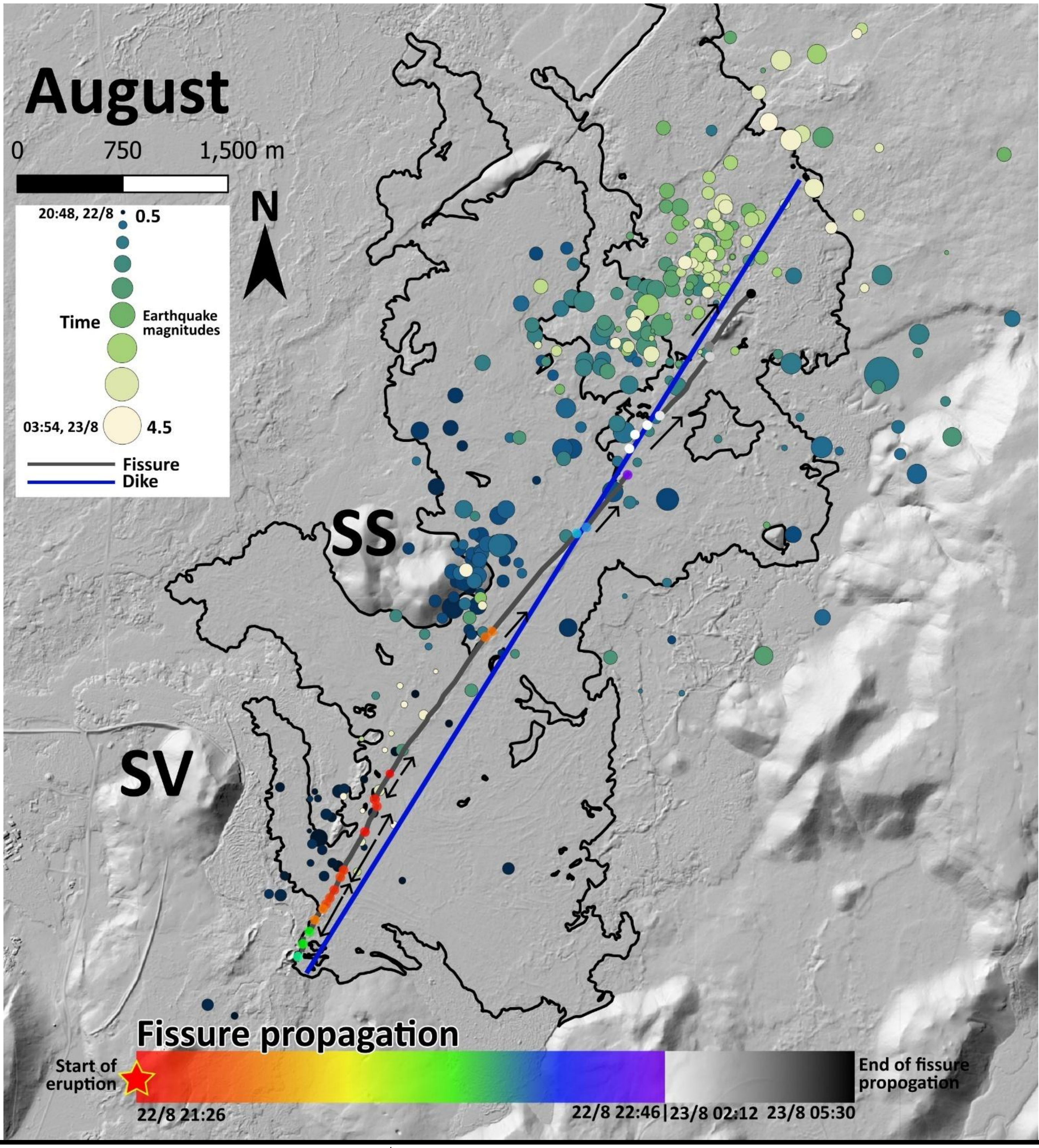

Fig.3.4f: *Seismicity from the injection of the August 22nd 2024 dike overlain by fissure propagation. Dot sizes are relative to earthquake size as per the key. Dike location: Parks et al., 2025; Seismicity: IMO, 2024b. Base map DEM from: ÍslandsDEM, 2025*

3.5 Fissure Locations

Dikes and their associated fissures propagate perpendicular to the direction of least compressive stress (σ3; Anderson, 1951), often exploiting preexisting structural weaknesses in the crust, even if not favourably orientated, if magma pressure exceeds σ3 (Delaney et al., 1986; Ziv and Rubin, 2000). Logically, fissures could be reused in subsequent eruptions as they represent areas of weakness that facilitate magma movement. However, when eruptions cease, fissures close, and magma solidifies in the void, potentially creating stronger material than the surrounding crust, depending on the degree of cooling. As a result, new fissures may be more likely to form adjacent to old ones, rather than reusing sealed pathways. If fissures have reopened along the Sundhnúkur crater row, it could indicate a persistent crustal weakness but shifts in fissure locations or orientations may suggest changes in crustal loading or stress distribution. Identifying faults that align with fissures could enhance predictions of future eruption sites.

Fissures from the December 2023 – September 2024 eruptions, mapped by the IMO, have been superimposed on a map of the Sundhnúkur crater row by Jenness and Clifton (2009, fig.3.5). This map provides a valuable opportunity to compare the 2350B.P. Sundhnúkur eruptions with ongoing activity in the region using geological evidence now overprinted by new lava flows. Jenness and Clifton (2009) propose several key hypotheses regarding fissure locations, which can now be tested. These include the existence of a continuous central fissure segment, repeated magma extrusion through Hagafell, the exploitation of N – S strike-slip faults and the deflection of fissures by surface topography.

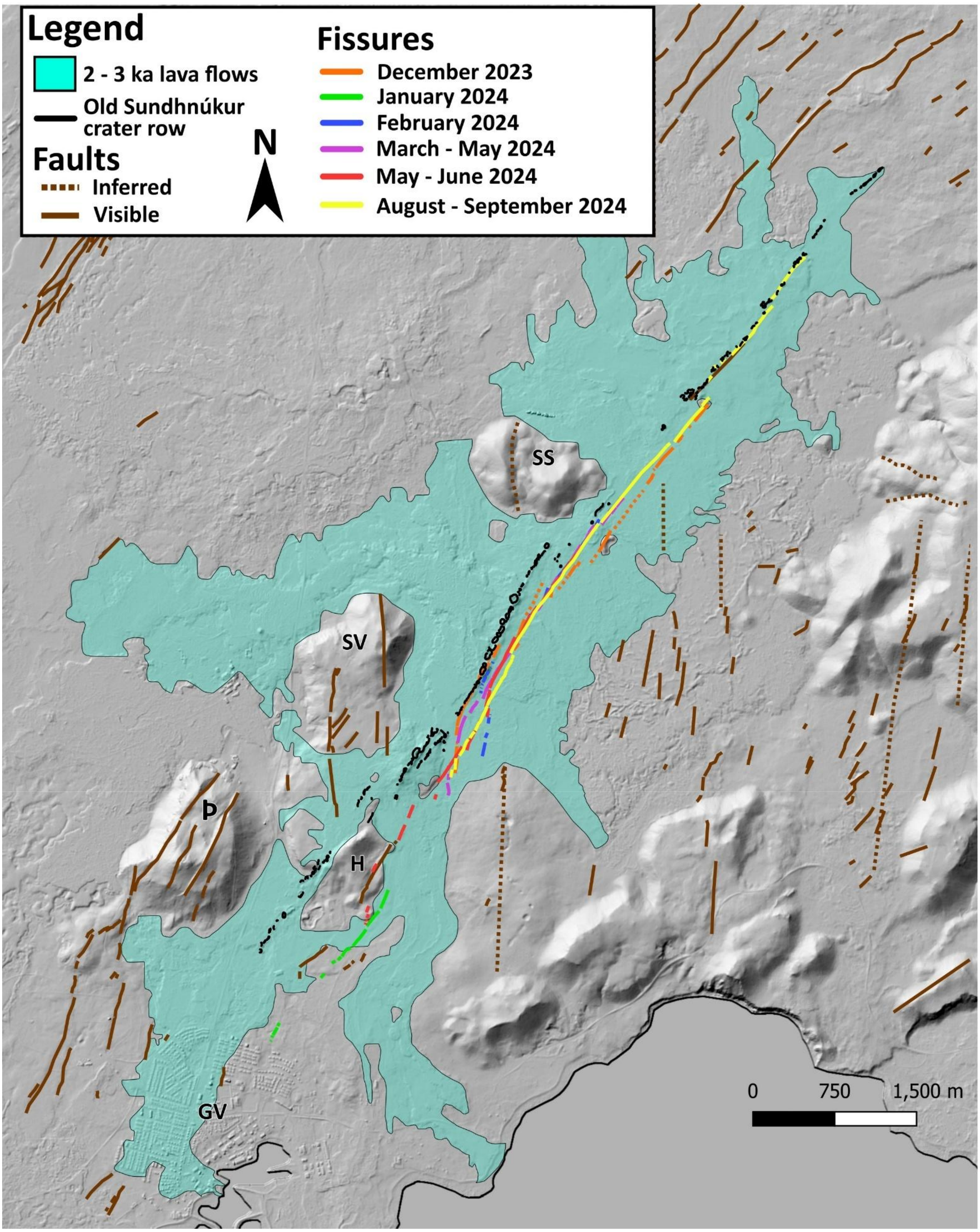

Fig.3.5: Map of the Svartsengi area, Iceland, showing fissure outlines from the December 2023 – September 2024 eruptions of the SVS, inferred and visible faults in the area and the outline of the old Sundhnúkur crater row. Also shown for reference is the outline of the lava erupted from the Sundhnúkur eruptions 2 – 3 ka. GV = Grindavík; Þ = Þorbjorn; H = Hagafell; SV = Svartsengisfell; SS = Stóra Skógafell. Faults, Sundhnúkur crater row outline and Sundhnúkur lava outline from Jenness and Clifton (2009). Base map DEM from: ÍslandsDEM, 2025

3.5.1 Continuous Central Segment

Jenness and Clifton (2009) identified a continuous fissure segment between Svartsengisfell and Stóra Skógafell (fig.3.6). Five of the six 2023 – 2024 SVS eruptions also produced fissures in this region. However, rather than a single continuous segment, this area is now characterised by numerous fissure segments from multiple eruptions, suggesting that the "continuous" central segment is actually a composite of fissures from multiple eruptions. This highlights a key oversight in the mapping of the Sundhnúkur crater row, as no account was made for the likelihood of crater row formation over multiple eruptions. Despite repeated fissure activity along this lineament, new fissures rarely open in the exact location of previous ones, indicating that fissures are not being reused in subsequent eruptions.

Overall, the pseudo-continuous fissure segment observed in the Sundhnúkur crater row has been replicated in the 2023 – 2024 eruptions. No other section of the lava field has been reactivated to the same extent suggesting either a distinct crustal weakness in this zone or that magma consistently flows into this area in greater volumes.

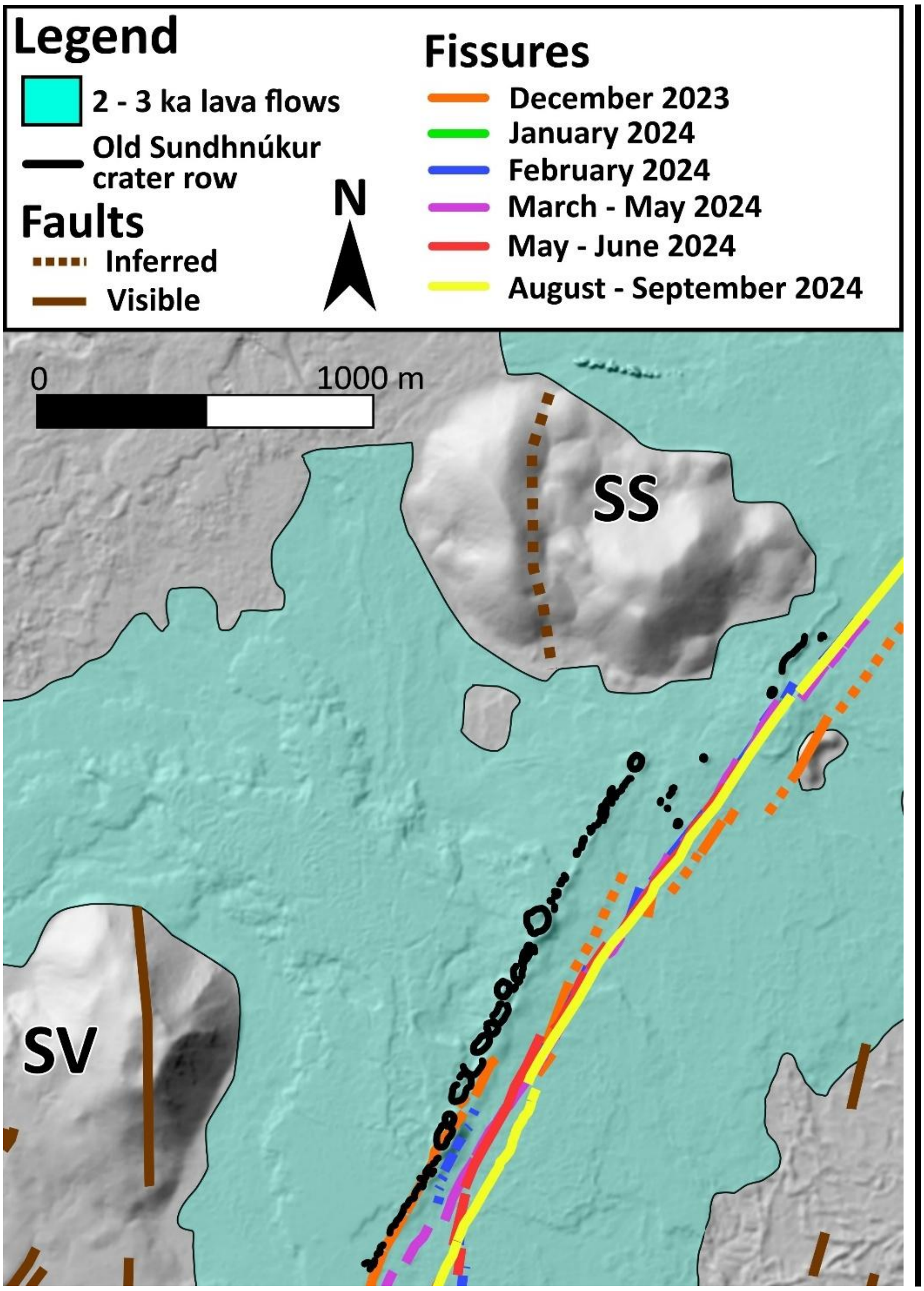

Fig.3.6: *Zoom in on the continuous segment of the Sundhnúkur crater row to the east of Svartsengisfell. SV = Svartsengisfell; SS = Stóra Skógafell. North up. Base map DEM from: ÍslandsDEM, 2025*

3.5.2 Hagafell Zone of Weakness

Hagafell is proposed to host a persistent zone of weakness, through which magma has risen several times (Jenness and Clifton, 2009). The Sundhnúkur craters travers the western flank of Hagafell, through conjugate fractures, and a May eruption fissure segment opened on the eastern flank through a normal fault (fig.3.7). This supports the hypothesis that magma repeatedly rises through Hagafell. However, fissure segments in the January eruption were deflected around Hagafell rather than propagating through it. Consequently, Hagafell may act as a topographic barrier to fissure propagation (see section 3.5.4) until sufficient crustal extension and weakening has occurred later into the rifting episode.

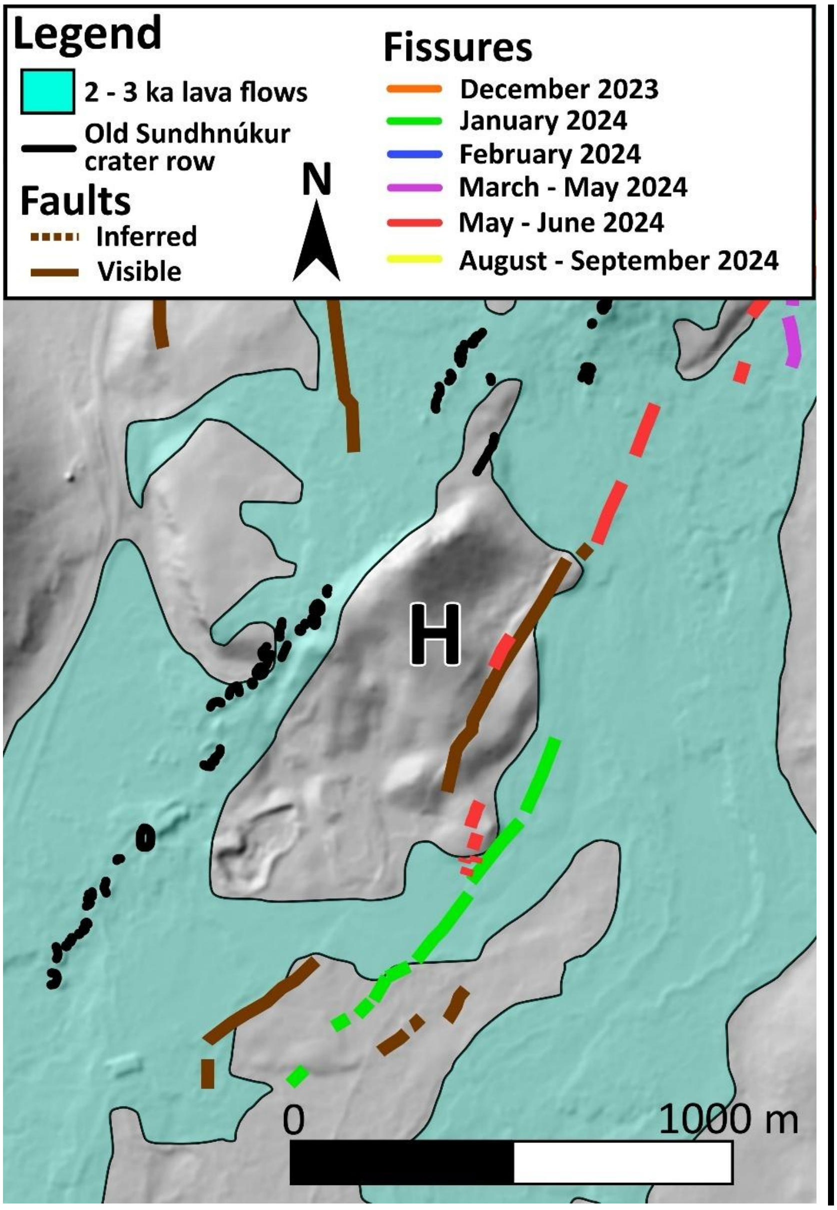

Fig.3.7: *Zoom in of Hagafell (H) showing Sundhnúkur craters on the western flank and a fissure from the May 2024 eruption exploiting the normal fault on the eastern flank. Also shown is the January fissure deflected round Hagafell. North up. Base map DEM from: ÍslandsDEM, 2025*

3.5.3 Exploitation of Strike-Slip Faults

Strike-slip faults in the region are orientated close to N – S (Sæmundsson et al., 2020), hence fissures exploiting them should also be close to N – S. Several fissure segments exhibit this orientation, notably those from the May eruption close to Hagafell (fig.3.7) and south of Svartsengisfell (fig.3.8). However, in both locations, topographic deflection (see section 3.5.4) could also explain the observed alignment.

Determining whether fissure orientation is controlled by faults or topography is challenging, as extensive lava flows likely prevented Jenness and Clifton from mapping all existing strike-slip faults. No fissure segment has opened directly along a mapped strike-slip fault, though fissure segments around Svartsengisfell are close to some (fig.5.4). However, in this area, orientations gradually shift from NNE – SSW to a N – S strike near the high topography, suggesting topographic deflection is a more probable cause. In contrast, the May fissure segments near Hagafell (fig.3.7) are consistently N – S in strike, making it more likely that they are exploiting strike-slip faults.

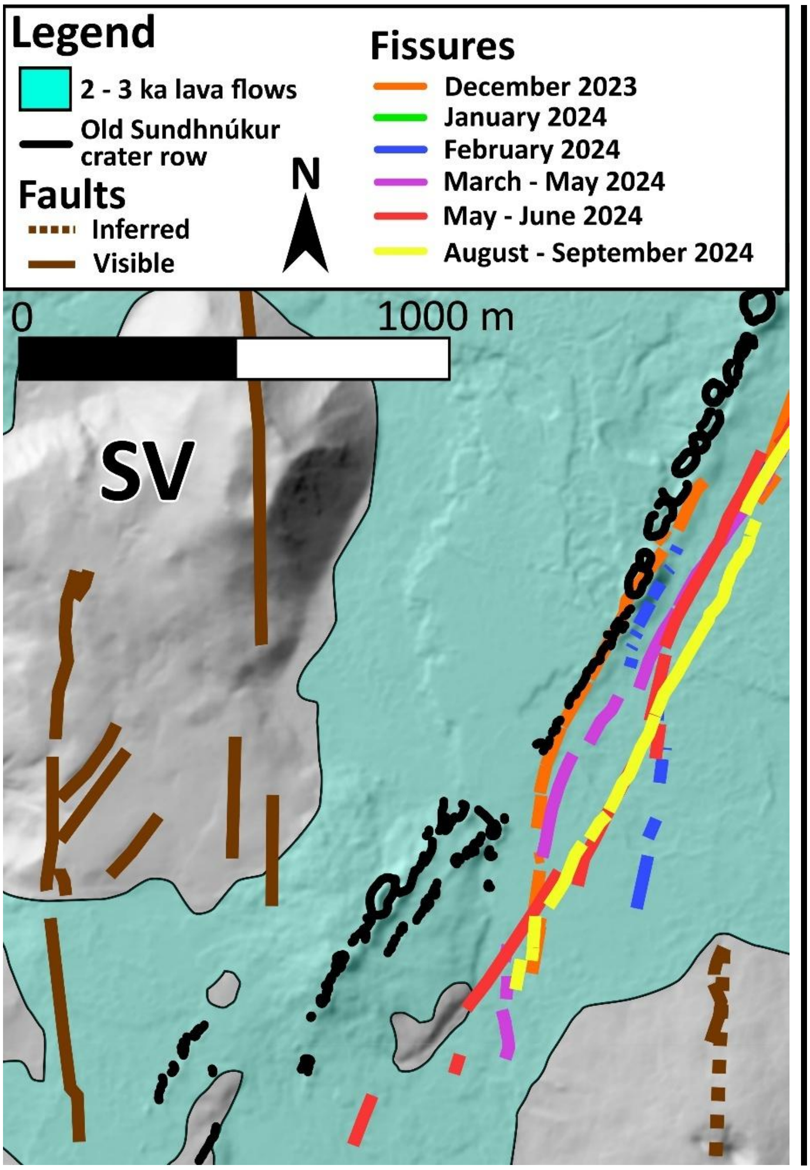

Fig.3.8: *Zoom in of the N – S orientated faults on the southern end of the continuous Sundhnúkur crater row. North up. Base map DEM from: ÍslandsDEM, 2025*

3.5.4 Deflection by Crustal Loading

Gravitational spreading of an edifice can modify the shallow crust's stress field, influencing dike propagation paths (Klügel et al., 2005). Even minor stress changes, as small as a few bars, can alter the direction of dike and fissure propagation (Walter and Amelung, 2006). This means that even the small topographic features in the lava field have the potential to influence fissure paths (Jenness and Clifton, 2009). While dikes typically erupt in low-elevation spaces unless a ridge parallel to the dike is present (Gaffney and Damjanac, 2006), this does not appear to be the case here, as fissures are deflected around the old crater row (fig.3.8). Fissures also curve around Hagafell (fig.3.7), providing field evidence supporting these predominantly experimental hypotheses. Similar dike deflections were also observed during the 2014 Barðarbunga eruption (Heimisson et al., 2015).

Between Svartsengisfell and Stóra Skógafell, new fissures do not align with the old crater row, but are displaced eastward (fig.3.6). However, the northernmost section of the August fissure directly overlaps the old crater row, demonstrating that fissures can still form along this features. This suggests that, while fissure paths are influenced by pre-existing weaknesses, the weight of extensive lava accumulation between Svartsengisfell and Stóra Skógafell during the 2350B.P. Sundhnúkur eruptions (Jenness and Clifton, 2009) has deflected most fissures eastwards (fig.3.6).

This evidence contrasts with Acocella et al. (2024), which proposes that even in extensional settings, magma tends to be drawn toward edifice summits rather than low lying areas.

3.5.5 Fissure Orientations

Fissure orientations (fig.3.9) vary both between and within eruptions due to the processes outlined above. The December and January eruptions exhibit greater variability in fissure orientation compared to later eruptions. This suggests that as continued extension occurs through successive eruptions, a more defined plane of weakness develops within the fissure field, allowing later fissures to propagate along a more optimal orientation. The March fissure was strongly influenced by topographic effects, which rotated its segments eastwards. Meanwhile, the August fissure aligns most closely with the ~40° mode, further supporting the idea that later eruptions propagate along a more defined structural trend.

The modal fissure bearing of the old Sundhnúkur crater row is 5° more northward than the new fissures (fig.3.10), because of topographic deflection of the new fissures from the old crater row. This demonstrates that lava accumulation from previous eruptions can influence the location and orientation of fissures in subsequent eruptive events.

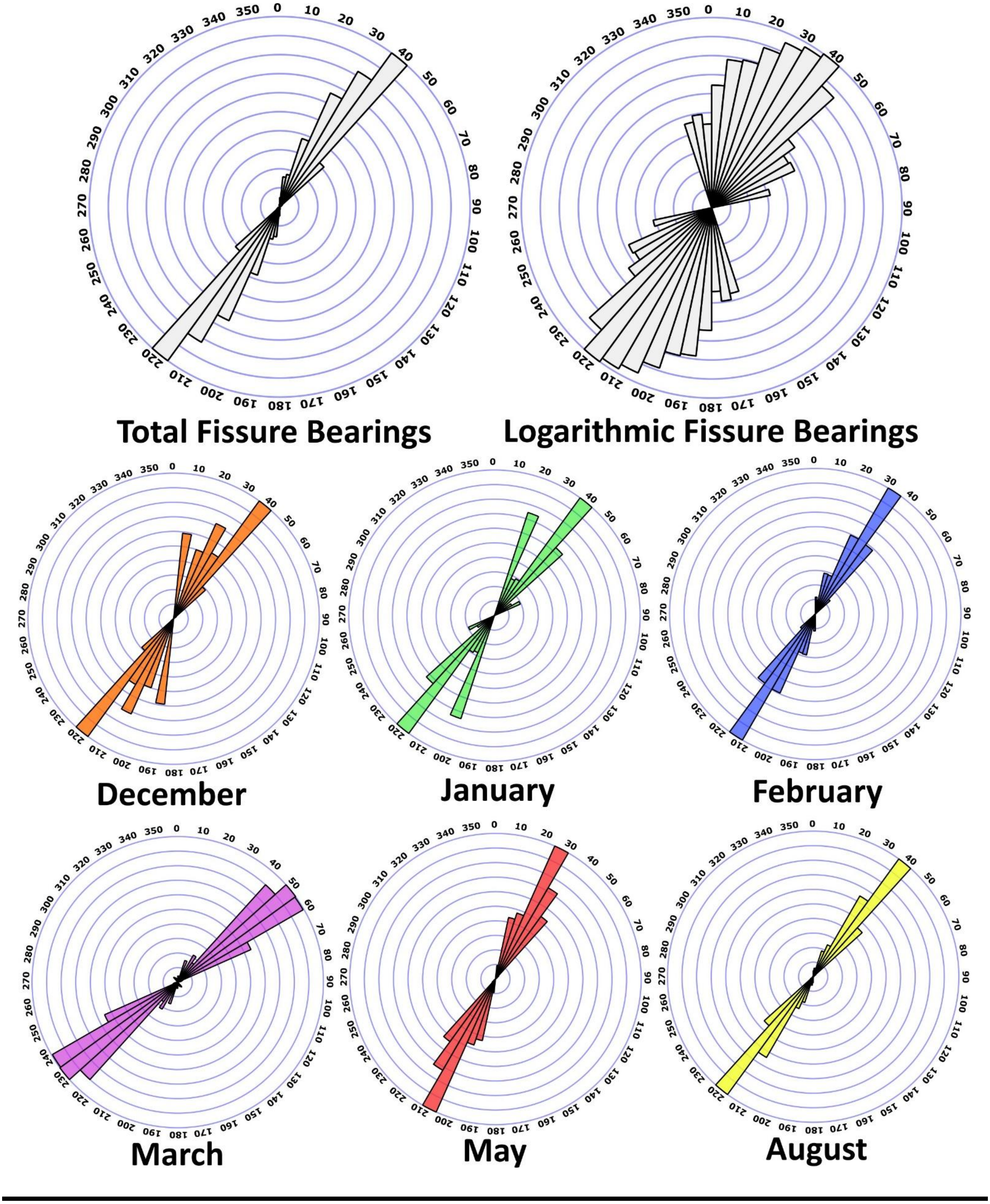

Fig.3.9: *Rose diagrams of the orientations of fissures during the 2023 – 2024 eruptions of the SVS. Segments are proportional in length to the lengths of fissures. Total fissure bearings are also shown on a logarithmic plot so the range of fissure orientations is clearer to see.*

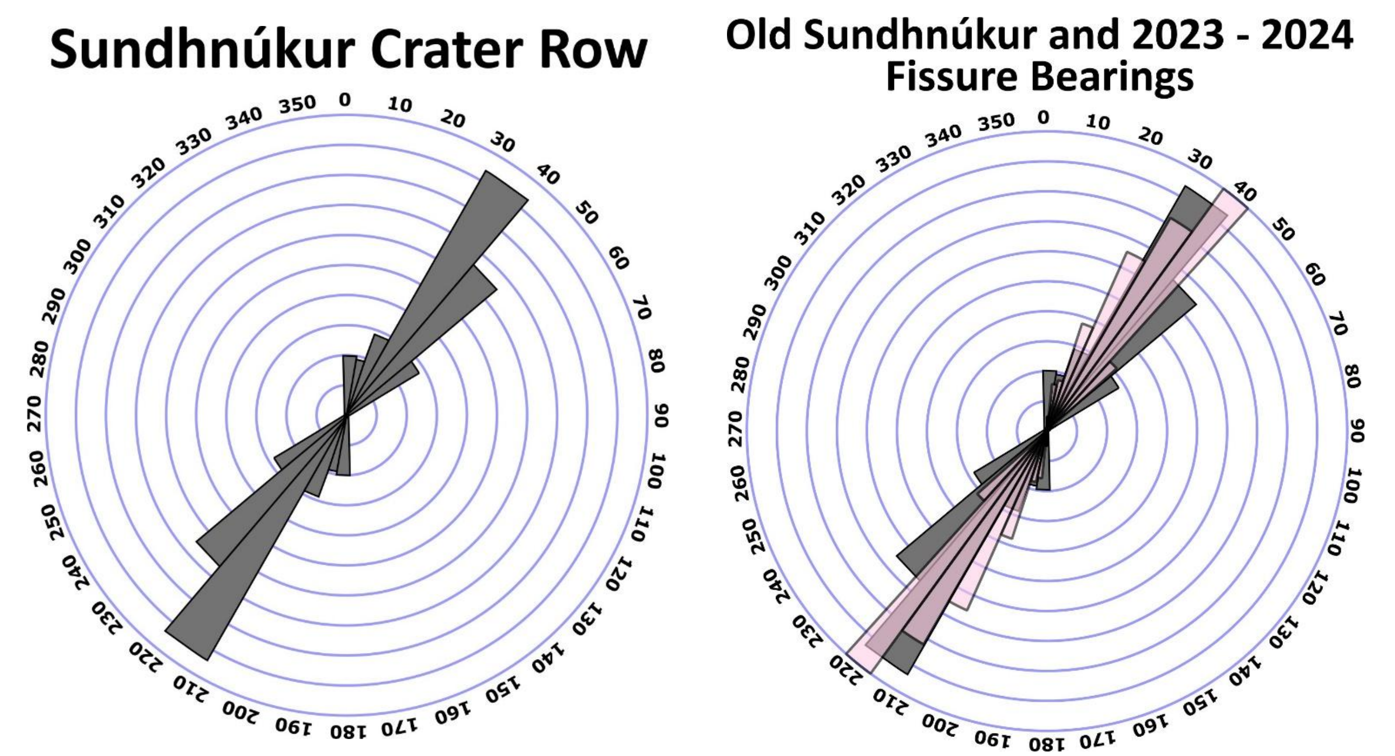

Fig.3.10: *Rose diagrams of the orientations of fissures of the old Sundhnúkur crater row (left) and the old Sundhnúkur crater row with the total new fissure orientations overlaid in pink (right). Segments are proportional in length to the lengths of fissures.*

3.5.6 Dike-Fissure Relationship

The locations of the precursor seismicity (IMO, 2024b), dike traces (Parks et al., 2025), and surface fissures differ from each other slightly (fig.3.11). Since seismic data has an approximate lateral error of +/- ~300 m it is unreliable for pinpointing exact dike locations. The dike traces have, therefore, been generated based on geodetic modelling of InSAR and GNSS data spanning each diking event, with the assumption that the dike is vertical and that the dike path is not segmented along its length (Parks et al., 2025). If the dikes are in fact slightly dipping, this could also result in an offset between the location of the dikes and the seismicity. The consistent bend in the fissures and disjointed seismicity east of Svartsengisfell suggests a possible bend in at least some of the dikes. But this depends on whether fissure deflection is influenced by topography and how deep this effect extends. If topography has no impact, the dike may be bent; if it affects only the shallow crust, bending is unlikely; but if its influence extends deeper, topography may have induced dike bending.

From the March eruption onwards, the dike seismicity spans roughly the same spatial extent as the surface fissure (fig.3.11). The first few fissures were unlikely to have been able to rupture the full extent of the dike at the surface because sufficient crustal weakening had yet to take place. Now that the crust has been weakened, the seismicity trace can be used as a proxy for the extent of the final fissure. However, as evident in the August eruption, seismicity is significantly less and weaker in locations that have continually been exploited by fissures, such as between Svartsengisfell and Stóra Skógafell. This suggests that future eruptions could come with less warning and less inclination of where the surface fissure could rupture.

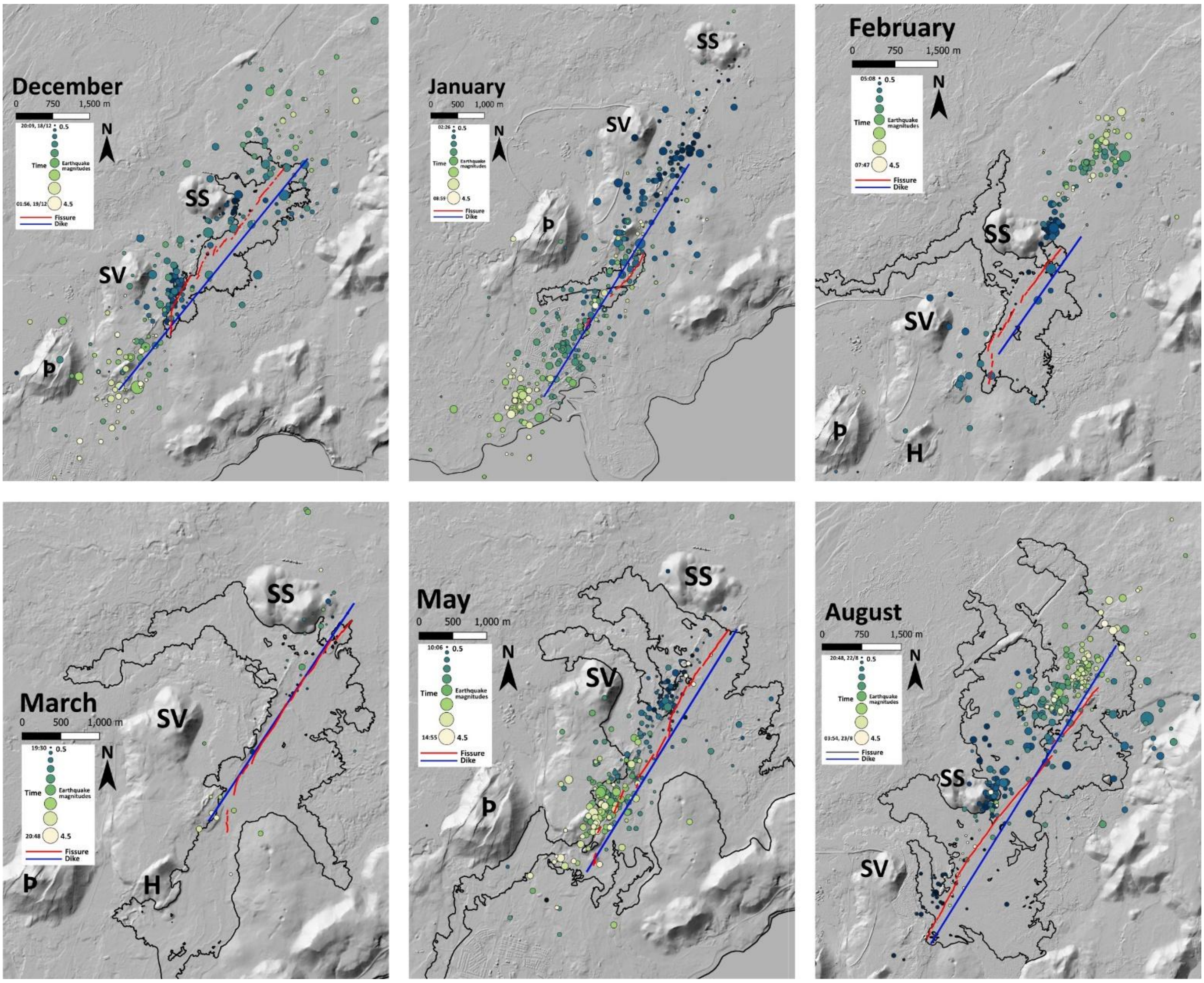

Fig.3.11: Dike seismicity, IMO dike trace, and surface fissure outline for the December 2023, January 2024, February 2024, March 2024, May 2024, and August 2024 eruptions of the Svartsengi volcanic system. For larger versions of these figures see Appendix B. GV = Grindavík; Þ = Þorbjorn; H = Hagafell; SV = Svartsengisfell; SS = Stóra Skógafell. Seismicity: IMO, 2024b; Dike trace: Parks et al., 2025. Base map DEMs from: ÍslandsDEM, 2025

A fire fountain is a mixture of magmatic gases and fragmented lava that erupts vertically from a vent because of the rapid release of volatiles from magma (Calvari et al., 2018). Few studies have focused on fire fountain dynamics from fissure fed eruptions, rather than from single vents, especially within the first few hours of an eruption before activity has concentrated into cones.

4.1 General Trends

In most fissure segments, the maximum fire fountain height is reached within ~10 minutes of a fissure segment opening, the height then decays, with some fluctuations, in a relatively linear form.

This pattern is most visible during the December eruption (fig.4.1). The fire fountain heights from each fissure segment have been normalised[c] in order to make comparison and pattern spotting clearer. The fire fountains from the December eruption lack major deviations from this common trend and any stochastic variability can be explained by the pulsatory nature of fire fountains.

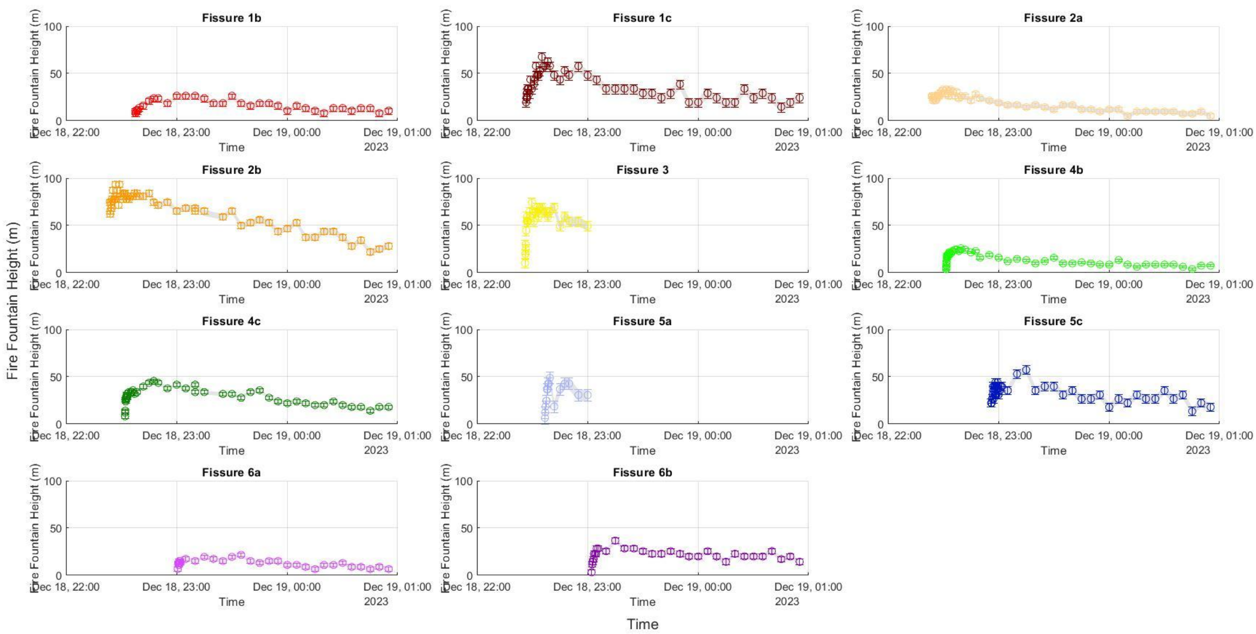

***Fig.4.1a:** Fire fountain heights for each measurable fissure segment during the first 2.5 hours of the December 2023 eruption*

[c] Fire fountain heights from each fissure segment have been stretched to have equal maximum and minimum heights, and shifted so all fissure segments open at the same time

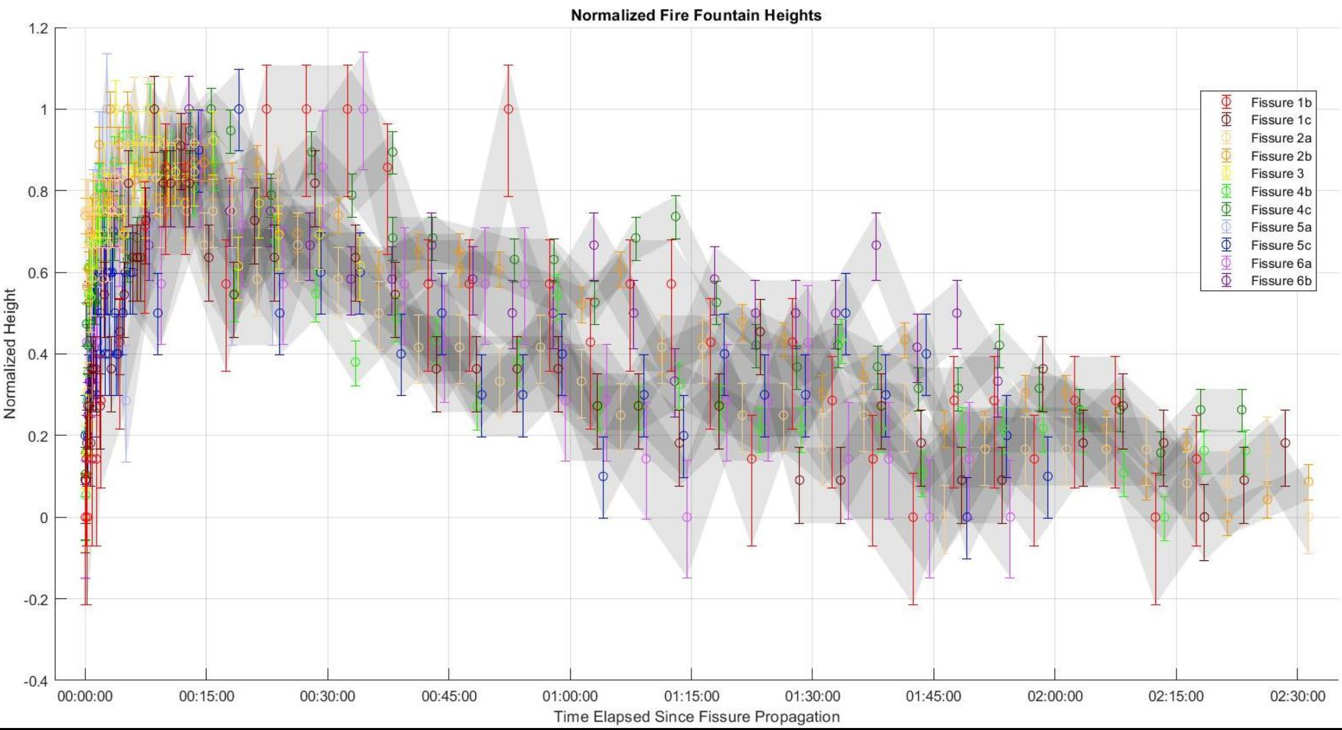

Fig.4.1b: *Normalised and shifted fire fountain heights during the first 2.5 hours of the December 2023 eruption.*

The March eruption follows this same pattern, albeit with a shallower decay gradient (fig.4.2). The uncertainties of the normalised fire fountain heights are larger than for the December eruption because footage has a reduced zoom and there are larger differences between fountain heights on each fissure segment, so the uncertainties increase during normalisation.

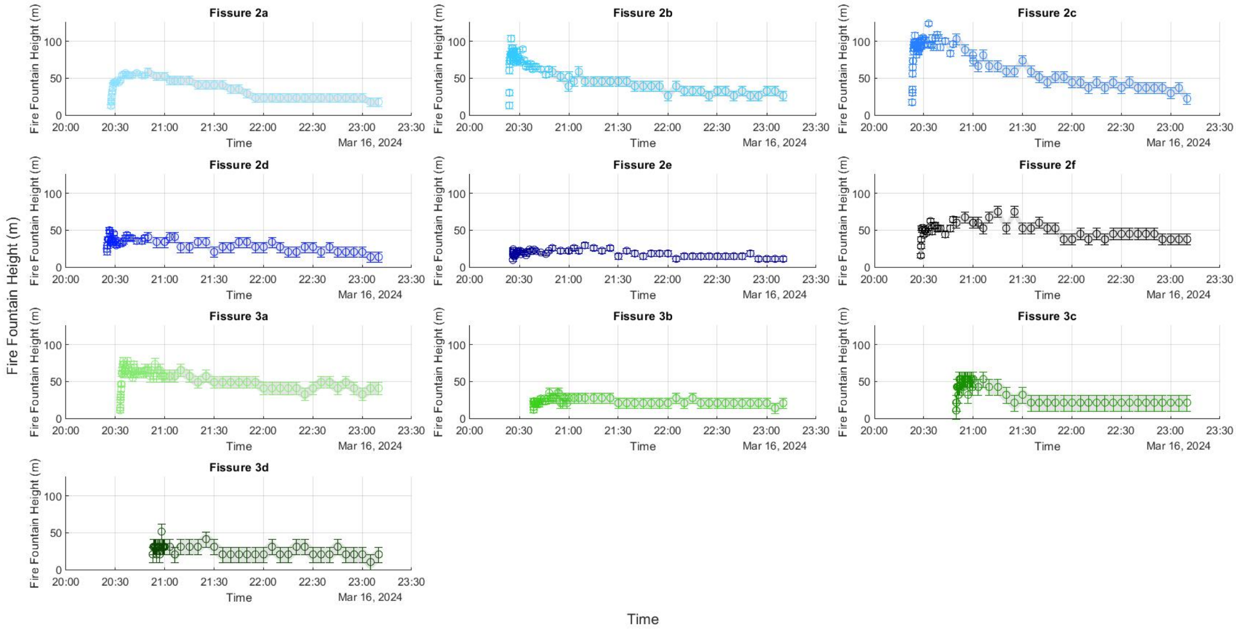

Fig.4.2a: *Fire fountain heights for each measurable fissure segment during the first ~ 3 hours of the March 2024 eruption*

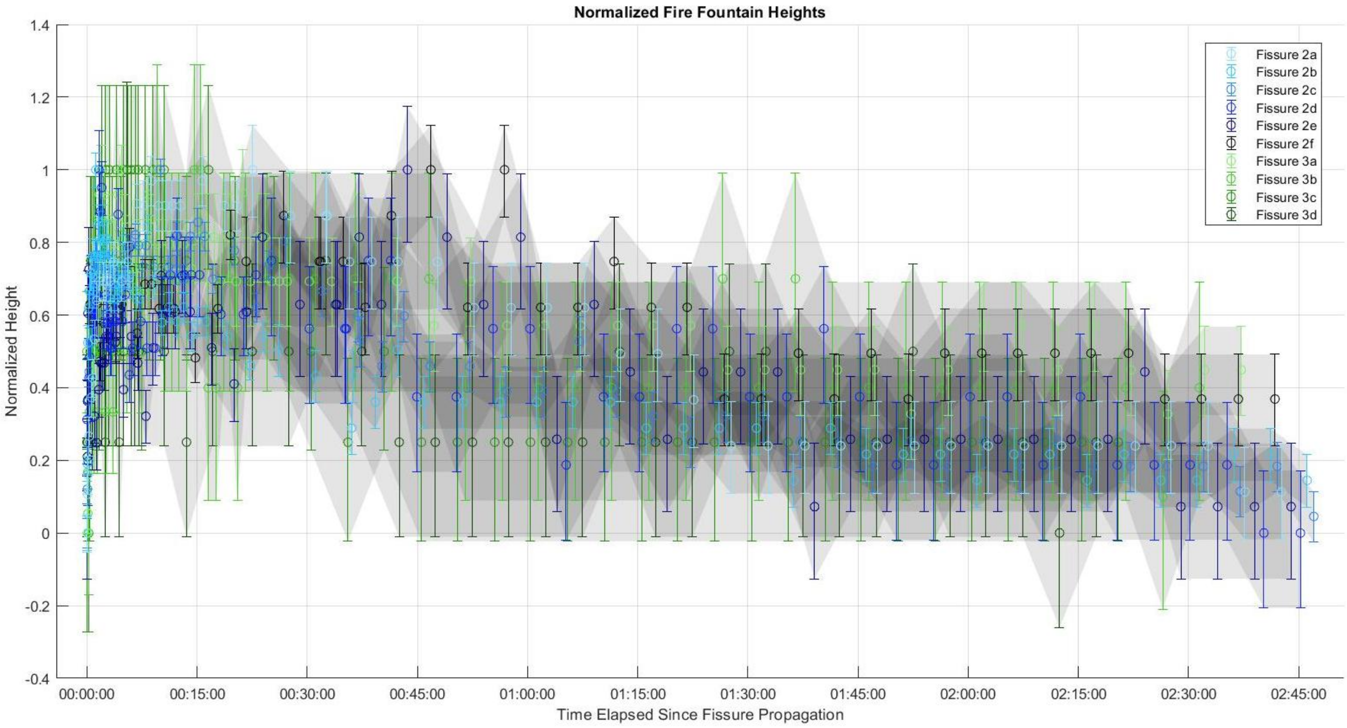

Fig.4.2b: *Normalised and shifted fire fountain heights during the first ~3 hours of the March 2024 eruption.*

The fire fountain heights during the January eruption are more variable than during the other eruptions (fig.4.3). Fissure opening during the January eruption occurred in two distinct phases. The first phase of opening occurred close to Þorjörn at ~08:00. The second phase of opening occurred at ~12:00 in Grindavík. The second phase had much shorter fissure segments with smaller fire fountains than the first phase, and due to their spatial and temporal separation, these phases have generally been analysed separately throughout. During the first phase, some fissure segments show a pulse of increased vigour at ~09:30, along with reduced vigour at ~09:00 and ~10:00. These pulses are most obvious in fissures 1b, 1c and 2a (fig.4.4) which had higher overall fountains than other fissures. These pulses in activity suggest that simple linear decay of fire fountain heights over time is not always the case, and that other factors, such as pressurisation of the magma system, could be contributing to fire fountain dynamics.

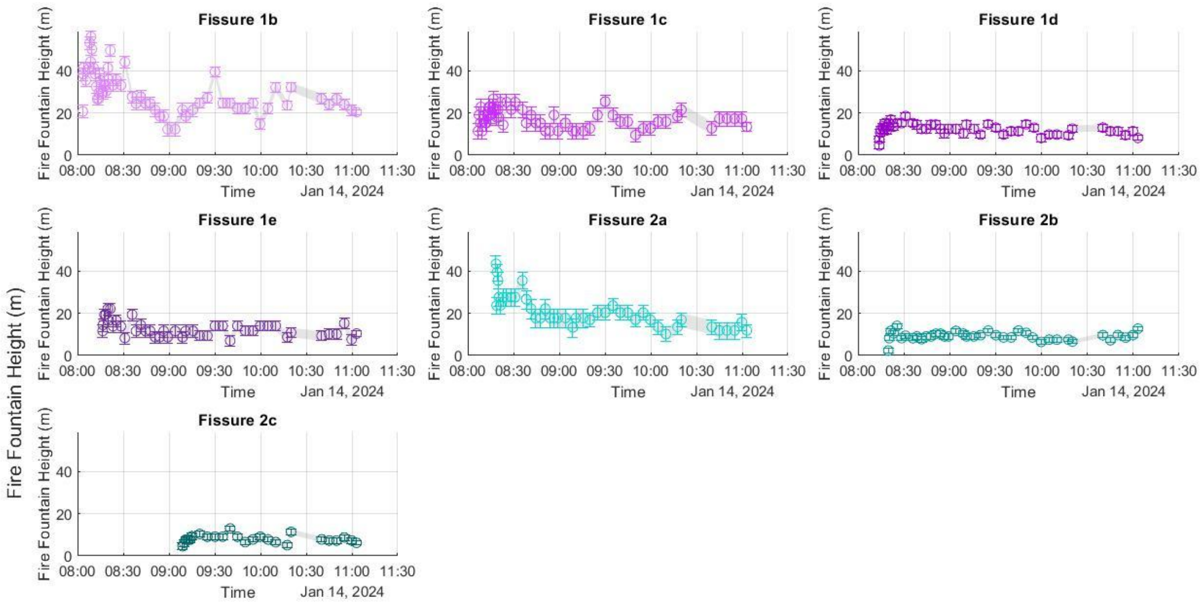

Fig.4.3a: *Fire fountain heights for fissure segments 1 and 2 during the first ~3 hours of the January 2024 eruption*

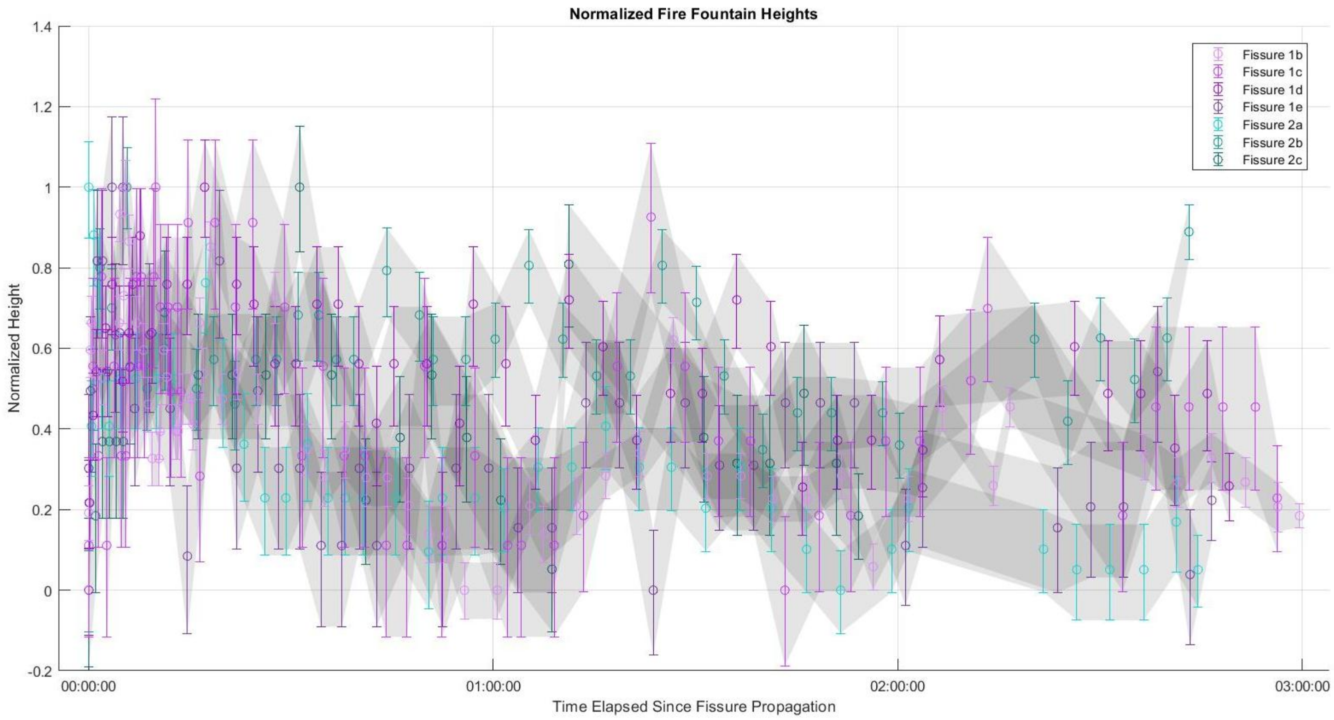

Fig.4.3b: *Normalised and shifted fire fountain heights during the first 3 hours of the January 2024 eruption.*

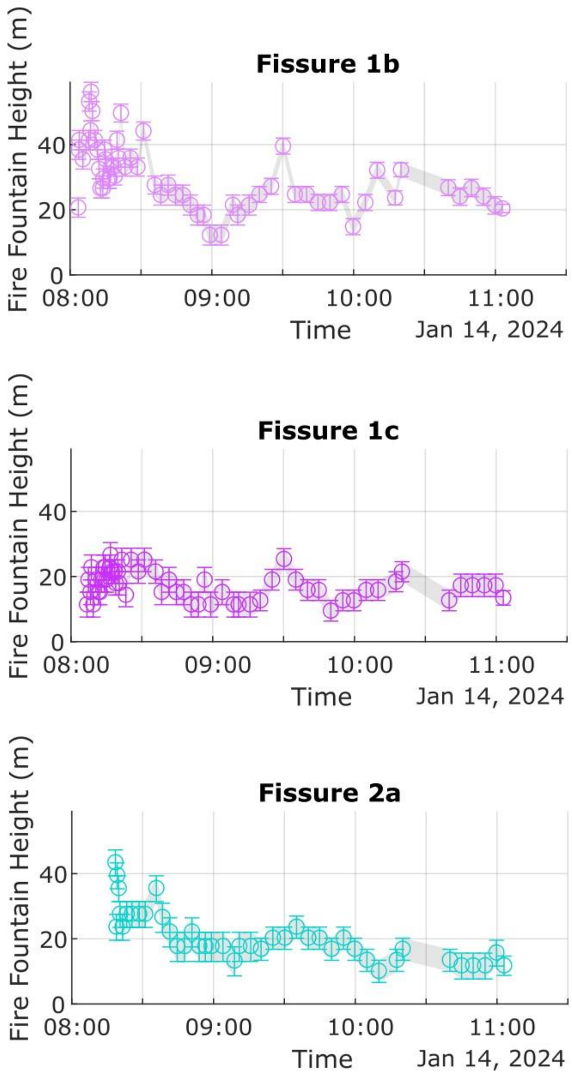

Fig.4.4: *Fire fountain heights through time for fissure 1b, 1c and 2a from the January 2024 eruption.*

The fire fountains during the August eruption have significantly different characteristics compared to the other eruptions (fig.4.5). Fissures 3b, 4a and 4b show the same pattern as the other eruptions, but the fire fountains for fissure 3c do not show any significant decrease in height and continue to increase in height through time. Each of the other fissure segments have fountain heights that eventually plateau at ~50m, while fountains from 3c reach >400m. Because the increase in height on fissure 3c is most likely driven by conduit erosion (see section 4.3), a process not extensively occurring in the other fissure segments, the August eruption heights have generally been left out of statistical analysis, unless deemed relevant, to prevent confusion. Measuring was cut short during the August eruption because of poor camera angles.

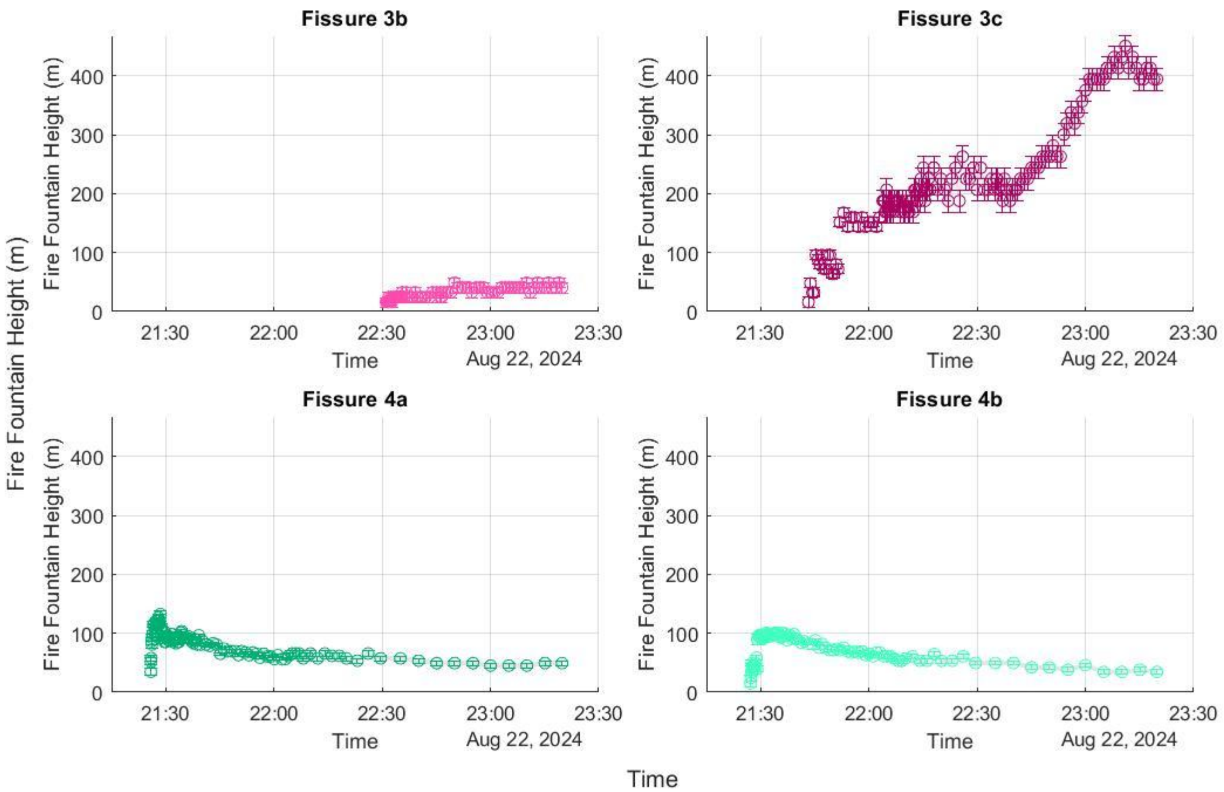

Fig.4.5a: *Fire fountain heights for fissure segments 3 and 4 during the first ~2 hours of the August 2024 eruption.*

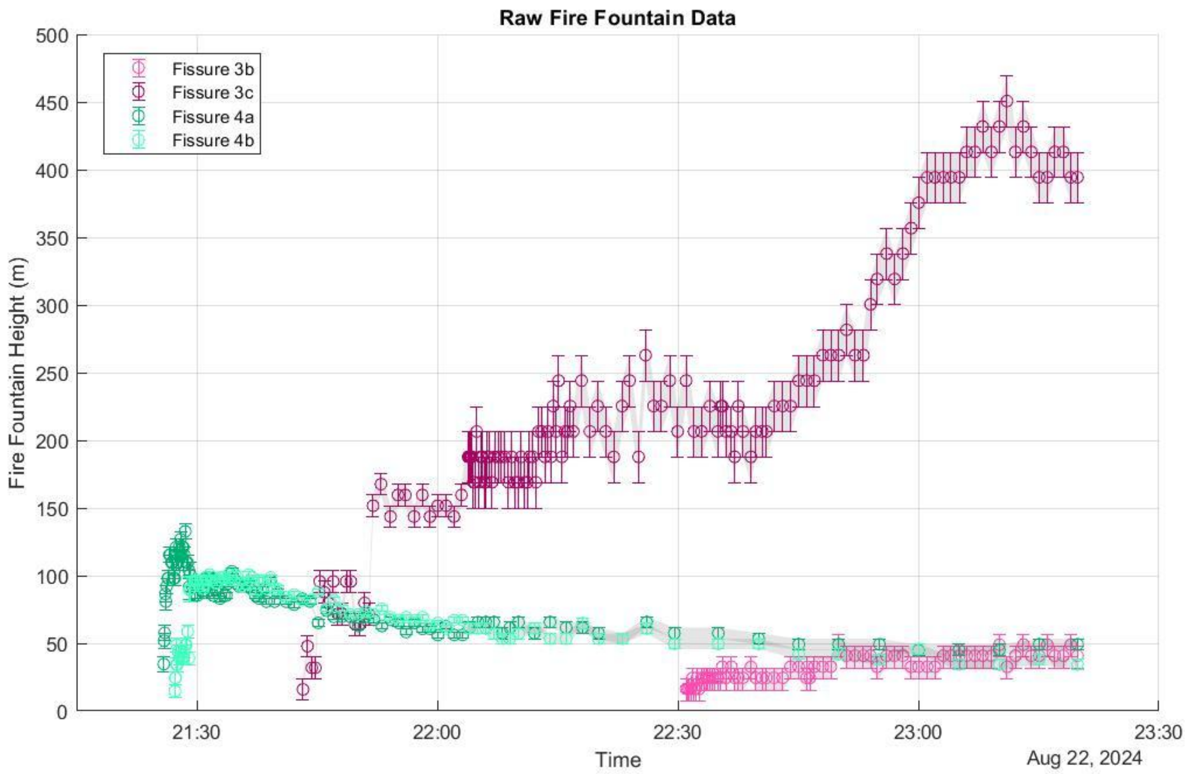

Fig.4.5b: *Fire fountain heights for fissure segments 3 and 4 during the first ~2 hours of the August 2024 eruption, plotted on one set of axes.*

4.2 Proposed Drivers of Fire Fountain Height

High fire fountains are proposed to come from systems with high magma gas content, high mass eruption rate and low magma viscosity, with increases in mass eruption rate being controlled by increased conduit size, greater magma density differences and pressurisation of the magma source (Wilson and Head, 1981). The factor with the greatest influence on fire fountain height is thought to be exsolved volatile content (Head and Wilson, 1987; Moyer and Sahagian, 2024), however, studies have focused on eruptions from single vent systems rather than from fissures (Wolfe et al., 1987). Even studies that look at fire fountains from fissure fed eruptions focus on looking at the fire fountains after the fissures have concentrated into cones (Witt et al., 2018). Within a single fissure fed eruption, the heights of fire fountains can vary between different fissure segments despite being fed by a single magma reservoir (Sigmundsson et al., 2024; fig.4.5). Therefore, it seems unlikely that magma gas content or viscosity is varying significantly between fissure segments, suggesting variations could be caused by mass eruption rate, which itself is controlled by fissure geometry and magma system pressure. Although, it is possible that variations in volatiles could be changing fire fountain heights between eruptions. Furthermore, dike overpressure has been predicted to control explosivity during fissure fed eruptions (Geshi et al., 2020), suggesting it may be possible to predict the expected fire fountain heights from characteristics of the dike.

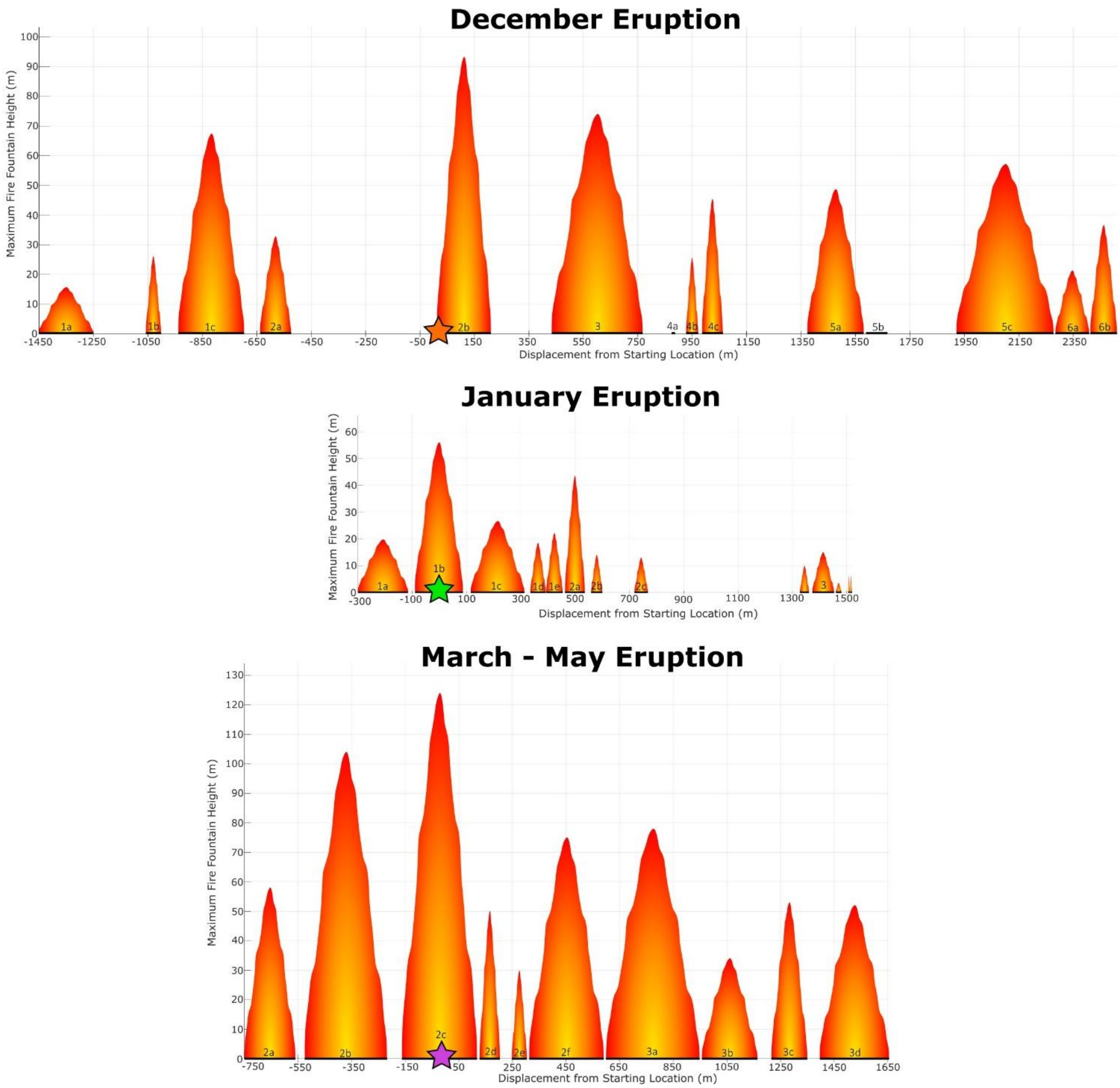

Figure caption overleaf...

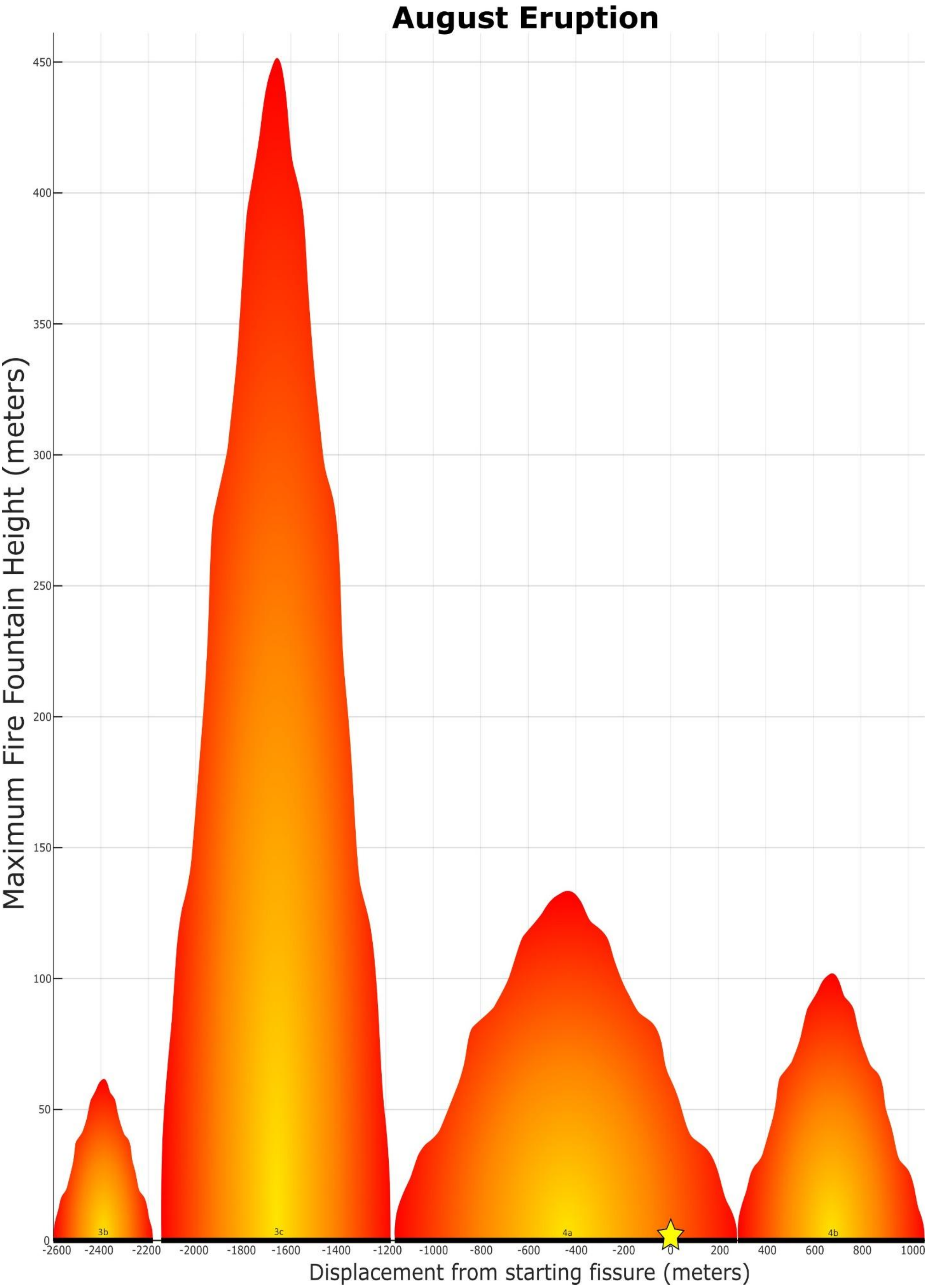

Fig.4.5: *Maximum fire fountain heights on each fissure during the December 2023, January 2024, March 2024 and August 2024 eruptions. Start location of each eruption is indicated with a star, and the fissures are plotted with their location relative to the start. Fissures outside those shown had fire fountains that could not be measured. Fissures shown with no fire fountain indicates a fissure that had fire fountains that could not be measured. Scale on each plot is the same to allow for comparison in height between eruptions. Vertical scale is exaggerated relative to horizontal scale. Fire fountain heights are schematic. Left is north, right is south*

4.3 The Influence of Fissure Length and Conduit Geometry

The January and March eruptions show strong positive correlations between fissure length and fire fountain height (table.4.1, fig.4.6), as larger conduits lead to increased mass eruption rates (Wilson and Head, 1981). However, during the December eruption, this correlation is negligible. Fire fountains during the December eruption also show weak correlations with other proposed controlling factors (see Appendix C) suggesting that the first eruption in a reactivated system may be more unpredictable. The exceptionally strong correlation in March suggests that predictability improves with successive eruptions.

There is negligible correlation between fire fountain height and fissure length during the August eruption (table.4.1). However, fissure length has been used as a proxy for conduit geometry, with fissure width being neglected. While this approximation has been valid thus far, it does not stand during the August eruption. When looking at the heights of fire fountains through time during the August eruption (fig.4.5) it is possible to see that the heights on segment 3c increase through time while the heights from the other segments decay linearly as expected. Because this increase in height is not matched in all figure segments, it cannot be explained by magma system processes. Therefore, the most likely explanation is that fissure segment 3c has experienced extensive conduit erosion at the start of the eruption, leading to an increase in mass eruption rate (Burgisser et al., 2015; Sahagian, 2005; Piombo et al., 2016). The widening of a fissure segment through erosion allows more magma to extrude from a segment at any one time, leading to a higher mass flux than is predicted based on the dike or fissure shape (Mitchell, 2005). Higher mass eruption rate then leads to higher fire fountains (Wilson and Head, 1981). Therefore, despite the lack of correlation between fissure length and fire fountain heights, when fissure width is considered, August still fits this correlation.

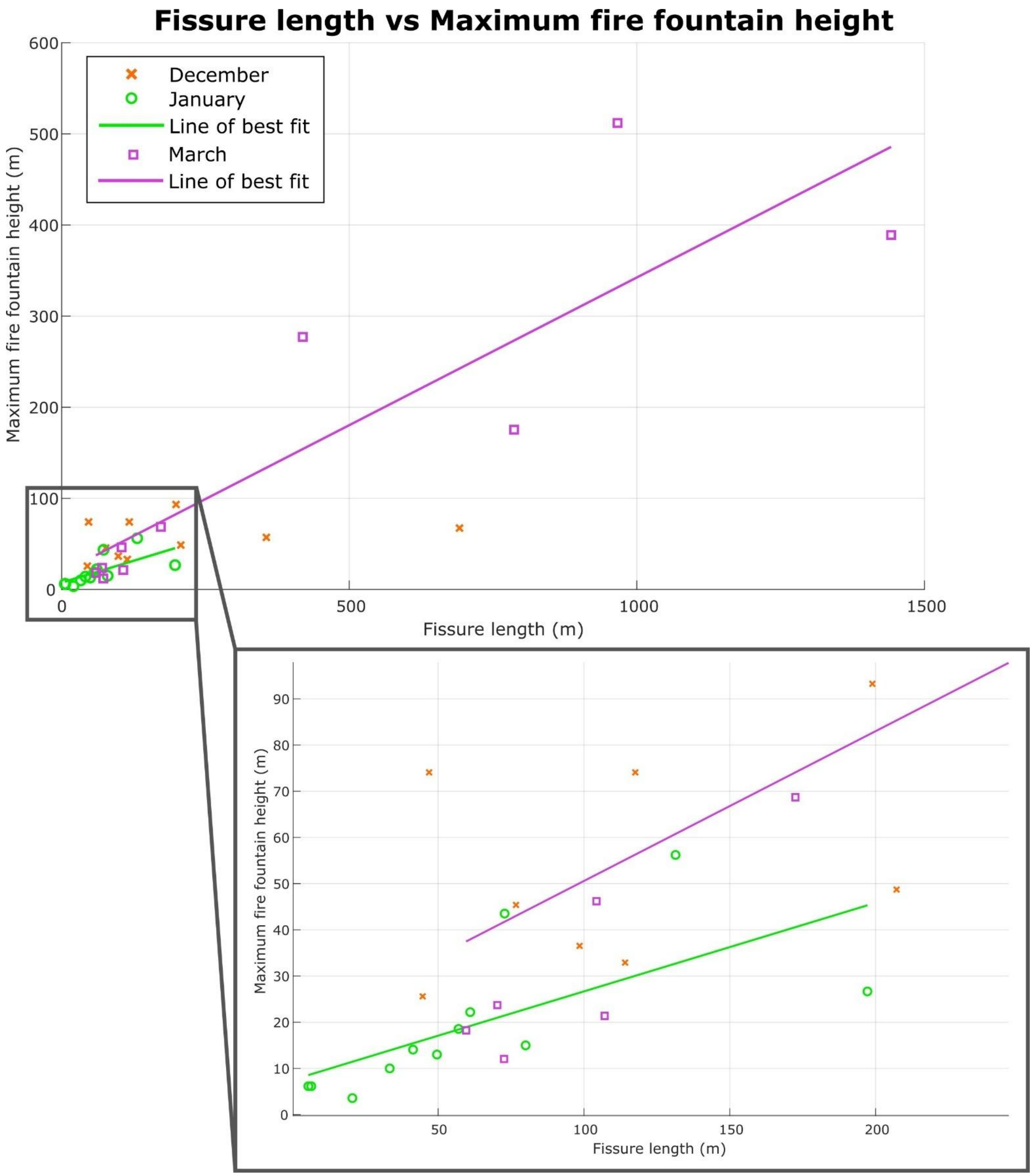

Fig.4.6: *Correlation plot between fissure lengths and fire fountain heights. Excluding the August eruption for clarity. Only best fit lines for correlations of moderate strength or greater have been shown. Best fit lines have been calculated using a least squares regression method, using the polyfit and polyval functions on MATLAB.*

	Month	Pearson's R value	Correlation strength	Significant?
Maximum fire fountain height vs fissure length	*December*	0.2965	Negligible	No
	January	0.6604	Moderate	Yes
	March	0.8730	Strong	Yes
	Total mean (excluding August)	0.8557	Strong	Yes
	August	0.2570	Negligible	no

Table.4.1: *Pearson's R value of the correlation between maximum fire fountain heights measured during each eruption and the length of the fissure they came from. |R| < 0.3 negligible; |R| < 0.5 weak; |R| < 0.7 moderate; |R| < 0.9 strong; |R| > 0.9 very strong. Significant if p < 0.05*

4.4 The Influence of Distance and Time from the Start of Eruption

Excluding during the August eruption, where extenuating circumstances are at play, the maximum fire fountain height measured during an eruption always comes from the fissure that was first to open (fig.4.5). Pressure in the magma chamber drops during dike and fissure propagation (Einarsson, 1991), so fire fountains furthest away from the start of fissure propagation should be smaller. However, there is only strong, negative correlation during the January eruption, with the March eruption exhibiting the weakest correlation (table.4.2; fig.4.7; fig.4.8). This suggests that fissure length plays a more significant role during the March eruption. Although a significant correlation exists for the January eruption, it does not indicate causation because the March eruption is insignificant. Rather, this correlation reflects the length-height relationship as later and further away fissures to propagate were smaller. Like the length-height relationship, the December eruption shows a weak-to-moderate, insignificant correlation, reinforcing the idea that a system's first eruption is unpredictable.

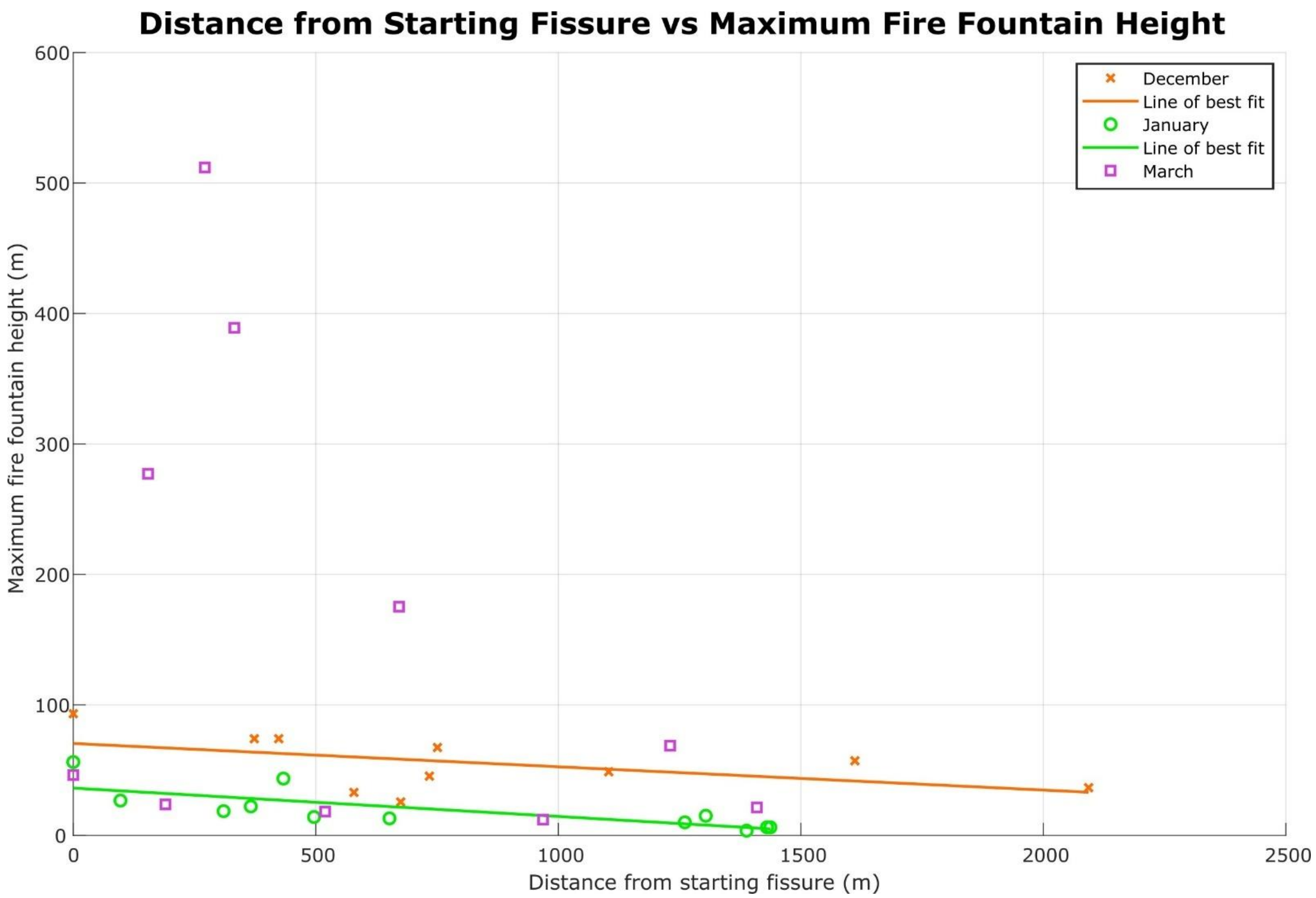

Fig.4.7: *Correlation plot between distance of fissure from the starting fissure to propagate during an eruption and fire fountain heights. Only best fit lines for correlations of moderate strength or greater have been shown. Best fit lines have been calculated using a least squares regression method, using the polyfit and polyval functions on MATLAB.*

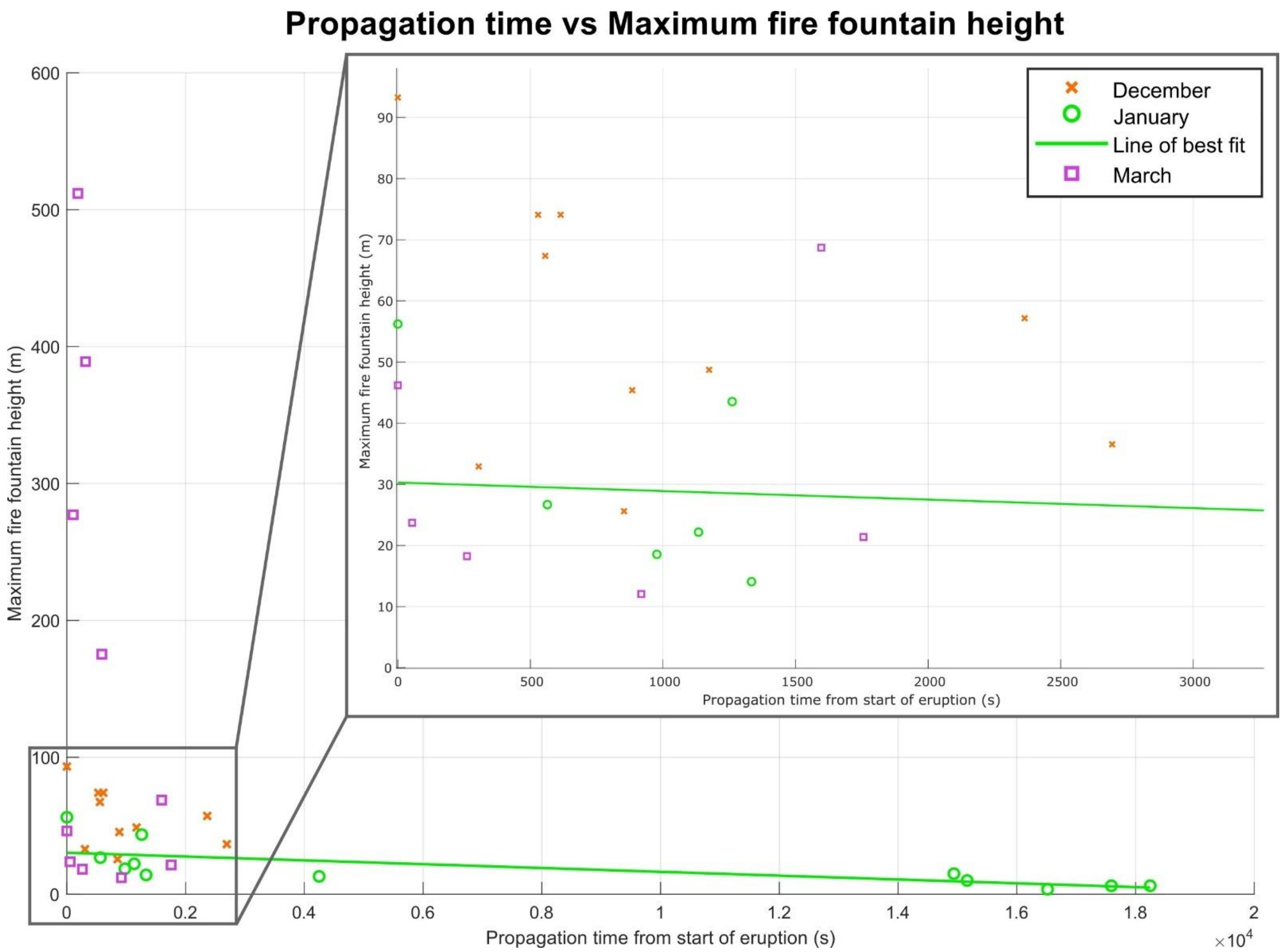

Fig.4.8: *Correlation plot between fissure propagation time from the start of eruption and fire fountain heights. Only best fit lines for correlations of moderate strength or greater have been shown. Best fit lines have been calculated using a least squares regression method, using the polyfit and polyval functions on MATLAB.*

	Month	**Pearson's R value**	**Correlation strength**	**Significant?**
Distance from starting fissure vs maximum fire fountain height	*December*	0.5134	Moderate	No
	January	0.7624	Strong	Yes
	March	0.4073	Weak	No
Time from start of eruption vs maximum fire fountain height	*December*	0.4067	Weak	No
	January	0.7206	Strong	Yes
	March	0.3645	Weak	No

Table.4.2: *Pearson's R value of the correlation between maximum fire fountain heights measured during each eruption and the distance and time from the start of the eruption that their fissure propagated. |R| < 0.3 negligible; |R| < 0.5 weak; |R| < 0.7 moderate; |R| < 0.9 strong; |R| > 0.9 very strong. Significant if p < 0.05*

4.5 The Influence of Overpressure and Vesicularity

Geshi et al., (2020) link fissure eruption explosivity to feeder dike overpressure and exsolved volatile concentration. Magma overpressure widens the dike, increasing vesicular lava flux. In the SVS, explosivity is reflected in fire fountain height, suggesting a potential link between dike overpressure and fountain height. Geshi et al., (2020) provide equations to calculate dike overpressure and vesicularity (box.4.1), which, combined with Moyer and Sahagian's (2024; box.4.2) equations using bubble number density, allow fire fountain heights to be predicted. These calculations suggest magma overpressure was higher during the January eruption than in December, despite lower fire fountains, indicating additional factors influence fountain height (fig.4.9).

Over pressure (Geshi et al., 2020)	***Excess magmatic pressure (Geshi et al., 2020)***	***Vesicularity (Geshi et al., 2020)***
$P_o = \frac{w\rho_r V_s^2}{L(1-v)}$	$P_e = P_o - (\rho_r - \rho_m)gh$	$p = \frac{P_o - P_e}{\rho_r gh}$

Where:
w = maximum dike opening in meters (provided by IMO)
L = dike length in meters (provided by IMO)
h = depth of magma reservoir ($5000m$: Sigmundsson et al., 2024)
ρ_r = density of the host rock in kgm^{-3} ($3275\ kgm^{-3}$: Bagdassarov, 2021)
ρ_m = density of the magma in kgm^{-3} ($2710\ kgm^{-3}$ starting point: Hartley and Maclennan, 2018)
V_s = s-wave velocity through the crust at the depth of the dike in m/s ($3030\ ms^{-1}$: Vinciguerra et al., 2005)
v = Poisson ratio (0.25: Geshi et al., 2020)
g = 9.81 ms^{-2}

Box 4.1: *Equations for overpressure, excess magmatic pressure and vesicularity from Geshi et al., (2020)*

Fire fountain height (Moyer and Sahagian, 2024)

$H_{max} = 0.07n + 90$

Where:
n = bubble density $= \frac{p}{bubble\ volume}$, assuming bubble volume^d $= 0.001$

Box 4.2: *Equations for fire fountain height from Moyer and Sahagian (2024)*

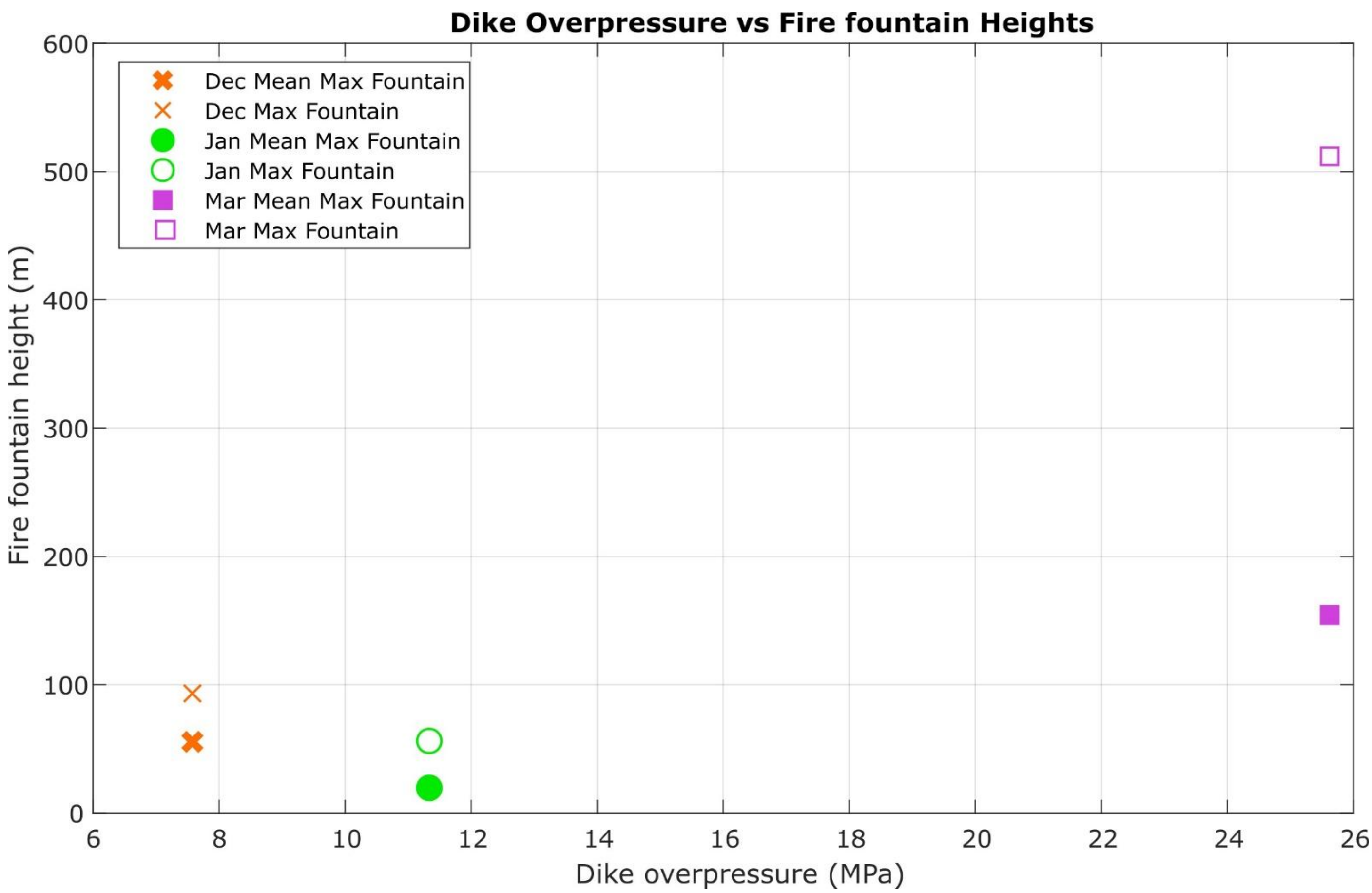

Fig.4.9: *Estimated overpressure (after Geshi et al., 2020) and the measured overall maximum, and average maximum fire fountain heights from each fissure during the December 2023, January 2024, and March 2024 eruptions of the SVS.*

Vesicularity can be calculated using the density difference between the host rock and the magma (Geshi et al., 2020). Since the magma density for these eruptions is unknown, it has been varied in calculations to determine whether reasonable values could recreate observed fire fountain heights. Assuming a crustal density of 3275kg/m^3 (Bagdassarov, 2021), and an estimated mean bubble volume of 0.0015mm^3 [d], matching the measured fire fountain heights requires magma densities of 3000 kg/m^3 in December, 5800 kg/m^3 in January, and an impossibly low value in March using Moyer and Sahagian's (2024) equation. These extreme[e] and inconsistent densities suggest that dike overpressure and magma vesicularity alone do not adequately explain fire fountain heights in these eruptions.

[d] A bubble volume of 0.0015mm^3 has been used from averaging the diameters of 24 bubbles from a tephra sample taken on the 17th March 2024

[e] These exact values are unlikely to be accurate due to assumptions of the bubble number density, crustal density, s-wave velocity, and the depth of the magma reservoir, but because these same assumptions have been made in each eruption, the magnitude of variations in required magma density between eruptions can still be used to support the principal.

4.6 Other Potentially Significant Controlling Factors

Long-term fissure propagation speed reflects the magma system's stress state (see Section 3). Comparing fissure propagation speed and fire fountain heights provides another way to assess magma overpressure's influence. However, the correlation between fissure propagation speed and fire fountain height is not strong (table.4.3). The strongest correlation occurs during the March eruption, yet significant deviation from the line of best fit remains (fig.4.10). This further supports the findings in Section 4.5 that overpressure is not a major control on fire fountain heights.

Other potential controlling factors include total erupted volume, inflation duration, eruption duration, and inflation volume. Longer and more voluminous eruptions should logically produce higher fire fountains, and a strong correlation between fire fountain height and eruption duration could enable early predictions of eruption duration. However, none of these correlations are strong (table.4.3), likely a product of small sample size. As more data is collected from future eruptions, the reliability of these findings will improve.

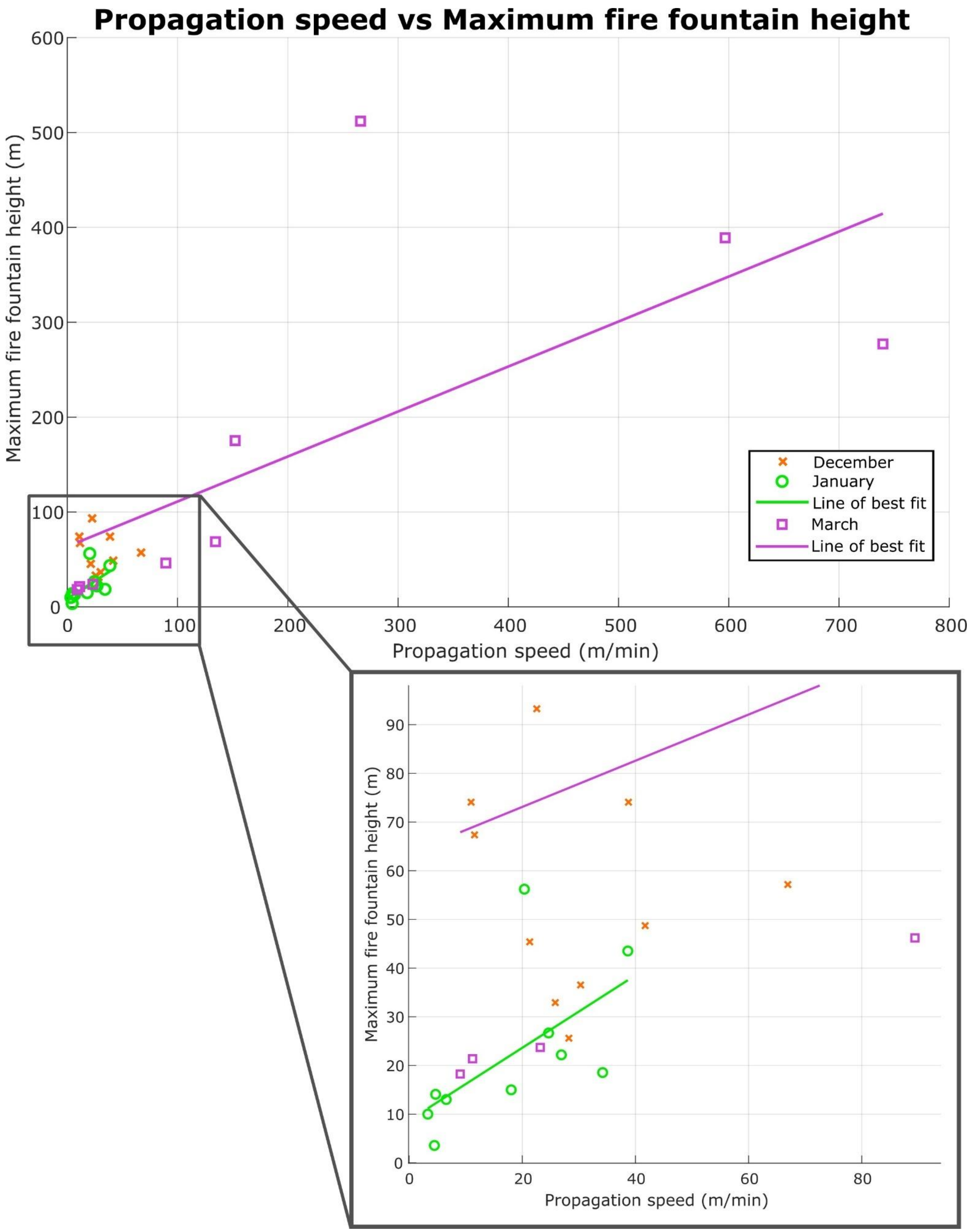

Fig.4.10: Correlation plot between fissure propagation speed of eruption and maximum fire fountain height from that fissure. Only best fit lines for correlations of moderate strength or greater have been shown. Best fit lines have been calculated using a least squares regression method, using the polyfit and polyval functions on MATLAB.

	Month	Pearson's R value	Correlation strength	Significant?
Propagation speed vs fire fountain height	*December*	0.1506	Negligible	No
	January	0.6008	Moderate	No
	March	0.6909	Moderate	Yes
Total volume erupted vs fire fountain height		0.5073	Moderate	Yes
Inflation duration vs fire fountain height		0.5074	Moderate	Yes
Eruption duration vs fire fountain height		0.4913	Weak	Yes
Inflation volume vs fire fountain height		0.0651	Negligible	No

Table.4.3: *Pearson's R value of the correlation maximum fire fountain heights and fissure propagation speed, total volume erupted, inflation duration, eruption duration and inflation volume. |R| < 0.3 negligible; |R| < 0.5 weak; |R| < 0.7 moderate; |R| < 0.9 strong; |R| > 0.9 very strong. Significant if p < 0.05*

Dike opening, like fissure length and width, likely also influences fire fountaining. Wider dike sections should correspond to higher mass eruption rates and taller fountains. The maximum dike opening occurs at ~1km depth between Hagafell and Sundhnúkur, shifting towards Sundhúnkur near the surface (fig.4.10). Other areas of significant opening occur at Grindavík, Hagafell, and Stóra Skógafell. Despite the greatest opening occuring between Hagafell and Sundhnúkur, only two small fissures formed there during the May eruption, who's fountains are unmeasured. In contrast, the high dike opening at Grindavík and Hagafell likely facilitated the January fissures. Fissures consistently form between Sundhnúkur and Stóra Skógafell and produce the tallest fountains, despite relatively lower dike opening. This suggests an inclined magma pathway, likely due to strong material in the shallow crust restricting opening above the area of maximum dike opening at depth.

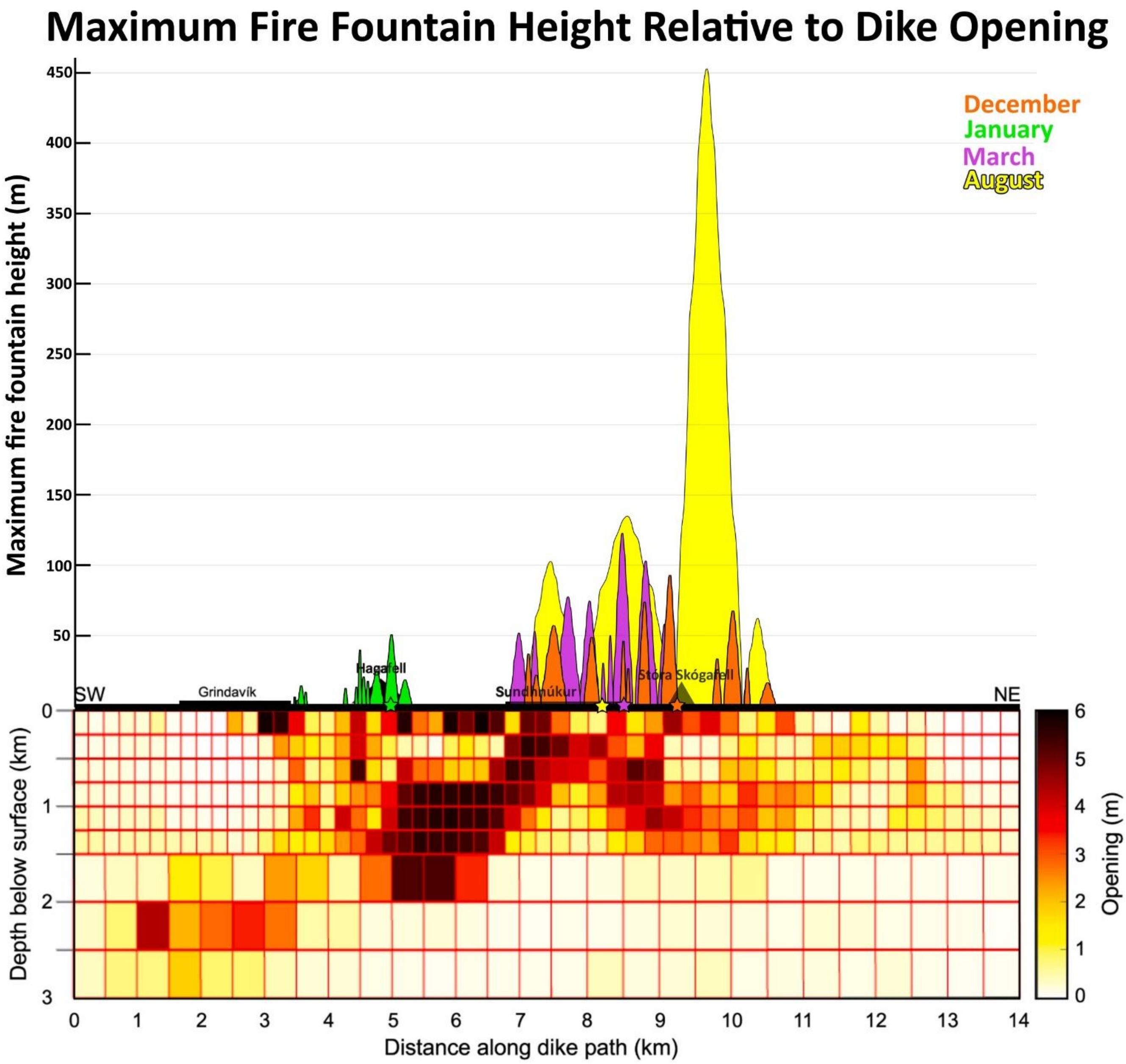

Fig.4.10: *Areas of maximum dike opening relative to measured fire fountains. Maximum dike opening has been extracted from text figure 8; Parks et al., 2025. Fire fountains have been coloured according to the eruption they occurred in. Start locations of eruptions have been shown with a star of the according colour. Fire fountain shapes are schematic.*

5 Predictability

Short and long term predictiability of the times, durations and character of these eruptions is important in order for Icelanders to coexist safely with these eruptions for the next few centuries. This has become increasingly important in recent months given the removal of cordons and security around the lava flows meaning that tourists are now free to hike over the eruption sites without limitation.

5.1 Short-Term Predictability

High-confidence predictions of eruptions of the SVS can be made up to a few hours before an eruption from common unrest patterns. Each eruption of the SVS follows the same pattern of precursor unrest (fig.5.1). Inflation occurs at Svartsengi at a depth of 5km (Sigmundsson et al., 2024) as the mid-crustal magma domain recharges with depleted magma from depth (Matthews et al., 2024). Once the magma reservoir reaches some critical volume, there is a large earthquake swarm accompanying the injection of a dike occurring between 30 – 90 minutes before the fissure-fed eruption begins (with the exception of the January eruption which began 5 hours after dike injection seismicity; IMO, 2024a, fig.5.2, fig.5.3). The critical magma volume required before an eruption is triggered has increased with every eruption (fig.5.4), and the rate of infill has decreased, leading to longer periods of repose between eruptions (IMO, 2024a, fig.5.5).

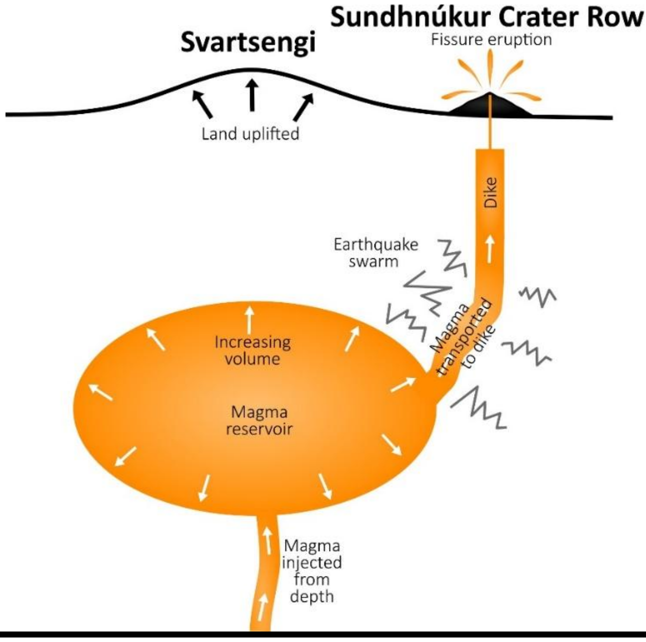

Fig.5.1: *Schematic diagram of the repeated pattern of precursor unrest prior to eruptions of the SVS*

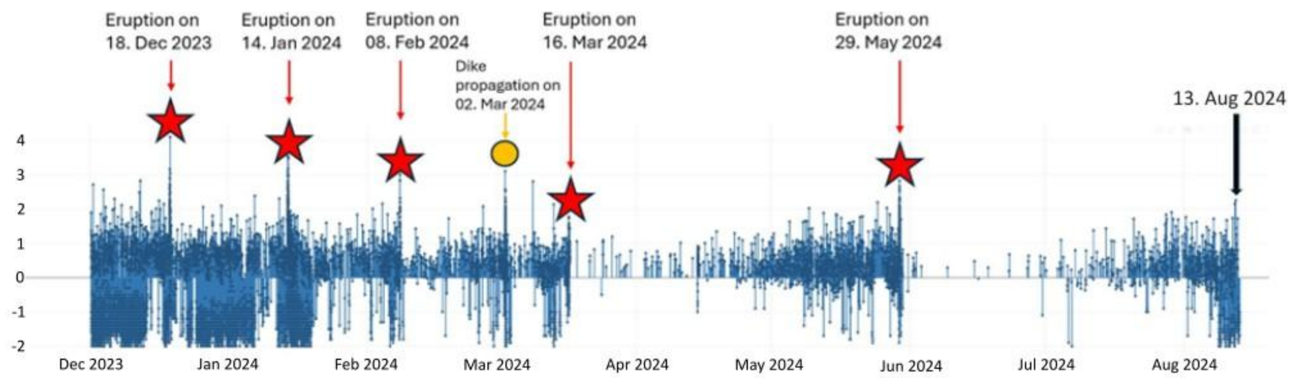

Fig.5.2: *Seismicity before eruptions of the SVS (IMOa, 2024)*

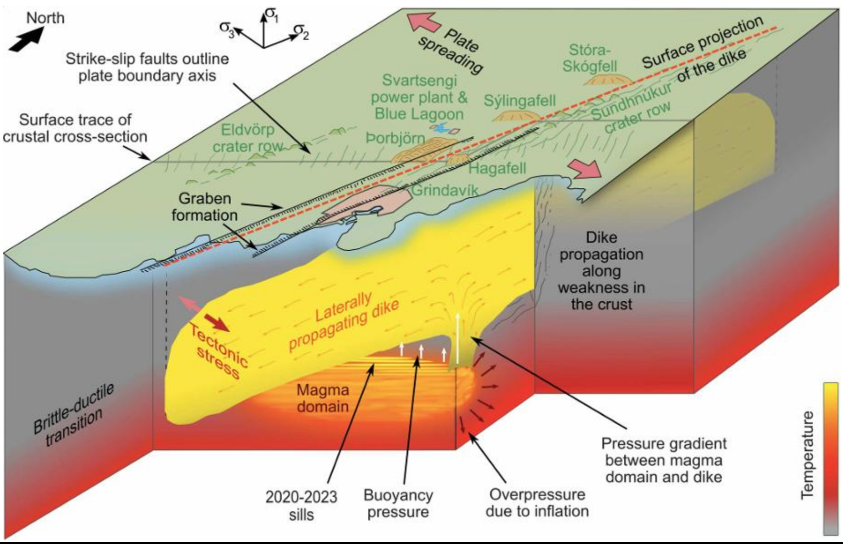

Fig.5.3: *Illustration of the Grindavík dike and the proposed magma domain under Svartsengi. Also shown is the graben (black lines) which formed through Grindavík during the injection of this dike on 11th November 2023. The surface project of the dike is outlined in red, and the crustal cross sections outlined in grey. Not to scale. (Sigmundsson et al., 2024, text fig.5.c)*

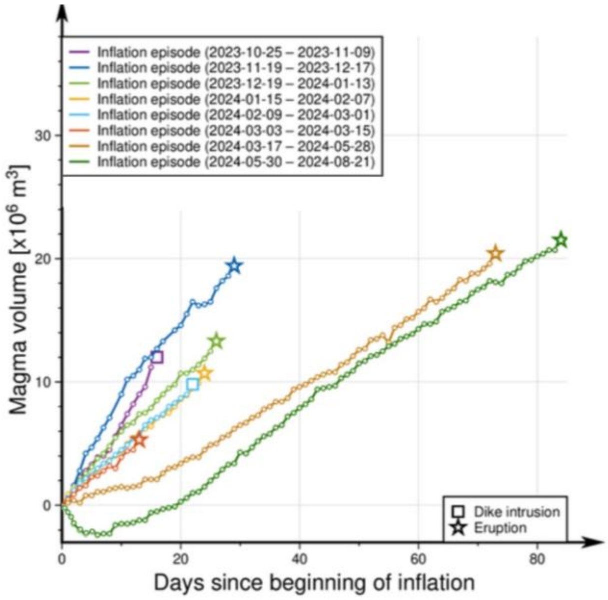

Fig.5.4: *Duration and volume of inflation prior to eruptions of the SVS (IMOa, 2024). Volumes were estimated using geodetic modelling, assuming a Mogi inflation source within a uniform elastic half space (Sigmundsson et al., 2024; Mogi, 1958)*

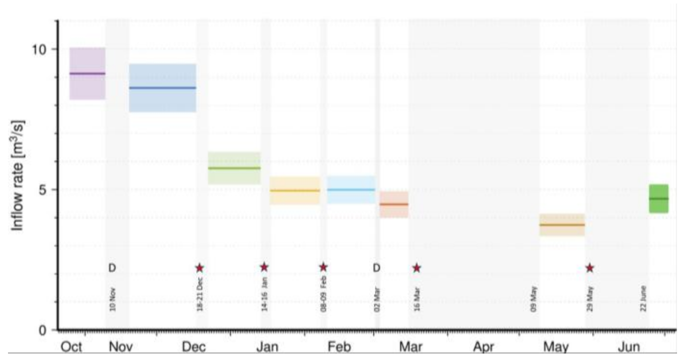

Fig.5.5: *Inflow rate into magma system prior to eruptions of the SVS. Star = eruption, D = dike injection with no eruption. (IMOa, 2024)*

Continued eruptions of the SVS are weakening the crust, meaning that precursor seismicity is reducing with every eruption. If this seismic activity is missed, those nearby need an alternative method to detect when and where an eruption will occur.

Before every SVS eruption, steam is emitted from the exact fissure location up to minutes before an eruption. Before the August eruption, steam was visible ~40 seconds before fissure opening (fig.5.6). The duration that steam is visible is largely dependent on light conditions. Similar observations were made during the Fagradalsfjall eruptions (Hjartardóttir et al., 2023) where steam was visible for 15 – 90 seconds at night and 9 – 23 minutes in daylight prior to an eruption.

The greatest immediate risk is to hikers, who are typically active during the day. Given that steam is visible several minues before an eruption, this provides sufficient time to move to safety.

21:25:14

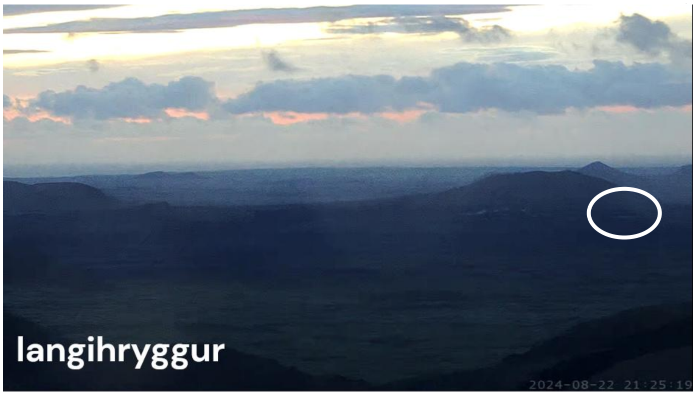

Steam is first visible: 21:25:19

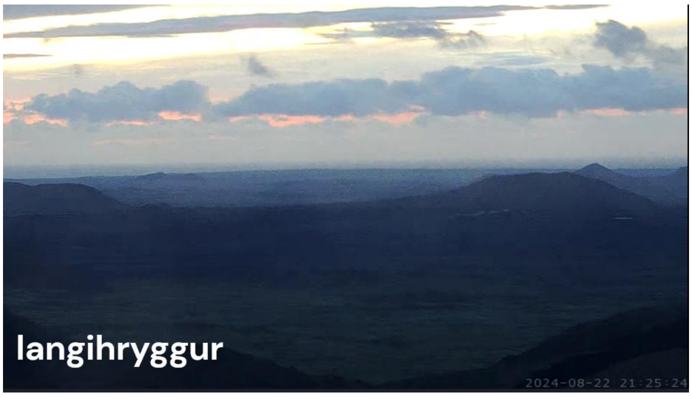

21:25:24

21:25:29

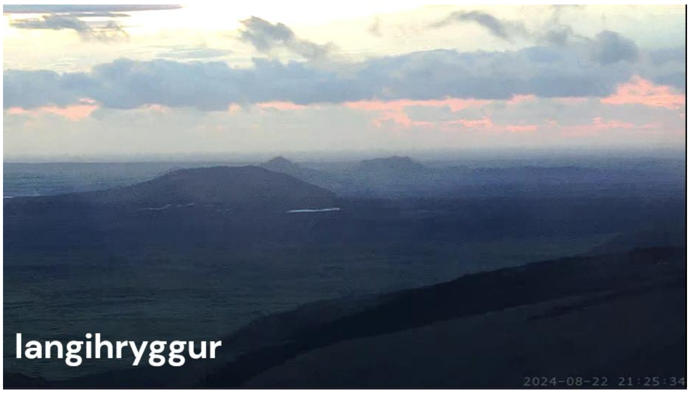

21:25:34

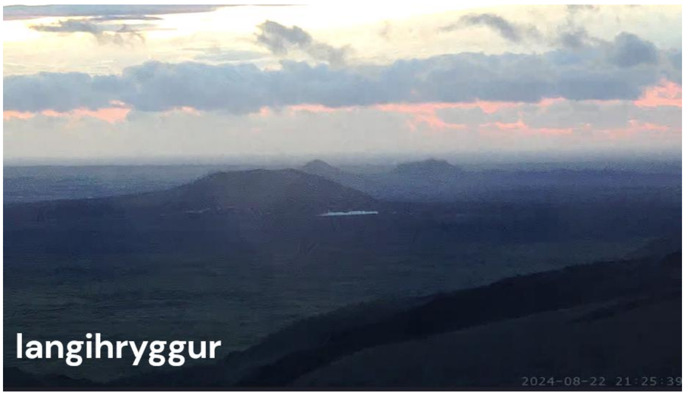

21:25:39

21:25:44

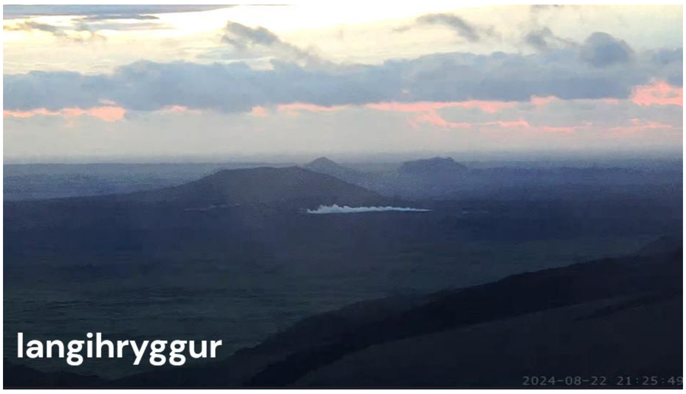

21:25:49

Fig.5.6: *Snapshots of the extrusion of steam prior to the August 2024 eruption of the SVS from the LFI Langihryggur camera*

5.2 Predictive Statistics

Predictive statistics uses correlations to predict eruption characteristics based on measurements that can be made in the first few hours of an eruption, or before it begins. The strongest correlation found between a potential controlling factor and an eruption characteristic was between inflation duration and total erupted volume. Findings from the first six eruptions have been used to test the accuracy of this predictive correlation by applying it to the November 2024 eruption (20/11/24). Inflation lasted 75 days before the eruption and a total of 49 million m^3 of lava was erupted (IMO, 2024a). The model predicted an erupted volume of 51.9 (+/- 17.4)[f] million m^3 – remarkably close to the actual volume. This suggests it may be possible to estimate lava output before an eruption begins, and tracking the eruption rate during an eruption could allow predictions to be made of when the eruption will end.

As more eruptions occur and additional data becomes available, the model will improve. The November 2024 eruption data can now be integrated into the model to estimate the expected lava volume if an eruption were to occur today[g]. With 103 days of inflation, the model predicts an erupted volume of 72.6 (+/- 20.0)[f] million m^3 (fig.5.7). Using the average volume eruption rate of 4.3 million m^3/day, this eruption would be expected to last 17 days. However, it is important to take this prediction with a grain of salt because this inflation duration is beyond the bounds of our current dataset.

[f] 95% confidence interval
[g] 4th March 2025

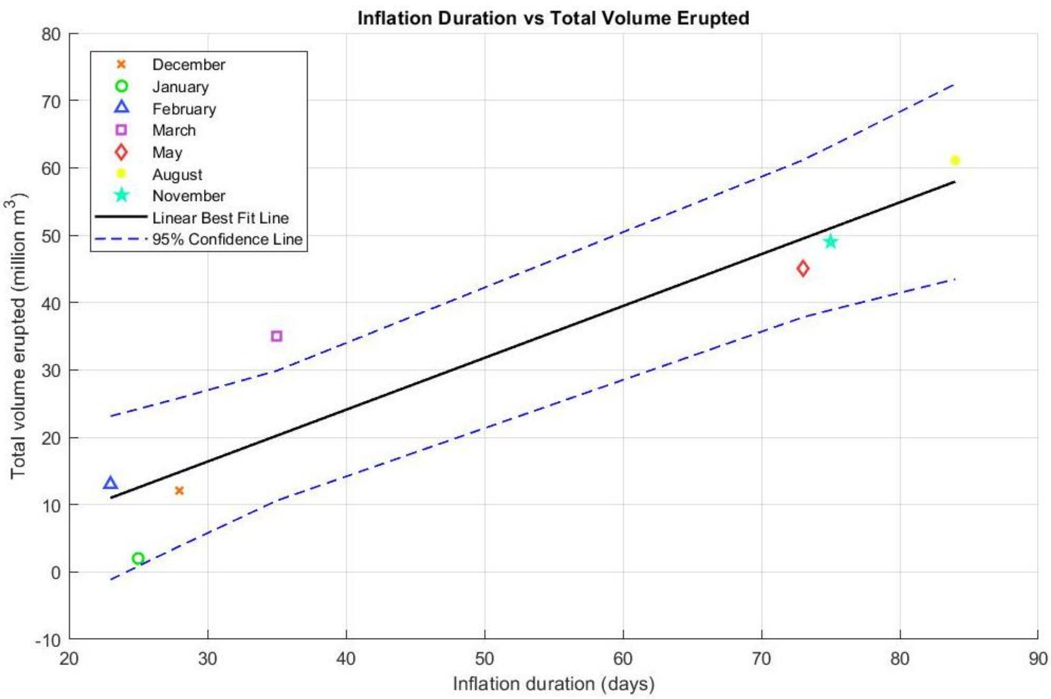

Fig.5.7: *Inflation duration prior to eruption vs total volume of lava erupted during an eruption. Line of best fit and confidence intervals plotted for prediction of expected volume erupted.*

To a lower degree of confidence it is also possible to predict total fissure length from its strong correlation with inflation duration[h]. Applying this to the November eruption, the model predicted a fissure length of 3955.572 m (+/- 1793.462[i]). The actual length was 3400m (IMO, 2024a), making this prediction less precise, but still within a 90% confidence interval. If an eruption occurred today[g], the fissure is expected to be 4935.320 m (+/- 2130.725[i]; fig.5.8).

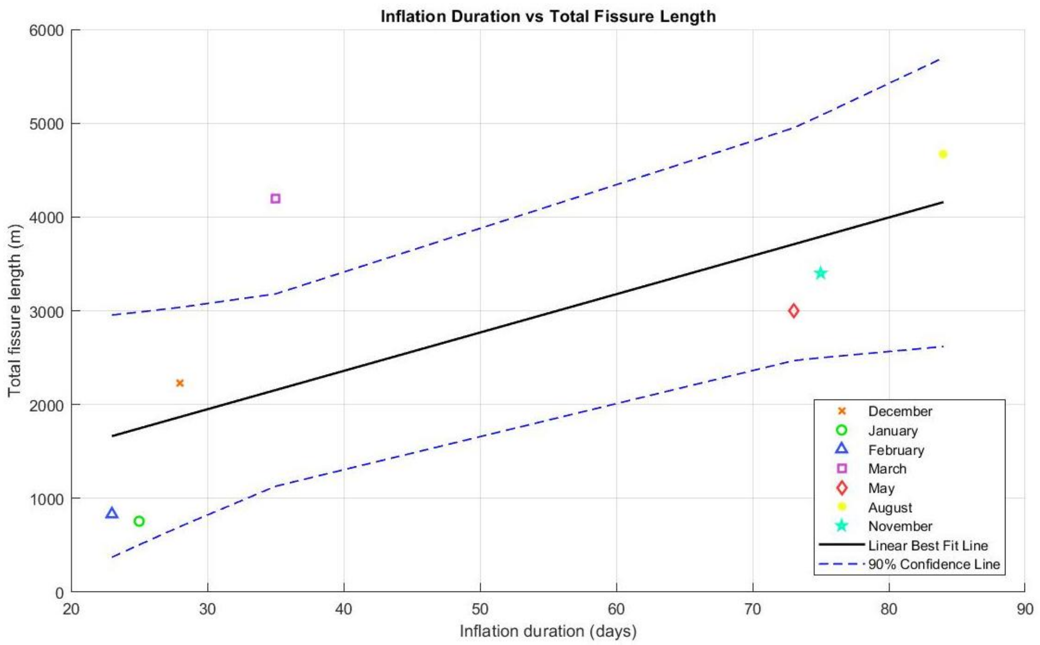

Fig.5.8: *Inflation duration prior to eruption vs total fissure length during an eruption. Line of best fit and confidence intervals plotted for prediction of expected volume erupted.*

[h] Pearson's R value of 0.7151 for the first 6 eruptions
[i] 90% confidence interval

5.3 Where Will the Next Fissure Open?

If an eruption occurs on March 4th 2025, the fissure is expected to be 4935 (+/- 2131[i]) m long and will produce 72.6 (+/- 20.0[f]) million m^3 of lava. Using the fissure location controls outlined in Section 3, the next erupton can be predicted to initate between Svartsengisfell and Stóra Skógafell, then extend southwards to Sundhnúkur, deflecting around it, consistent with six of the seven SVS eruptions (fig.5.9). Later eruptions have shown a northwards propagation trend, so propagation north of Stóra Skógafell, following the old Sundhnúkur crater row and the August fissure is likely. If the fissure extends beyond the ~4900 m confident prediction, two possibilities emerge: (1) propagation further north into the unexploited region of the Sundhnúkur crater row, or (2) propagation southward along the normal faults through Hagafell, following the pattern of the May eruption.

While repeated fissure opening between Svartsengisfell and Stóra Skógafell is expected, a fissure forming in Grindavík is unlikely, but not impossible. The southern extent of the visible Sundhnúkur crater row has already been reached, faults in this region are sparse, and the N-S fault in central Grindavík is misaligned with the regional stress field. Additionally, Grindavík is far from the inflation center, meaning the stopping pressure (Buck et al., 2006) is likely to be reached before propagation can extend into Grindavík. However, the 10th November 2023 dike did extend under Grindavík (IMO, 2024a) and surtseyan eruptions have occurred during previous volcanic events on the RP (Sigurgeirsson, 2004), so fissure opening in Grindavík and into the sea is still an apparent threat.

In the north, fissures are yet to extend to the full extent of the Sundhnúkur crater row, suggesting future propagation could extend up to 1 km further north. As seen in the fault structures and past crater alignments, the stress field shifts near the rift margin, causing the fissures to become more rift-sub-parallel, trending NE rather than NNE (Clifton & Schlische, 2003; Clifton & Kattenhorn, 2006; fig.3.5). This means future far north fissures are likely to adopt a northeasterly orientation.

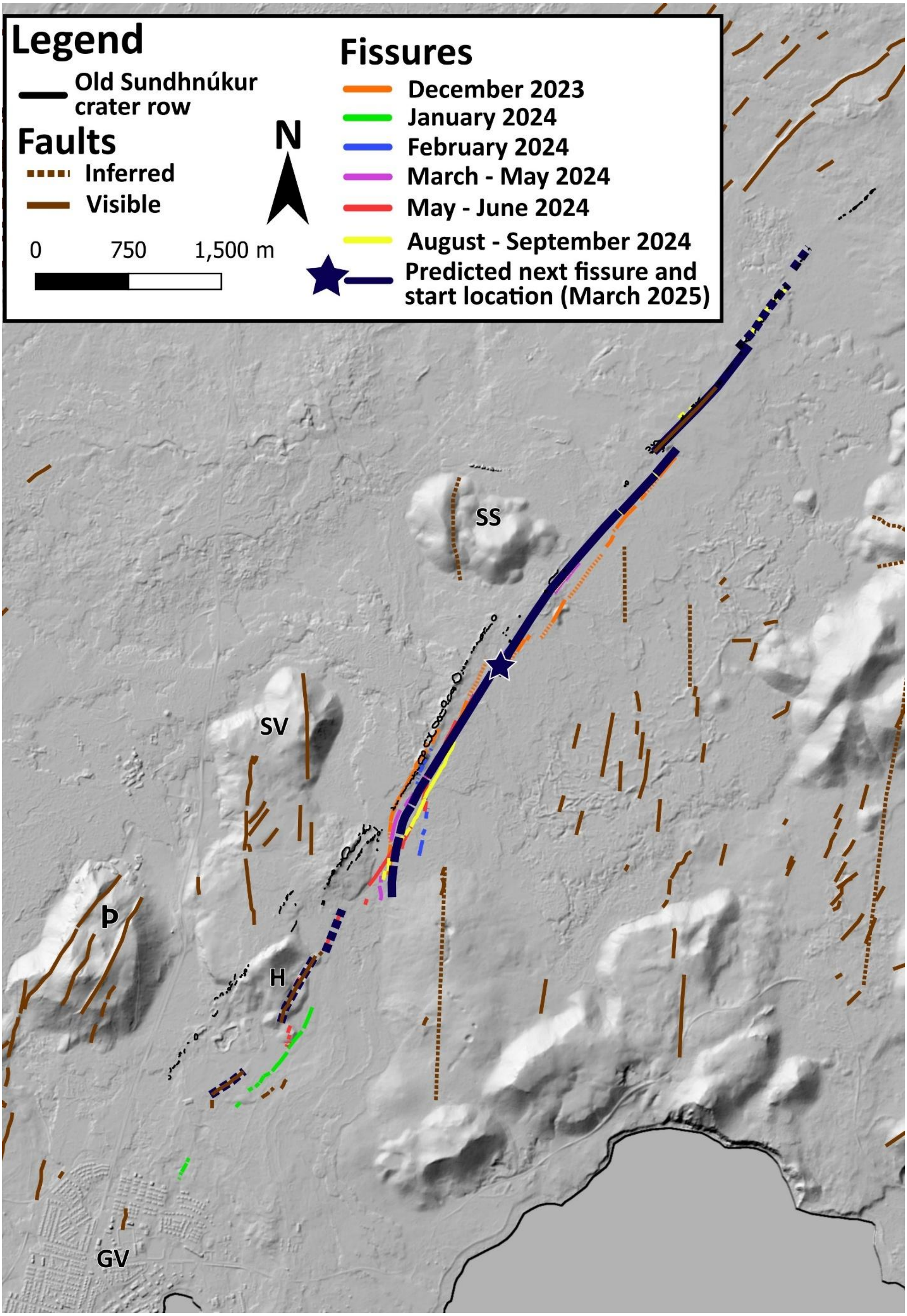

Fig.5.9: *Prediction of the locations a new fissure could open if an eruption occurred on 4th March 2025. Solid teal lines are the confident prediction and the dashed teal lines are the uncertain predictions if the fissure propagates into the upper uncertainty bound of length. GV = Grindavík; Þ = Þorbjorn; H = Hagafell; SV = Svartsengisfell; SS = Stóra Skógafell. Faults and old crater row from Jenness and Clifton, 2009. Base map DEM from: ÍslandsDEM, 2025*

6.1 Controls on Fissure Propagation

Fissure propagation is influenced by magma pressure, tectonic movement, crustal stress fields, normal faults (Pedicini et al., 2023), and geology (Tentler and Temperley, 2006). Fissure propagation occurs in bursts, with the fastest propagation early in an eruption before slowing. Within fissure segments, propagation speed variations arise from small-scale heterogeneities like cross-cutting faults and lithological differences. Long-term propagation trends appear to be driven by magma stress changes.

6.2 Controls on the Locations of Fissures

Fissure location is governed by least compressive stress direction (Anderson, 1951), preexisting crustal weaknesses (Delaney et al., 1986; Ziv and Rubin, 2000), crustal loading (Klügel et al., 2005; Walter and Amelung, 2006; Jenness and Clifton, 2009), and topography (Gaffney and Damjanac, 2006). These controls have different influences across the fissure field. In the south, Hagafell's high topography and structural weaknesses both deflect and preferentially allow fissure propagation. In the central field, Svartsengisfell and the old crater row deflect fissure due to crustal loading. In the north, minimal topography allows fissures to align perpendicular to the least compressive stress, along normal faults and the old crater row. Therefore the Sundhnúkur crater row can be re-exploited as a weakness, but topography and faults exert stronger controls when present. Understanding these influences improves fissure location prediction and hazard assessments.

6.3 Controls on Fire Fountain Heights

Fire fountain height is controlled by multiple factors, varying across spatial and temporal scales. Within an eruption, fissure segment length is the primary control, with longer fissures producing higher fountains. Variations seen in the August eruption also highlight the importance of conduit erosion.

Between eruptions, height differences may relate to magma volume, pressure and inflation duration, though correlations remain weak due to limited data. Magma volatile content is a widely accepted primary control (Head and Wilson, 1987; Moyer and Sahagian, 2024; Geshi et al., 2020), but its influence here is unclear given the lack of lava samples, and doubt cast by the shared magma domain limiting variation in magma characteristics.

Overall, within-eruption fountain variations are controlled by shallow crustal processes, while long-term differences reflect magma reservoir dynamics, similar to the trend observed in fissure propagation.

6.4 Predictability

Statistical models successfully predicted fissure length and erupted volume from inflation duration for the November 2024 eruption, demonstrating the potential to predict eruption characteristics before an eruption begins. However, extrapolating beyond previous eruptions should be approached with caution, as longer inflation periods may alter eruption dynamics. Future events will refine these models and clarify long-term trends.

As crustal weakening reduces precursor seismicity, alternative warning signals, such as steam emissions, will become increasingly important for short-term, close-proximity eruption prediction.

6.5 Future Research

Continued data collection will enhance long-term eruption forecasts, revealing stronger correlations and eliminating weaker ones. Future studies should explore whether fire fountains correlate with increased magma gas content by collecting lava samples.

Reinstating the disbanded webcam network is critical. Continuous, high-resolution monitoring is essential for refining models, improving eruption forecasts, and ensuring safety in the region. With eruptions expected to continue on the Reykjanes Peninsula for centuries (Sæmundsson et al., 2020), accurate prediction and characterisation of eruptions is essential.

Acknowledgements

Many thanks to my supervisors: Professor David Pyle (Oxford), Professor Tamsin Mather (Oxford), Dr Gro Pedersen (IMO) and Dr Michelle Parks (IMO). Thanks to David and Tamsin for their continued support, guidance and redirection throughout the project. Thanks to Gro for supplying the fissure and lava maps and for her advice on the mapping of the fissure propagation. Thanks to Michelle for her initial enthusiasm to create this project when I met with her in Iceland, and for her advice and guidance on how to navigate the IMO earthquake database, and for sharing with me the more detailed earthquake data. Finally thanks to the Icelandic Met Office for sharing the webcam footage and to Tamsin for collecting this footage from Iceland.

Now all glory to God who is able to do immeasurably more than we can ask or imagine.
Ephesians 3v20

Acocella, V. et al. (2024) Towards scientific forecasting of magmatic eruptions [Preprint]. doi:10.5194/egusphere-egu24-4441.

Anderson, E.M. (1951) *The dynamics of faulting and dyke formation with applications to Britain.* 2nd ed. Edinburgh: Oliver & Boyd.

Bagdassarov, N. (2021) ‘Density and Porosity’, in *Fundamentals of Rock Physics*. [Online]. United Kingdom: Cambridge University Press. pp. 28–65.

Belachew, M., Ebinger, C. and Coté, D. (2012) ‘Source mechanisms of dike-induced earthquakes in the Dabbahu-Manda Hararo rift segment in Afar, Ethiopia: Implications for faulting above dikes’, *Geophysical Journal International*, 192(3), pp. 907–917. doi:10.1093/gji/ggs076.

Bindeman, I.N., Deegan, F.M., Troll, V.R., Thordarson, T., Höskuldsson, Á., Moreland, W.M., Zorn, E.U., Shevchenko, A.V. and Walter, T.R . (2022) ‘Diverse mantle components with invariant oxygen isotopes in the 2021 Fagradalsfjall eruption, Iceland’, *Nature Communications*, 13(1). doi:10.1038/s41467-022-31348-7.

Bing (2025) *Bing satellite imagery*, *Bing*. Available at: https://www.bing.com/maps?cp=63.896967~-22.248823&lvl=10.9&style=h (Accessed: 25 January 2025).

Black, B.A., Karlstrom, L. and Mather, T.A. (2021) ‘The life cycle of large igneous provinces’, *Nature Reviews Earth & Environment*, 2(12), pp. 840–857. doi:10.1038/s43017-021-00221-4.

Bond, D.P.G. and Wignall, P.B. (2014) ‘Large igneous provinces and mass extinctions: An update’, *Volcanism, Impacts, and Mass Extinctions: Causes and Effects* [Preprint]. doi:10.1130/2014.2505(02).

Buck, W.R., Einarsson, P. and Brandsdóttir, B. (2006) ‘Tectonic stress and magma chamber size as controls on dike propagation: Constraints from the 1975–1984 Krafla rifting episode’, *Journal of Geophysical Research: Solid Earth*, 111(B12). doi:10.1029/2005jb003879.

Burgisser, A. and Degruyter, W. (2015) ‘Geometry of conduit’, in H. Sigurdsson (ed.) *The Encyclopedia of Volcanoes*. 2nd edn. London: Elsevier Science and Technology, pp. 230–231.

Calvari, S. *et al.* (2018) ‘Paroxysmal explosions, lava fountains and ash plumes at Etna Volcano: Eruptive Processes and Hazard Implications’, *Frontiers in Earth Science*, 6. doi:10.3389/feart.2018.00107.

Caracciolo, A., Bali, E., Halldórsson, S.A., Guðfinnsson, G.H., Kahl, M., Þórðardóttir, I., Pálmadóttir, G.L. and Silvestri, V. (2023) ‘Magma plumbing architectures and timescales of magmatic processes during historical magmatism on the Reykjanes Peninsula, Iceland’, *Earth and Planetary Science Letters*, 621, p. 118378. doi:10.1016/j.epsl.2023.118378.

Clapham, M.E. and Renne, P.R. (2019) ‘Flood basalts and mass extinctions’, *Annual Review of Earth and Planetary Sciences*, 47(1), pp. 275–303. doi:10.1146/annurev-earth-053018-060136.

Clifton, A.E. and Kattenhorn, S.A. (2006) ‘Structural architecture of a highly oblique divergent plate boundary segment’, *Tectonophysics*, 419(1–4), pp. 27–40. doi:10.1016/j.tecto.2006.03.016.

Clifton, A.E. and Schlische, R.W. (2003) ‘Fracture populations on the Reykjanes Peninsula, Iceland: Comparison with experimental clay models of oblique rifting’, *Journal of Geophysical Research: Solid Earth*, 108(B2). doi:10.1029/2001jb000635.

Cubuk-Sabuncu, Y., Jónsdóttir, K., Caudron, C., et al., 2021. ‘Temporal seismic velocity changes during the 2020 rapid inflation at Mt. Thorbjörn-Svartsengi, Iceland, using seismic ambient noise.’ *Geophysical Research Letters*, 48(11). Available at: https://doi.org/10.1029/2020GL092265

Delaney, P.T. *et al.* (1986) ‘Field relations between dikes and joints: Emplacement processes and paleostress analysis’, *Journal of Geophysical Research: Solid Earth*, 91(B5), pp. 4920–4938. doi:10.1029/jb091ib05p04920.

DeMets, C., Gordon, R.G., Argus, D.F. and Stein, S., 1994. Effect of recent revisions to the geomagnetic reversal time scale on estimates of current plate motions. *Geophysical Research Letters*, 21, pp.2191–2194.

Ducrocq, C., Árnadóttir, T., Einarsson, P., Jónsson, S., Drouin, V., Geirsson, H. and Hjartardóttir, Á.R. (2024) ‘Widespread fracture movements during a volcano-tectonic unrest: The Reykjanes Peninsula, Iceland, from 2019–2021 terrasar-X interferometry’, *Bulletin of Volcanology*, 86(2). doi:10.1007/s00445-023-01699-0.

Einarsson, P. (1991) Earthquakes and present-day tectonism in Iceland. *Tectonophysics*. 189 (1), pp. 261–279.

Einarsson, P. (2008) ‘Plate boundaries, rifts and transforms in Iceland’, *Jökull*, 58(1), pp. 35–58. doi:10.33799/jokull2008.58.035.

Finnsson, H. (1796) 'Um mannfækkun af Hallærum á Íslandi' (Decimation of the population in Iceland due to famines), Rit þess konunglega íslenska lærdómslistafélags, XIV, pp. 30-226. Copenhagen. (In Icelandic)

Flóvenz, O.G., Wang, R., Hersir, G.P., et al., 2022. ‘Cyclical geothermal unrest as a precursor to Iceland’s 2021 Fagradalsfjall eruption.’ *Nature Geoscience*, pp.1–8. Available at: https://doi.org/10.1038/s41561-022-00930-5

Gaffney, E.S. and Damjanac, B. (2006) ‘Localization of volcanic activity: Topographic effects on dike propagation, eruption and Conduit Formation’, *Geophysical Research Letters*, 33(14). doi:10.1029/2006gl026852.

Geirsson, H., Parks, M., Vogfjörd, K., et al., 2021. ‘The 2020 volcano-tectonic unrest at Reykjanes Peninsula, Iceland: stress triggering and reactivation of several volcanic systems.’ *EGU General Assembly 2021*, pp.EGU21–7534. Available at: https://doi.org/10.5194/egusphere-egu21-7534

Geshi, N., Browning, J. and Kusumoto, S. (2020) ‘Magmatic overpressures, volatile exsolution and potential explosivity of fissure eruptions inferred via dike aspect ratios’, Scientific Reports, 10(1). doi:10.1038/s41598-020-66226-z.

Hálfdanarson, G. (1984) 'Loss of human lives following the Laki eruption', in Gunnlaugsson, G.A. and Rafnsson, S. (eds.) *Skaftáreldar 1783-1784: Ritgerðir og heimildir*. Reykjavík: Mál og Menning, pp. 139-162. (In Icelandic)

Hartley, M. and Maclennan, J. (2018) 'Magmatic densities control erupted volumes in Icelandic volcanic systems', *Frontiers in Earth Science*, 6. doi:10.3389/feart.2018.00029.

Head, J.W. and Wilson, L. (1987) 'Lava Fountain Heights at pu'u 'o'o, Kilauea, Hawaii: Indicators of amount and variations of exsolved magma volatiles', *Journal of Geophysical Research: Solid Earth*, 92(B13), pp. 13715–13719. doi:10.1029/jb092ib13p13715.

Heimisson, E.R., Hooper, A. and Sigmundsson, F. (2015) 'Forecasting the path of a laterally propagating dike', *Journal of Geophysical Research: Solid Earth*, 120(12), pp. 8774–8792. doi:10.1002/2015jb012402.

Hjartardóttir, Á.R., Dürig, T., Parks, M., Drouin, V., Eyjólfsson, V., Reynolds, H., Einarsson, P., Jensen, E.H., Óskarsson, B.V., Belart, J.M.C., Ruch, J., Gies, N.B. and Pedersen, G.B.M. (2023) 'Pre-existing fractures and eruptive vent openings during the 2021 Fagradalsfjall eruption, Iceland', *Bulletin of Volcanology*, 85(10). doi:10.1007/s00445 023-01670-z.

IMO (2024a) *Magma accumulation beneath and land uplift above Svartsengi continue*, *Icelandic Meteorological office*. Available at: https://en.vedur.is/about-imo/news/volcanic-unrest-grindavik (Accessed: 24 October 2024).

IMO (2024b) *IMO Earthquake Map*, *Skjalftalisa.vedur.is*. Available at: https://skjalftalisa.vedur.is/#/page/map (Accessed: 10 February 2025).

IMO. (1992). *Icelandic National Digital Seismograph Network* [Data set]. International Federation of Digital Seismograph Networks. https://doi.org/10.7914/zkjm-tj71

ÍslandsDEM (2025) *ÍslandsDEM*, *Kortasjá*. Available at: https://atlas.lmi.is/mapview/?application=DEM (Accessed: 30 April 2025).

Jenness, M.H. and Clifton, A.E. (2009) 'Controls on the geometry of a Holocene Crater Row: A field study from Southwest Iceland', *Bulletin of Volcanology*, 71(7), pp. 715–728. doi:10.1007/s00445-009-0267-9.

Jin-Yu, Z., Yan, C. and Xian-Xiang, H. (2009) 'Edge detection of images based on improved Sobel operator and genetic algorithms', *2009 International Conference on Image Analysis and Signal Processing*, pp. 31–35. doi:10.1109/iasp.2009.5054605.

Jóhannesson, H., 1980. Jardlagaskipan og þróun rekbelta á Vesturlandi (Evolution of rift zones in western Iceland, in Icelandic with English summary). *Náttúrufræðingurinn*, 50, pp.13–31.

Jónsson, J. (1983) 'Eldgos á sögulegum tíma á Reykjanesskaga', *Náttúrufræðingurinn*, 52, pp. 127–139.

Klügel, A., Walter, T.R., Schwarz, S. and Geldmacher, J., 2005. 'Gravitational spreading causes en-echelon diking along a rift zone of Madeira Archipelago: an experimental approach and implications for magma transport.' *Bulletin of Volcanology,* 68(1), pp.37–46.

Matthews, S.W., Caracciolo, A., Bali, E., Halldórsson, S.A., Sigmarsson, O., Guðfinnsson, G.H., Pedersen, G.B.M., Gunnarsson Robin, J., Marshall, E.W., Aden, A.A., Gísladóttir, B.Ý., Bosq, C., Auclair, D., Merrill, H., Levillayer, N., Löw, N., Rúnarsdóttir, R.H., Johnson, S.M., Steinþórsson, S., and Drouin, V., (2024) A dynamic mid-crustal magma domain revealed by the 2023 to 2024 Sundhnúksgígar eruptions, Iceland. *Science (American Association for the Advancement of Science)* 386 (6719), pp. 309–314.

Mitchell, K.L. (2005) 'Coupled conduit flow and shape in explosive volcanic eruptions', *Journal of Volcanology and Geothermal Research*, 143(1–3), pp. 187–203. doi:10.1016/j.jvolgeores.2004.09.017.

Mogi, K. (1958) ' Relations between the eruptions of various volcanoes and the deformation of the ground surfaces around them', *Bulletin of the Earthquake Research Institute*, 36, pp. 99–134.

Moyer, S. and Sahagian, D. (2024) 'Use of Pele's tears and spheres as an indicator of lava fountain height in Hawaiian volcanoes', Frontiers in Earth Science, 12. doi:10.3389/feart.2024.1379985.

Oskarsson, N., Grönvold, K. and Larsen, G. (1984) 'The haze associated with the Laki eruption', in Gunnlaugsson, G.A. and Rafnsson, S. (eds.) Skaftáreldar 1783-1784: Ritgerðir og heimildir. Reykjavik: Mál og Menning, pp. 67-80.

Pałgan, D., Devey, C.W. and Yeo, I.A. (2017) 'Volcanism and hydrothermalism on a hotspot–influenced ridge: Comparing Reykjanes Peninsula and Reykjanes Ridge, Iceland', *Journal of Volcanology and Geothermal Research*, 348, pp. 62–81. doi:10.1016/j.jvolgeores.2017.10.017.

Parks, M. *et al.* (2025) '2023–2024 inflation-deflation cycles at svartsengi and repeated dike injections and eruptions at the Sundhnúkur Crater Row, Reykjanes Peninsula, Iceland', *Earth and Planetary Science Letters*, 658, p. 119324. doi:10.1016/j.epsl.2025.119324.

Parks, M., Sigmundsson, F., Drouin, V., Hjartardóttir, Á.R., Geirsson, H., Hooper, A., Vogfjörd, K.S., Ófeigsson, B.G., Hreinsdóttir, S., Jensen, E.H., Einarsson, P., Barsotti, S. and Fridriksdóttir, H.M. (2023) 'Deformation, seismicity, and monitoring response preceding and during the 2022 Fagradalsfjall eruption, Iceland', *Bulletin of Volcanology*, 85(10). doi:10.1007/s00445-023-01671-y.

Pedicini, M. *et al.* (2023) 'A step forward to understanding the development of Volcanotectonic Rifts: The structure of the Fremrinamar Fissure Swarm (Iceland)', *Frontiers in Earth Science*, 11. doi:10.3389/feart.2023.1271721.

Piombo, A., Tallarico, A. and Dragoni, M. (2016) 'Role of mechanical erosion in controlling the effusion rate of basaltic eruptions', *Geophysical Research Letters*, 43(17), pp. 8970–8977. doi:10.1002/2016gl069737.

Rampino, M.R. and Self, S., 2015. Large igneous provinces and biotic extinctions. In *The encyclopedia of volcanoes* (pp. 1049-1058). Academic Press. doi:10.1016/B978-0-12-385938-9.00061-4

Roman, D.C. and Cashman, K.V. (2006) 'The origin of volcano-tectonic earthquake swarms', *Geology*, 34(6), p. 457. doi:10.1130/g22269.1.

Sæmundsson, K., Sigurgeirsson, M. and Friðleifsson, G.Ó. (2020) 'Geology and structure of the Reykjanes volcanic system, Iceland', *Journal of Volcanology and Geothermal Research*, 391, p. 106501. doi:10.1016/j.jvolgeores.2018.11.022.

Sahagian, D. (2005) 'Volcanic eruption mechanisms: Insights from intercomparison of models of Conduit Processes', *Journal of Volcanology and Geothermal Research*, 143(1–3), pp. 1–15. doi:10.1016/j.jvolgeores.2004.12.006.

Scott, S. *et al.* (2023) 'Near-surface magma flow instability drives cyclic lava fountaining at Fagradalsfjall, Iceland', *Nature Communications*, 14(1). doi:10.1038/s41467-023-42569-9.

Sigmundsson, F., Parks, M., Geirsson, H., Hooper, A., Drouin, V., Vogfjörd, K. S., Ófeigsson, B. G., Greiner, S. H. M., Yilin Yang, Y., Lanzi, C., De Pascale, G. P., Jónsdóttir, K., Hreinsdóttir, S., Tolpekin, V., Friðriksdóttir, H. M., Einarsson, P. and Barsotti, S. (2024) 'Fracturing and tectonic stress drive ultrarapid magma flow into dikes', *Science*, 383(6688), pp. 1228–1235. Doi:10.1126/science.adn2838.

Sigmundsson, F., Parks, M., Hooper, A., Geirsson, H., Vogfjörd, K.S., Drouin, V., Ófeigsson, G., Hreinsdóttir, S., Hjaltadóttir, S., Jónsdóttir, K., Einarsson, P., Barsotti, S., Horálek, J., and Ágústsdóttir, T. (2022) 'Deformation and seismicity decline before the 2021 Fagradalsfjall eruption', *Nature*, 609(7927), pp. 523–528. doi:10.1038/s41586-022-05083-4.

Sigurgeirsson, M.A. (2004) 'Þáttur Or gossögu Reykjaness: Gosskeið fyrir um tvö þúsund árum', Náttúrufræðingurinn, 72, pp. 21–28.

Spampinato, L. *et al.* (2008) 'Shallow magma transport for the 2002–3 Mt. Etna eruption inferred from Thermal Infrared Surveys', *Journal of Volcanology and Geothermal Research*, 177(2), pp. 301–312. doi:10.1016/j.jvolgeores.2008.05.013.

Tentler, T. and Temperley, S. (2006) 'Rock control of faulting: A case study from the Icelandic Rift Zone', *The Journal of Geology*, 114(4), pp. 449–470. doi:10.1086/504179.

Tentler, T. and Temperley, S. (2007) 'Magmatic fissures and their systems in Iceland: A tectonomagmatic model', *Tectonics*, 26(5). doi:10.1029/2006tc002037.

Thorarinsson, S. (1979) 'On the damage caused by volcanic eruptions with special reference to tephra and gases', in Sheets, P.D. and Grayson, D.K. (eds.) *Volcanic activity and human ecology*. New York: Academic Press, pp. 125-159.

Thordarson, T. and Self, S. (1993) 'The Laki (Skaftár Fires) and Grímsvötn eruptions in 1783-1785', *Bulletin of Volcanology*, 55(4), pp. 233–263. doi:10.1007/bf00624353.

Tyrell, G.W. (1937) 'Flood basalts and fissure eruption', *Bulletin Volcanologique*, 1(1), pp. 89–111. doi:10.1007/bf03028044.

Vinciguerra, S. *et al.* (2005) 'Relating seismic velocities, thermal cracking and permeability in Mt. Etna and Iceland basalts', *International Journal of Rock Mechanics and Mining Sciences*, 42(7–8), pp. 900–910. doi:10.1016/j.ijrmms.2005.05.022.

Walter, T.R. and Amelung, F. (2006) ‘Volcano-earthquake interaction at Mauna Loa Volcano, Hawaii’, *Journal of Geophysical Research: Solid Earth*, 111(B5). doi:10.1029/2005jb003861.

White, J.D.L. *et al.* (2009) ‘Physical volcanology of continental large igneous provinces: update and review’, in *Studies in Volcanology: The Legacy of George Walker*. London: Geological Society.

Wilson, L. and Head, J.W. (1981) ‘Ascent and eruption of basaltic magma on the Earth and moon’, *Journal of Geophysical Research: Solid Earth*, 86(B4), pp. 2971–3001. doi:10.1029/jb086ib04p02971.

Witt, T. and Walter, T.R. (2017) ‘Video monitoring reveals pulsating vents and propagation path of fissure eruption during the March 2011 pu’u ’ō’ō eruption, Kilauea Volcano’, *Journal of Volcanology and Geothermal Research*, 330, pp. 43–55. doi:10.1016/j.jvolgeores.2016.11.012.

Witt, T. and Walter, T.R. (2017a) ‘Video monitoring reveals pulsating vents and propagation path of fissure eruption during the March 2011 pu’u ’ō’ō eruption, Kilauea Volcano’, *Journal of Volcanology and Geothermal Research*, 330, pp. 43–55. doi:10.1016/j.jvolgeores.2016.11.012.

Witt, T. *et al.* (2018) ‘The relationship between lava fountaining and vent morphology for the 2014–2015 Holuhraun eruption, Iceland, analyzed by video monitoring and topographic mapping’, *Frontiers in Earth Science*, 6. doi:10.3389/feart.2018.00235.

Wolfe, E.W. *et al.* (1987) ‘The Puu Oo Eruption of Kilauea Volcano, Episodes 1-20, January 3, 1983, to June 8, 1984’, in *Volcanism in Hawaii*. U.S. Geological Survey Professional Paper (1350), pp. 471–507.

Ziv, A., Rubin, A.M. and Agnon, A. (2000) ‘Stability of dike intrusion along preexisting fractures’, *Journal of Geophysical Research: Solid Earth*, 105(B3), pp. 5947–5961. doi:10.1029/1999jb900410.

Appendix A: Fire Fountain Measurements

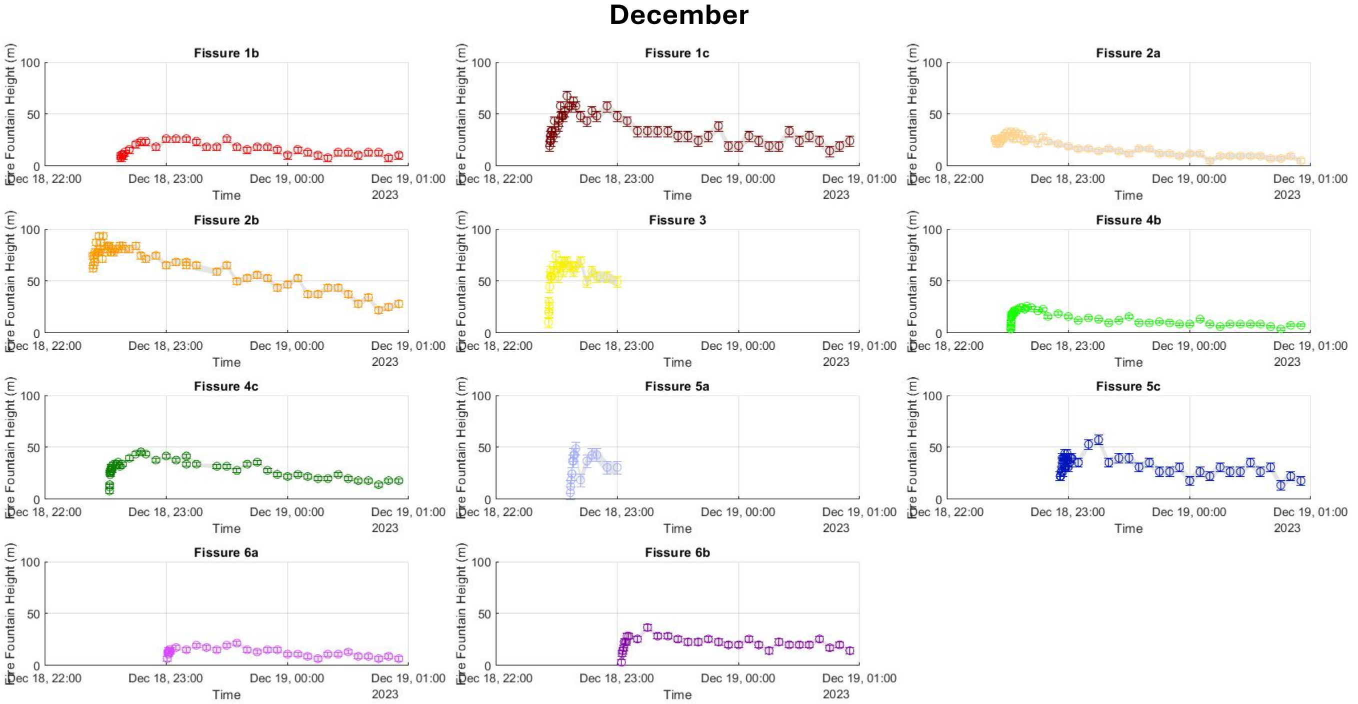

Fire fountain heights from each fissure segment during the December eruption. Heights have been scaled to be the same between fissure segments.

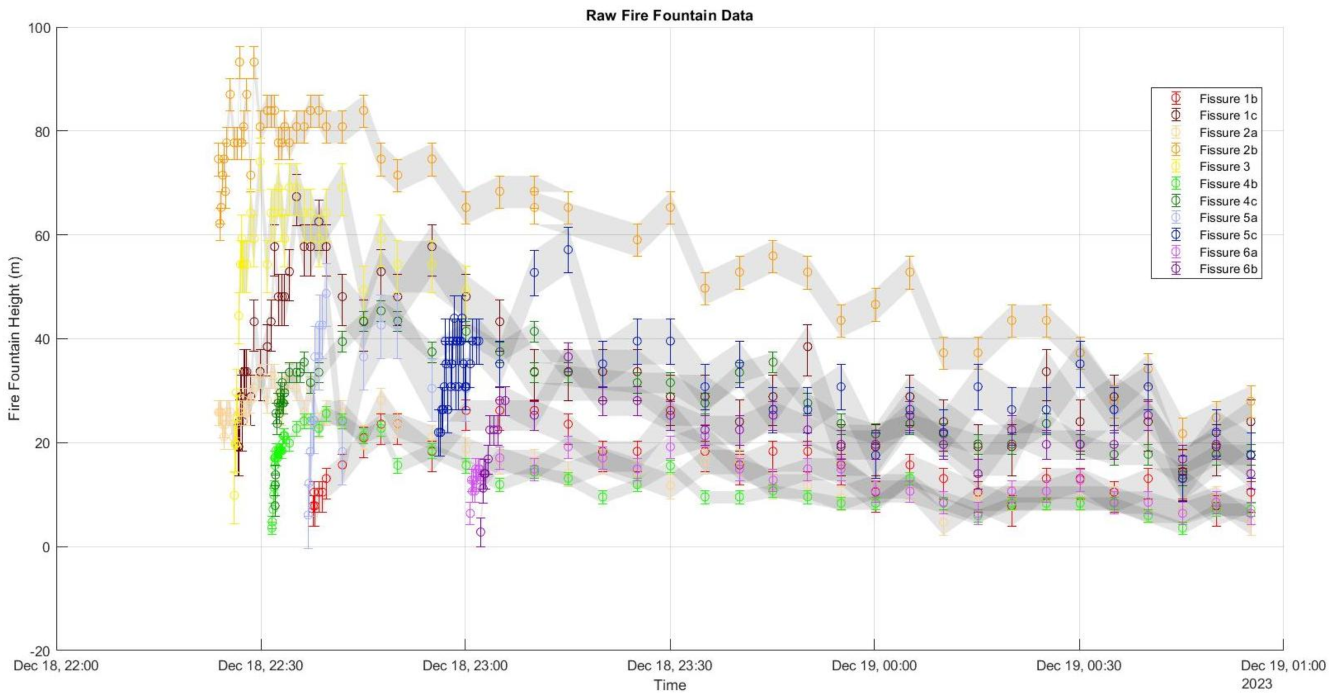

Fire fountain heights from each fissure segment during the December eruption on one plot.

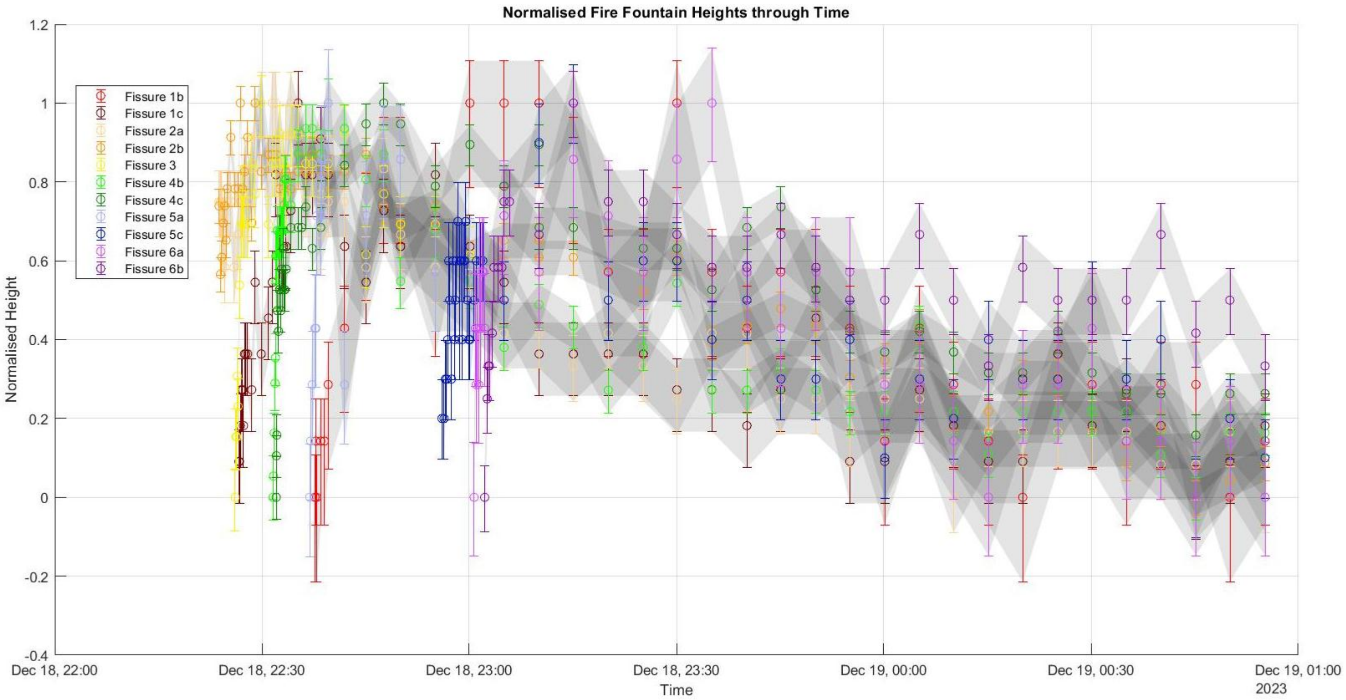

Fire fountain heights from the December eruption, normalised so each fissure segment has the same maximum and minimum fire fountain height.

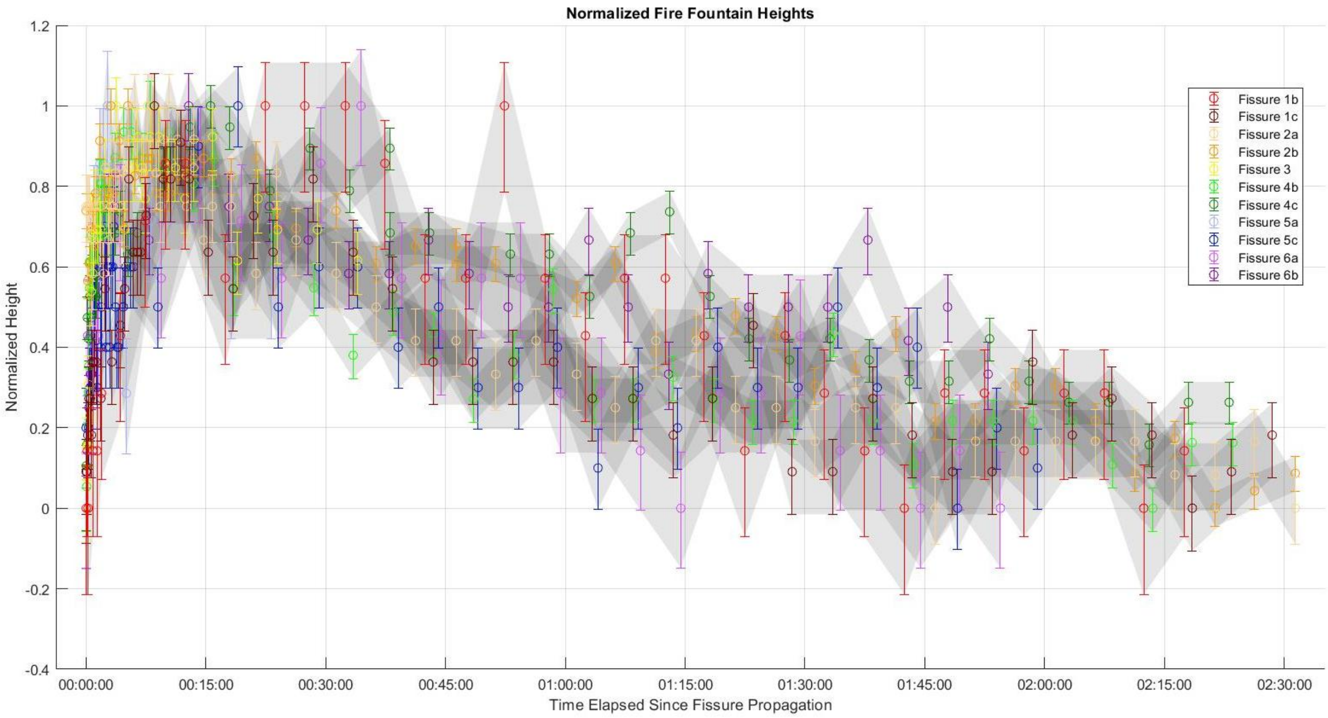

Fire fountain heights from the December eruption, normalised and shifted so each fissure segment has the same maximum and minimum fire fountain height and shifted so each segment opens at the same time.

January Fissure 1 and 2

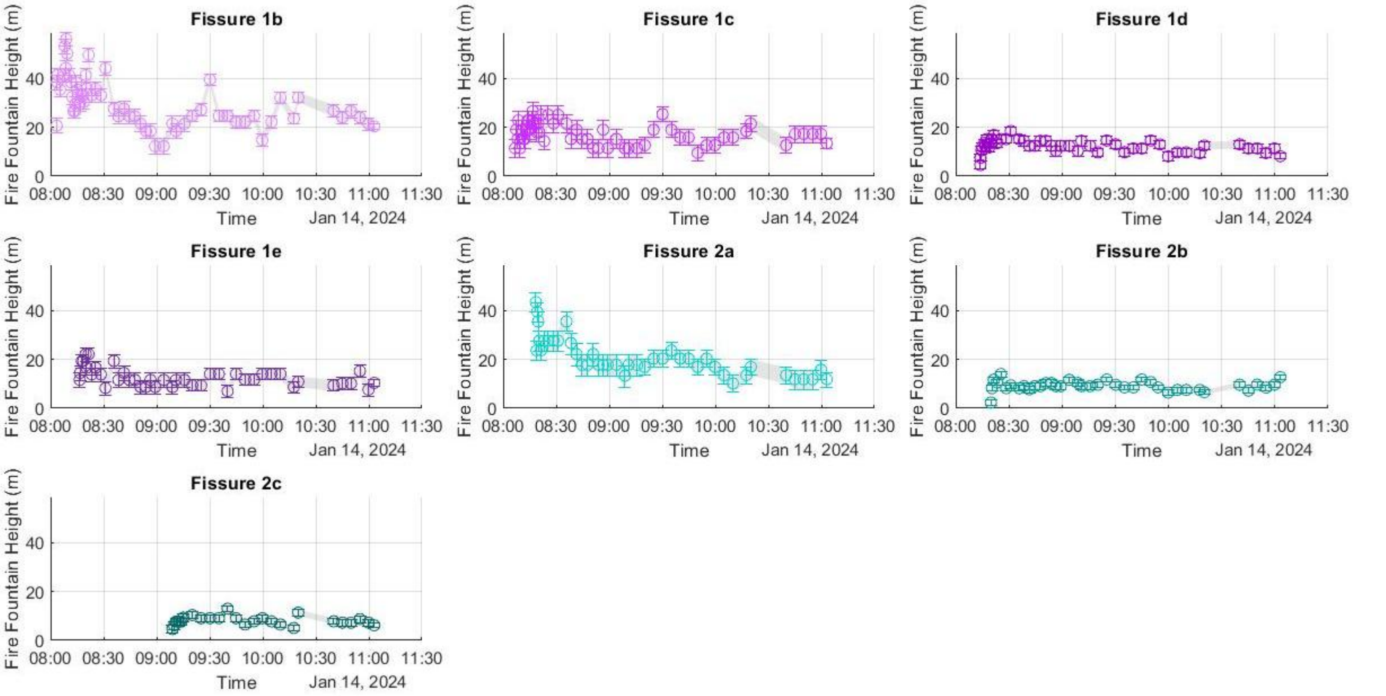

Fire fountain heights from each fissure segment from fissure 1 and 2 during the January eruption. Heights have been scaled to be the same between fissure segments.

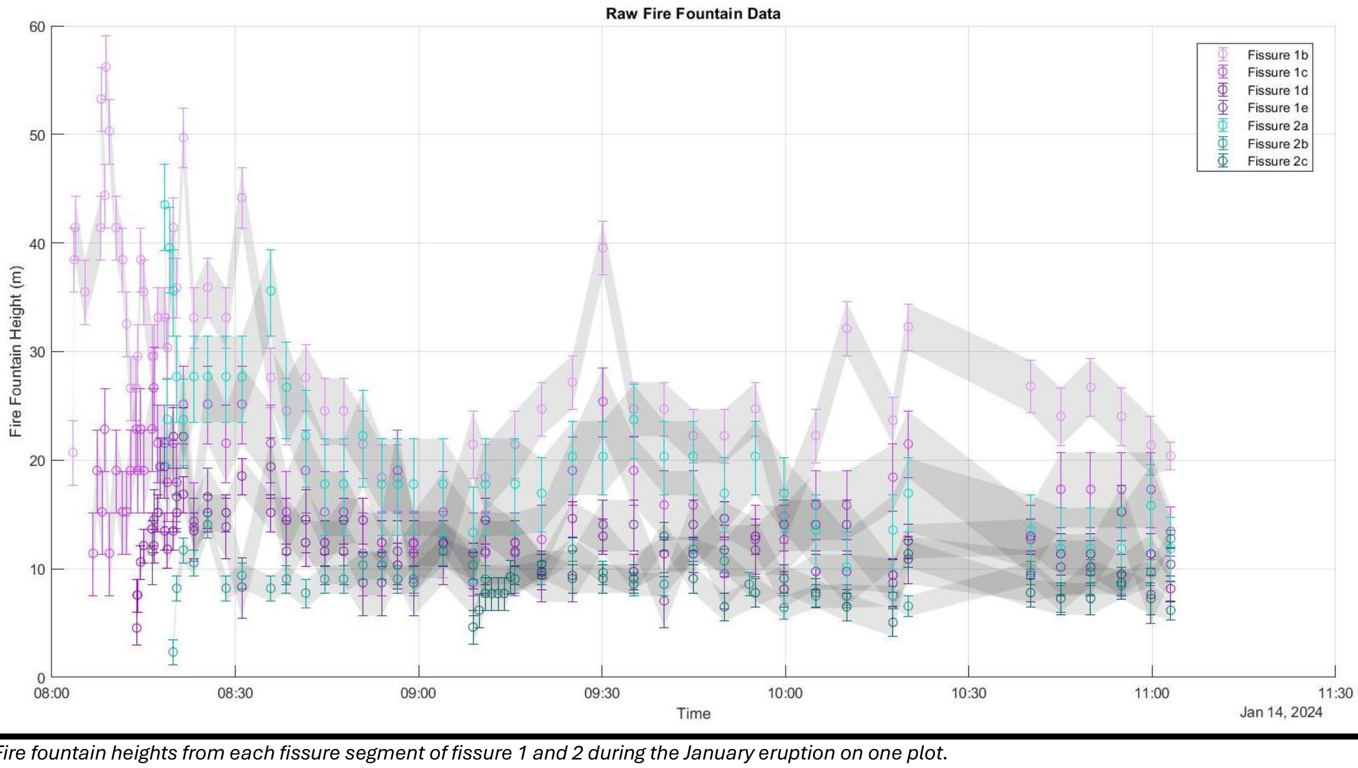

Fire fountain heights from each fissure segment of fissure 1 and 2 during the January eruption on one plot.

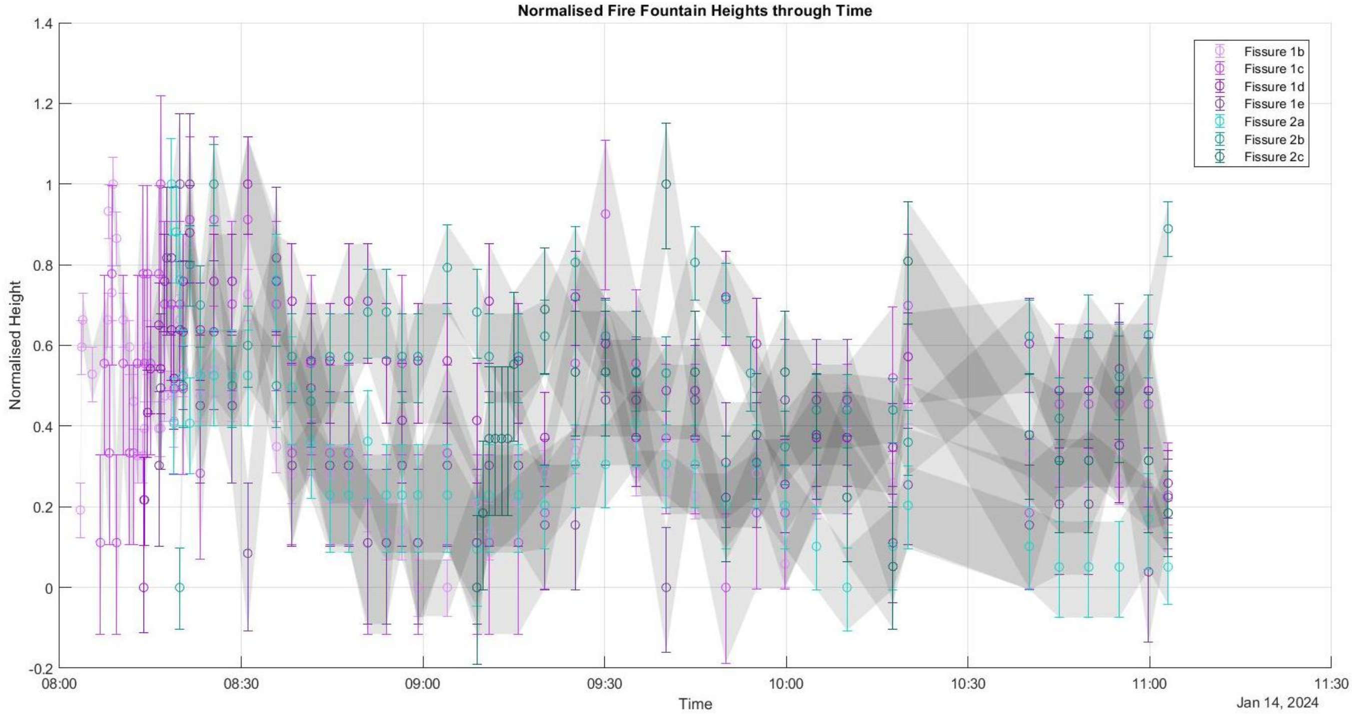

Fire fountain heights from the January eruption, normalised so each fissure segment of fissure 1 and 2 has the same maximum and minimum fire fountain height.

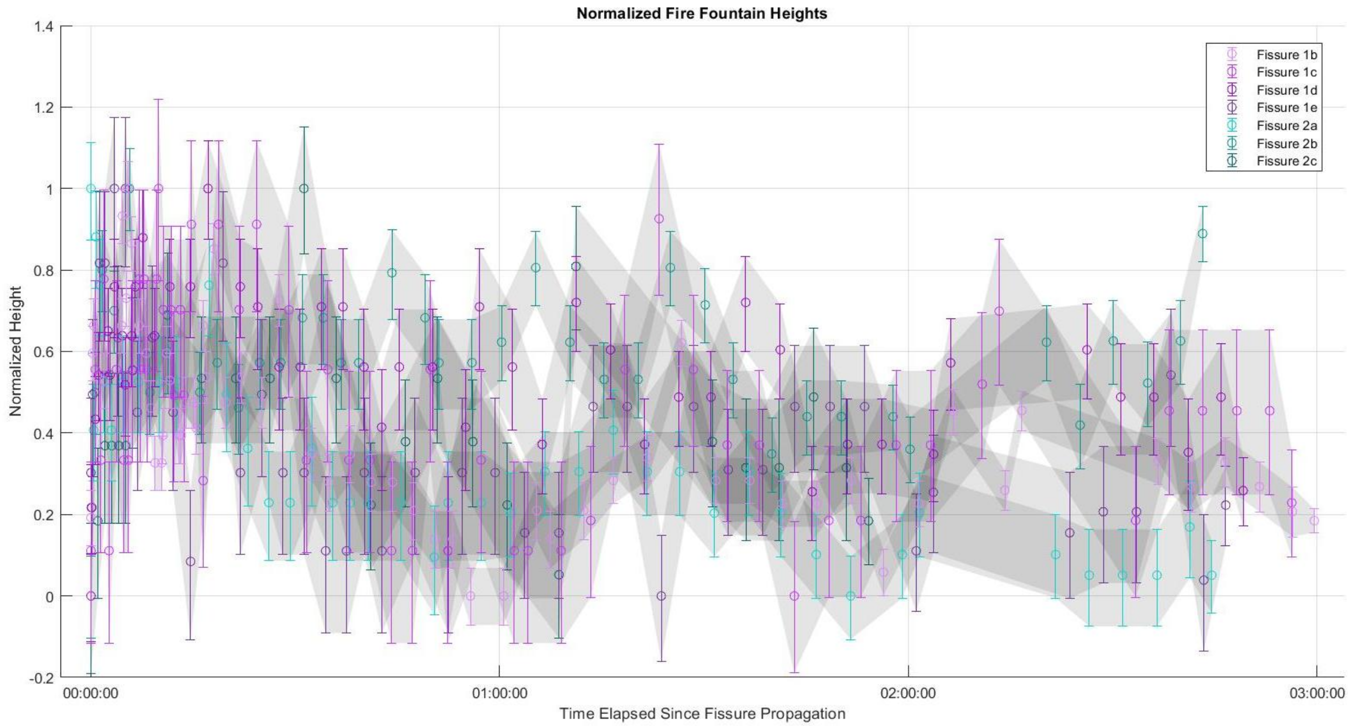

Fire fountain heights from the January eruption, normalised and shifted so each fissure segment from fissure 1 and 2 has the same maximum and minimum fire fountain height and shifted so each segment opens at the same time.

January Fissure 3

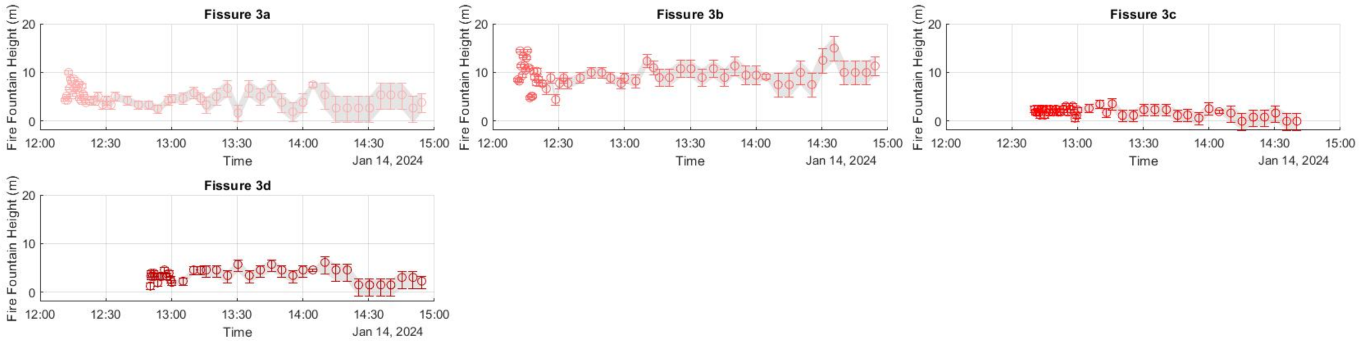

Fire fountain heights from each fissure segment from fissure 3 during the January eruption. Heights have been scaled to be the same between fissure segments.

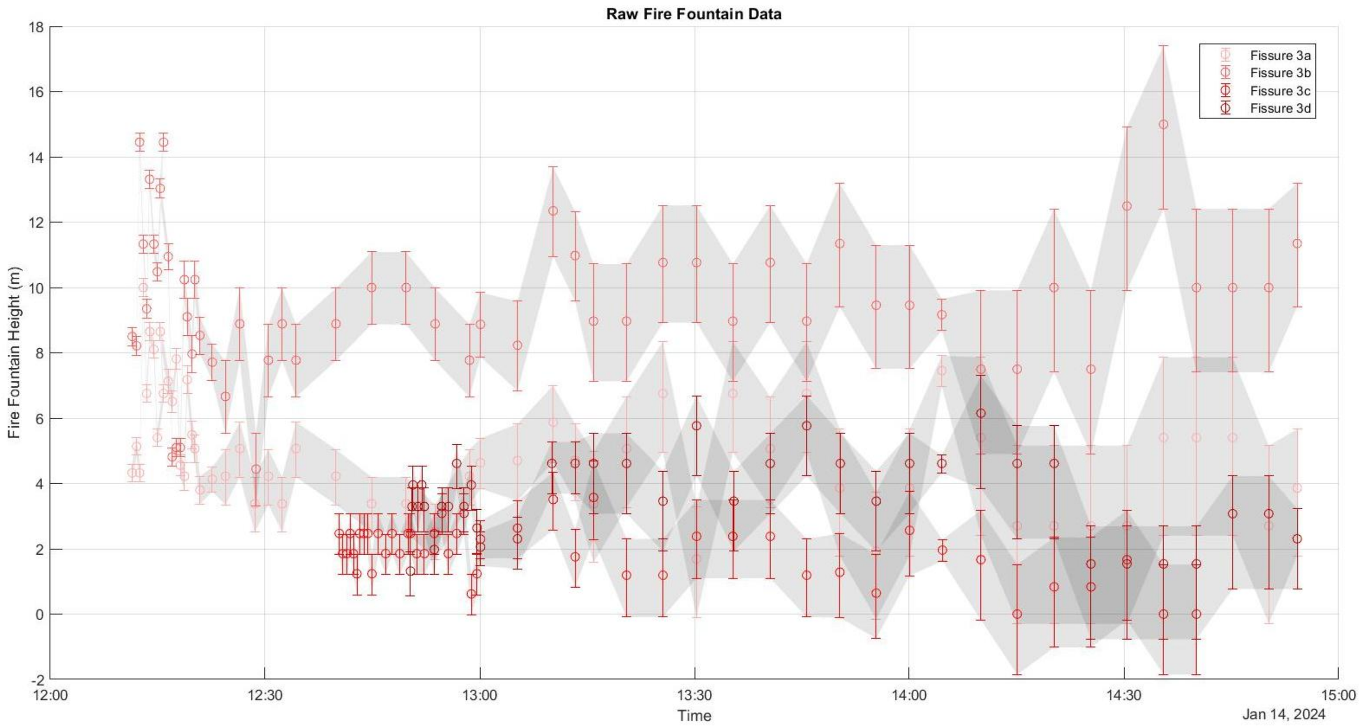

Fire fountain heights from each fissure segment of fissure 3 during the January eruption on one plot.

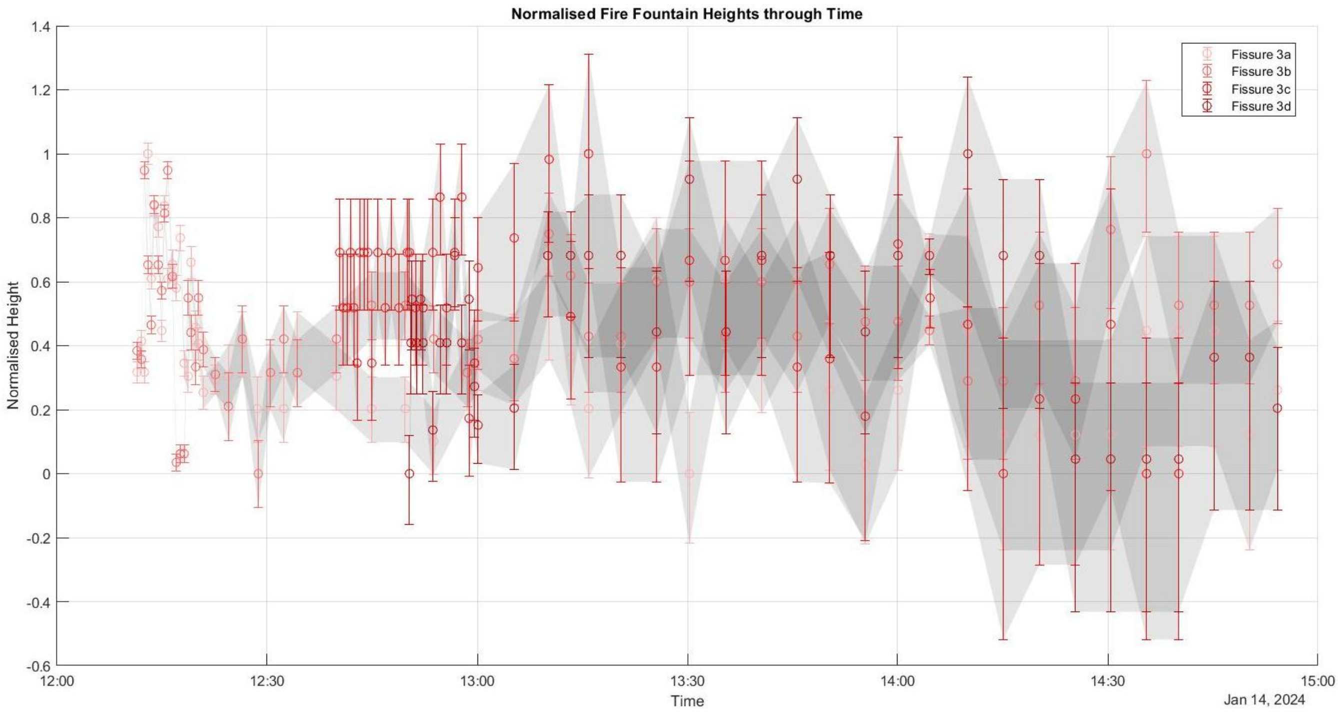

Fire fountain heights from the January eruption, normalised so each fissure segment of fissure 3 has the same maximum and minimum fire fountain height.

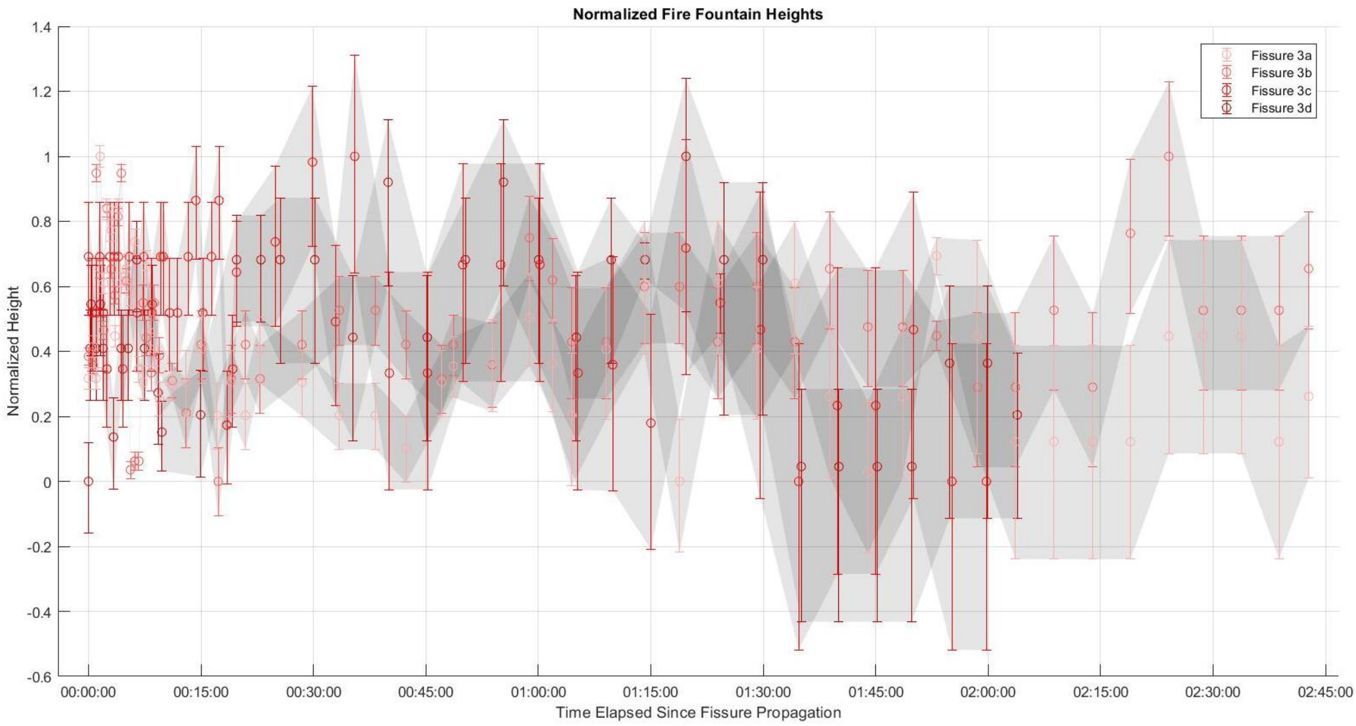

Fire fountain heights from the January eruption, normalised and shifted so each fissure segment from fissure 3 has the same maximum and minimum fire fountain height and shifted so each segment opens at the same time.

March

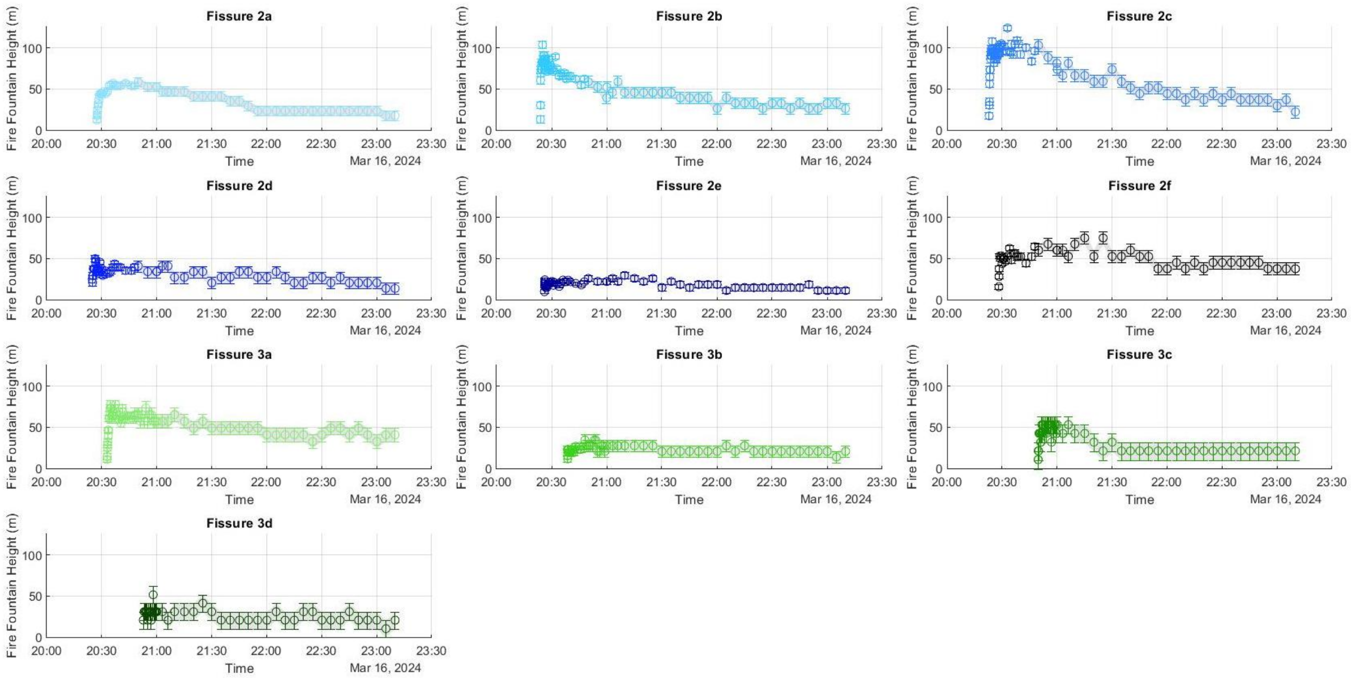

Fire fountain heights from each fissure segment during the March eruption. Heights have been scaled to be the same between fissure segments.

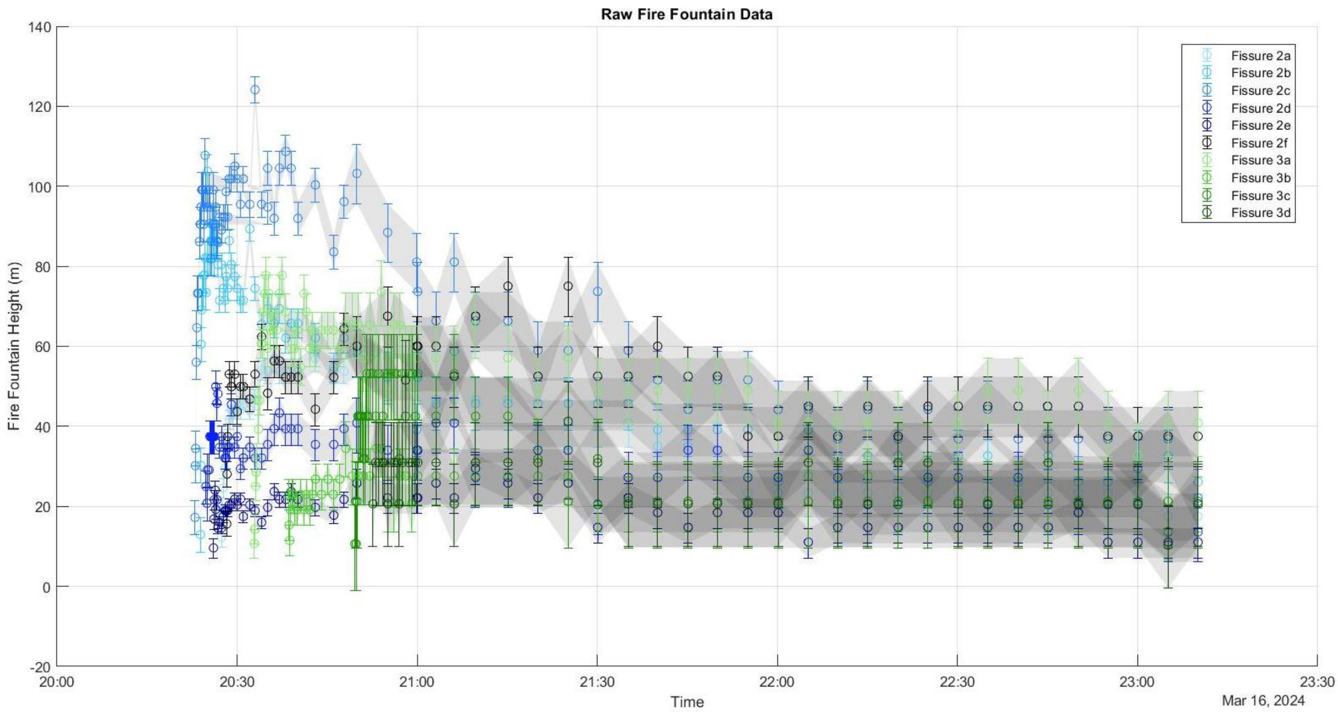

Fire fountain heights from each fissure segment during the March eruption on one plot.

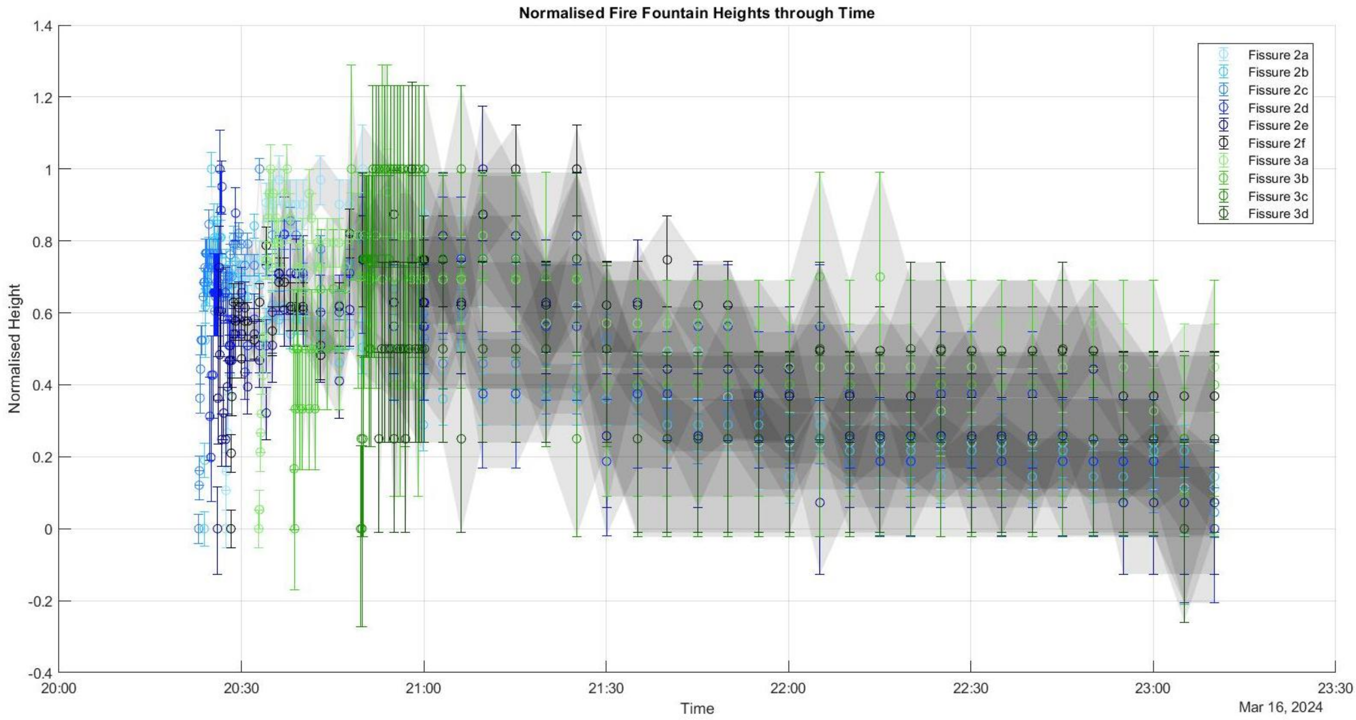

Fire fountain heights during the March eruption, normalised so each fissure segment has the same maximum and minimum fire fountain height.

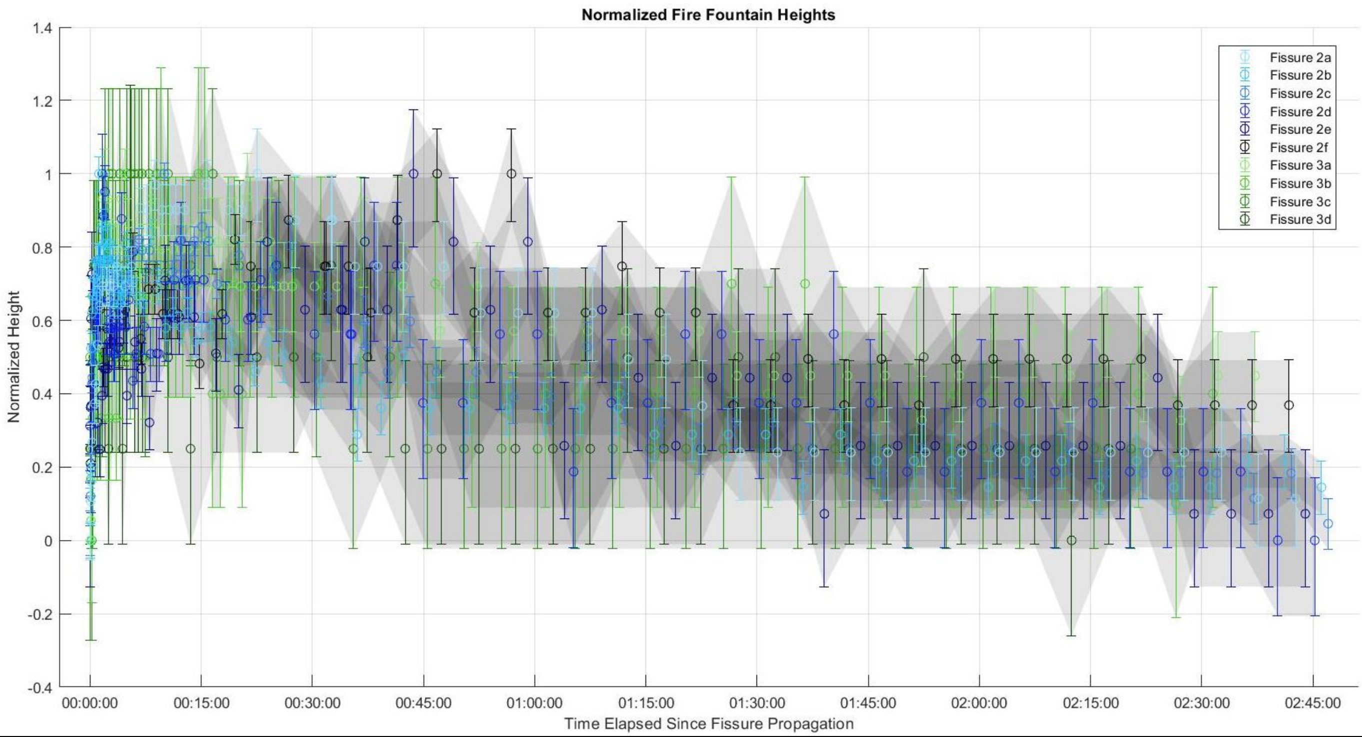

Fire fountain heights during the March eruption, normalised and shifted so each fissure segment has the same maximum and minimum fire fountain height and shifted so each segment opens at the same time.

Appendix B: Larger Versions of the Dike-Seismicity Figures

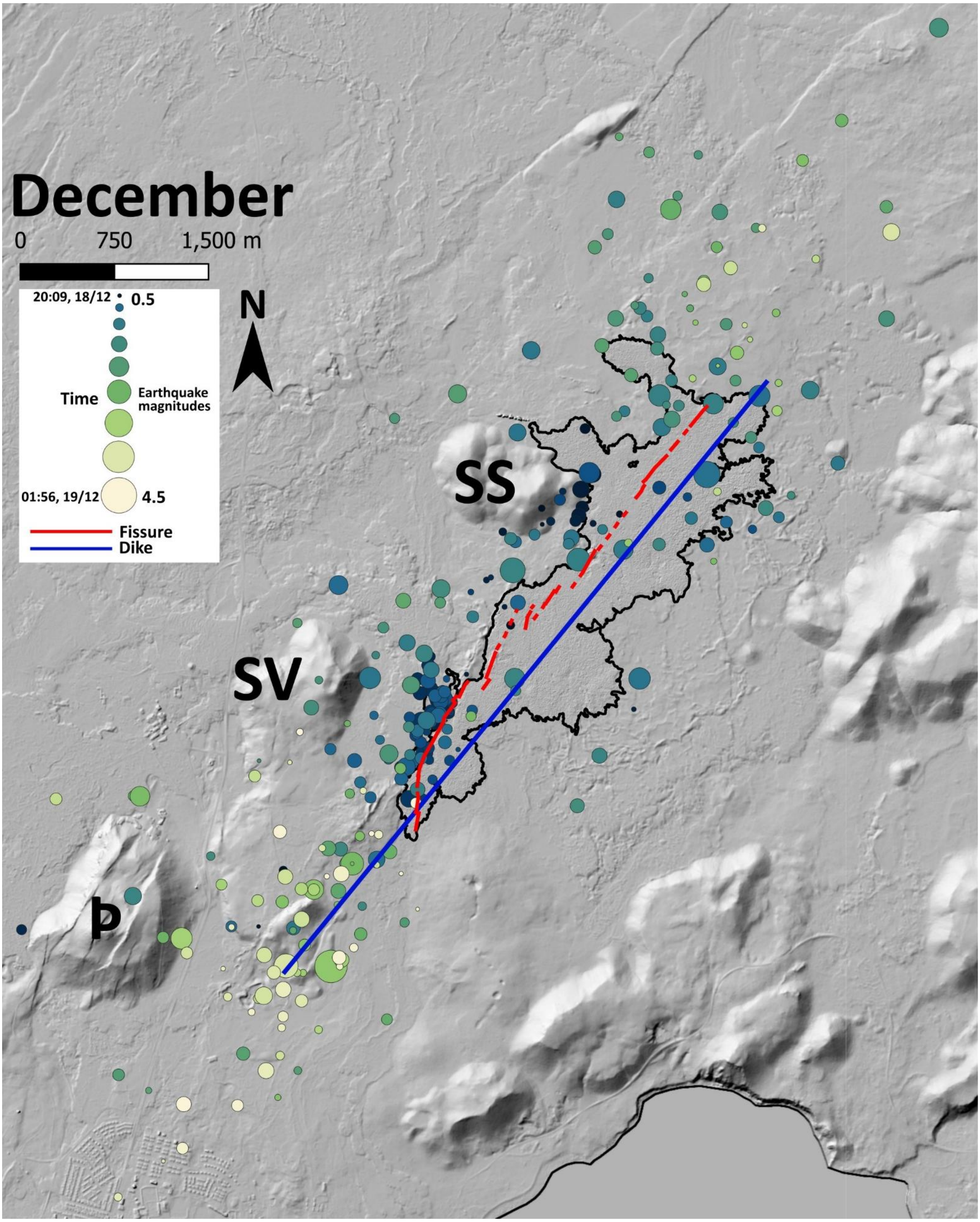

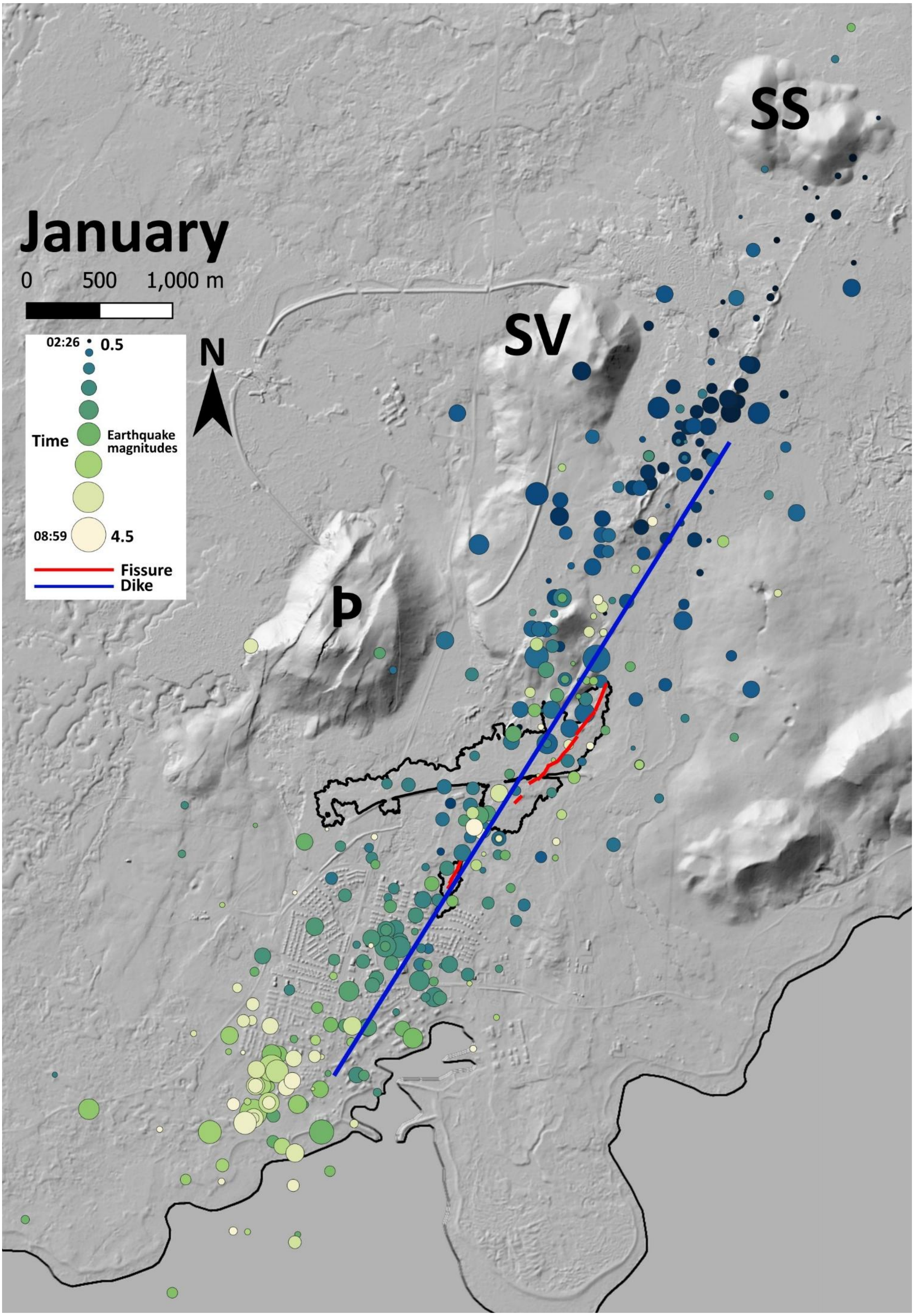
January
0 500 1,000 m
02:26
0.5
Time
Earthquake magnitudes
08:59
4.5
Fissure
Dike
N
SS
SV
Þ

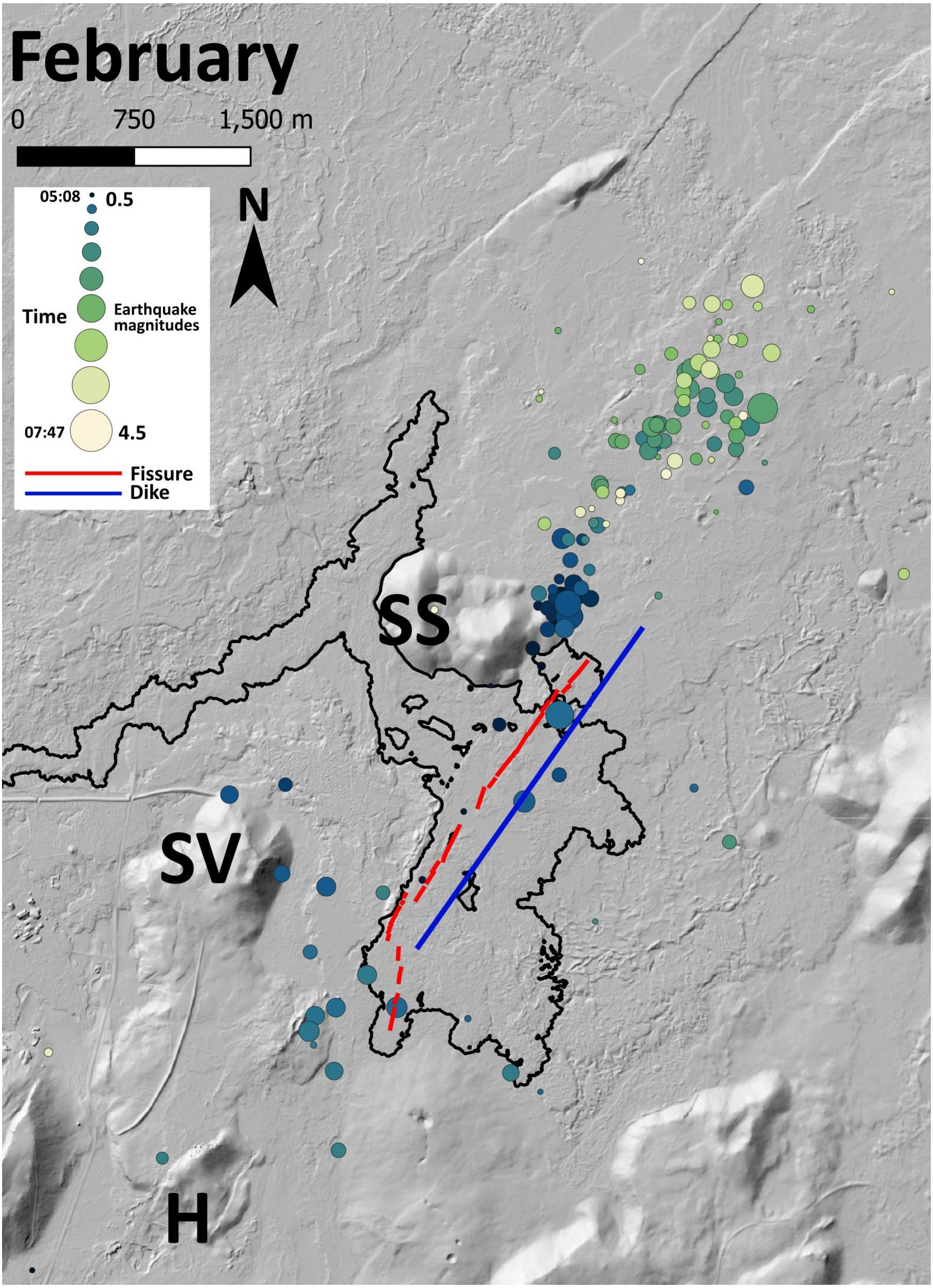
February
0
750
1,500 m
N
05:08
0.5
Time
Earthquake magnitudes
07:47
4.5
Fissure
Dike
SS
SV
H

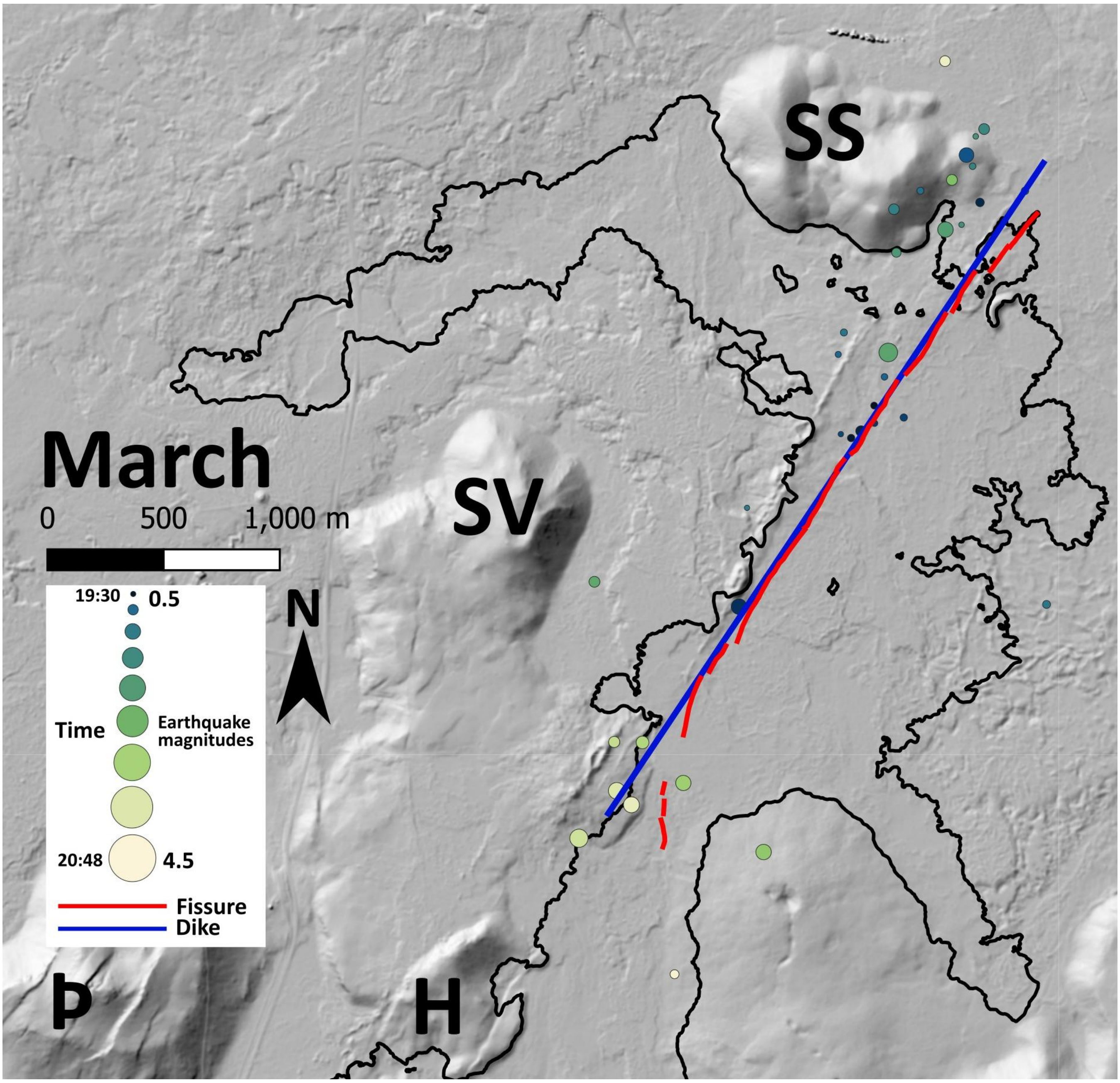

SS
March
0
500
1,000 m
SV
19:30
0.5
Time
Earthquake magnitudes
20:48
4.5
Fissure
Dike
N
Þ
H

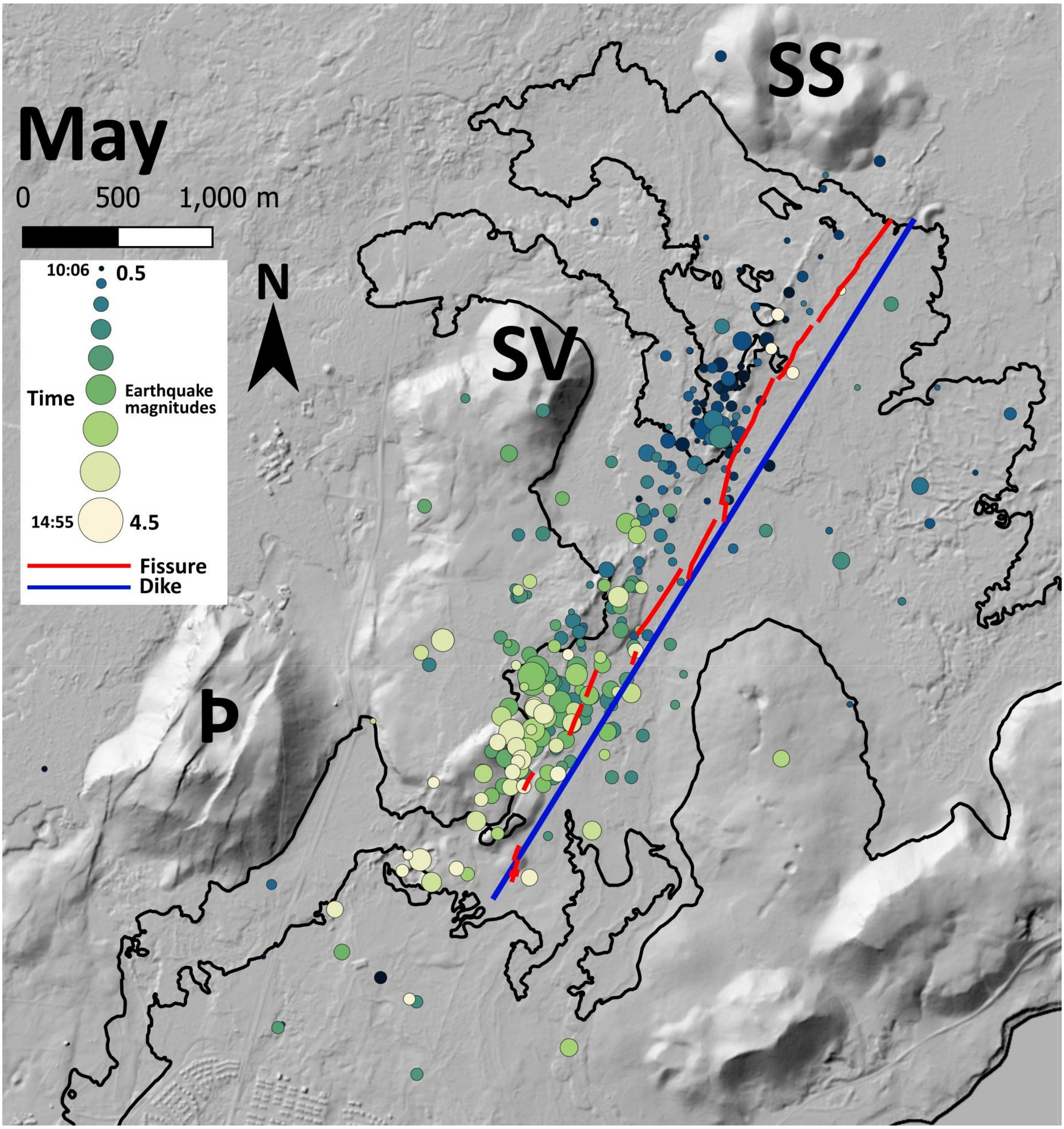
May
0 500 1,000 m
N
SS
SV
Þ
10:06
0.5
Time
Earthquake magnitudes
14:55
4.5
Fissure
Dike

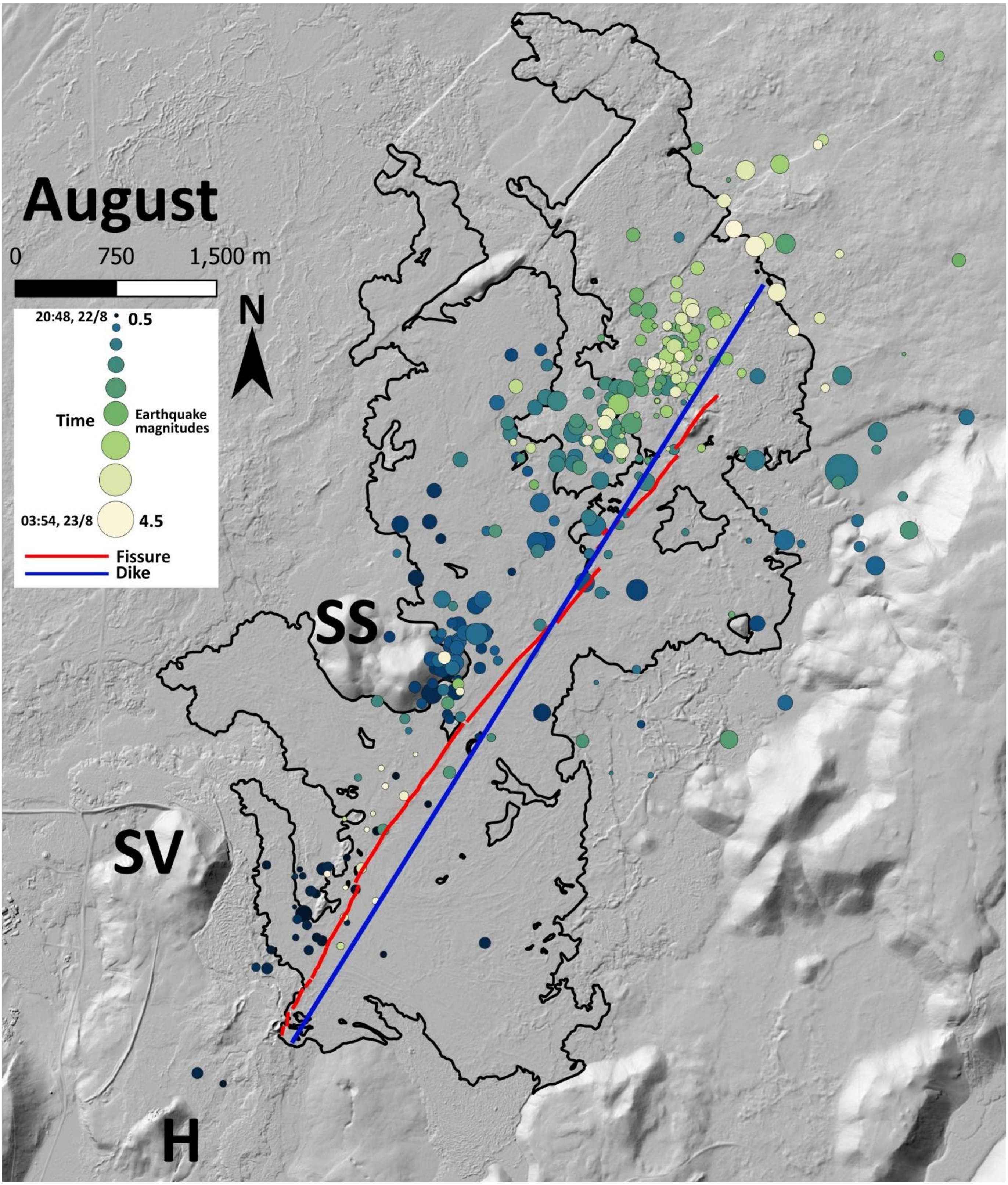

August
0
750
1,500 m
N
20:48, 22/8
0.5
Time
Earthquake magnitudes
03:54, 23/8
4.5
Fissure
Dike
SS
SV
H

Appendix C: Statistical Tests on Different Controlling Factors of Eruption Features

Eruption characteristic \ Controlling factor	Fissure length			Propagation speed			Fissure segment time from start of eruption			Fissure segment distance from start of eruption			Total volume erupted	Inflation duration	Eruption duration	Fire fountain height	Inflation volume
Fissure length							Dec	0.15	No	Dec	-0.087	No	0.89	0.72	0.69		0.7
							Jan	0.64	Yes	Jan	-0.72	Yes					
							Feb	0.10	No	Feb	-0.055	No					
							Mar	0.24	No	Mar	-0.29	No	Yes	No	No		No
							May	0.29	No	May	-0.45	No					
							Aug	0.48	No	Aug	-0.68	Yes					
Propagation speed	Dec	0.14	No				Dec	-0.15	No	Dec	0.021	No	0.34	-0.019	0.27		0.095
	Jan	0.42	No				Jan	-0.62	Yes	Jan	0.55	No					
	Feb	-0.44	No				Feb	0.13	No	Feb	0.41	No					
	Mar	0.61	No				Mar	-0.26	No	Mar	0.34	No	Yes	No	Yes		No
	May	0.14	No				May	-0.26	No	May	0.62	Yes					
	Aug	0.74	Yes				Aug	-0.37	No	Aug	0.5	No					
Fissure segment time from start of eruption																	
Fissure segment distance from start of eruption																	
Total volume erupted														0.93			0.71
														Yes			No
Inflation duration																	
Eruption duration													0.49	0.23			0.15
													No	No			No
Fire fountain height	Dec	0.3	No	Dec	0.15	No	Dec	0.42	No	Dec	0.51	No	0.51	0.51	0.49		0.065
	Jan	0.66	Yes	Jan	0.6	Yes	Jan	0.72	Yes	Jan	0.76	Yes					
	Mar	0.87	Yes	Mar	0.69	Yes	Mar	0.36	No	Mar	0.41	No	Yes	Yes	Yes		No
	Aug	0.26	No														
Inflation volume														0.8			
														No			

Colour explanations:

Significance of correlation

Significant | Not significant

Pearson's R value

Negligible | Weak | Moderate | Strong | Very strong